WORK FUNCTION STUDY OF IRIDIUM OXIDE AND MOLYBDENUM USING UPS AND SIMULTANEOUS FOWLER-NORDHEIM I-V PLOTS WITH FIELD EMISSION ENERGY DISTRIBUTIONS

John Michael Bernhard, B.S., M.S.

Dissertation Prepared for the Degree of

DOCTOR OF PHILOSOPHY

UNIVERSITY OF NORTH TEXAS

August 1999

APPROVED:

David E. Golden, Major Professor
Witold K. Brostow, Minor Professor
Bruce Gnade, Committee Member and Chair of the Department of Material Science
Zhibing Hu, Committee Member
Samuel E. Matteson, Chair of the Department of Physics
C. Neal Tate, Dean of the Robert B. Toulouse School of Graduate Studies

Bernhard, John Michael, Work Function Study of Iridium Oxide and Molybdenum Using UPS and Simultaneous Fowler-Nordheim I-V Plots with Field Emission Energy Distributions. Doctor of Philosophy (Physics), August 1999, 129 pp., 3 tables, 47 illustrations, references, 70 titles.

The characterization of work functions and field emission stability for molybdenum and iridium oxide coatings was examined. Single emission tips and flat samples of molybdenum and iridium oxide were prepared for characterization. The flat samples were characterized using X-ray Photoelectron Spectroscopy and X-ray diffraction to determine elemental composition, chemical shift, and crystal structure. Flat coatings of iridium oxide were also scanned by Atomic Force Microscopy to examine topography. Work functions were characterized by Ultraviolet Photoelectron Spectroscopy from the flat samples and by Field Emission Electron Distributions from the field emission tips. Field emission characterization was conducted in a custom build analytical chamber capable of measuring Field Emission Electron Distribution and Fowler-Nordheim I-V plots simultaneously to independently evaluate geometric and work function changes. Scanning Electron Microscope pictures were taken of the emission tips before and after field emission characterization to confirm geometric changes. Measurement of emission stability and work functions were the emphasis of this research. In addition, use of iridium oxide coatings to enhance emission stability was evaluated.

Molybdenum and iridium oxide, IrO_2, were characterized and found to have a work function of 4.6 eV and 4.2 eV by both characterization techniques, with the molybdenum value in agreement with previous research. The analytic chamber used in the field emission analysis demonstrated the ability to independently determine the value and changes in work function and emitter geometry by simultaneous measurement of the Field Emission Energy Distribution and Fowler-Nordheim I-V plots from single emitters.

Iridium oxide coating was found to enhance the stability of molybdenum emission tips with a relatively low work function of 4.2 eV and inhibited the formation of high work function molybdenum oxides. However, the method of deposition of iridium and annealing in oxygen to form iridium oxide on molybdenum emitters left rather severe cracking in the protective oxide coating exposing the molybdenum substrate.

ACKNOWLEDGMENTS

This work was supported by Motorola Flat Panel Display Division and the National Science Foundation through Grant No: DMR-9705187. Iridium oxide sample preparation was conducted at the Department of Materials and Nuclear Engineering, University of Maryland.

I want to thank Prof. David Golden for his years of guidance, patience, and encouragement throughout my graduate studies. I deeply appreciate Dr. Babu Chalamala's long term friendship and support. Ambrose Rouse, Ed Sosa, and Dr. Ike Akwani have been very helpful and informative, which assisted in the progression of this research, thank you.

TABLE OF CONTENTS

Page

LIST OF TABLES

Page

LIST OF ILLUSTRATIONS

Page

CHAPTER 1

INTRODUCTION

1.1 Introduction

The process of field emission is dynamic and energetic where the emitting surface can undergo changes in structure and composition that directly effects the emission current and energy distribution of emitted electrons. The primary attributes of a conductive material that effect field emission are work function (Φ) and emitter radius (b) or conversely tip sharpness [1]. These factors determine the height and width of the potential barrier the electrons must tunnel through from the Fermi level to the vacuum level once sufficient voltage is applied between an emission tip and its anode. Where the work function is the intrinsic property that represents the barrier height and the emitter radius effect the barrier width due to edge enhancement of the electric field [2, 3]. This barrier height and its stability under large field emission conditions for two materials (molybdenum and iridium oxide) are the emphasis of this research. Molybdenum is examined because it is currently used in field emission array devices, while iridium oxide (IrO_2) has the desirable properties of high conductivity, thermal and oxidation

stability, and the work functions of these materials are not well known [4,5,6].

1.2 Field Emission Applications and Flat Panel Displays

Field emission arrays (FEAs) are being developed as high brightness electron sources in microelectronic applications ranging from high-speed radio frequency sources and high-voltage and current switches to field emission flat panel displays [7,8,9]. The Spindt-type micro cathode FEAs are the common structures under development for field emission applications, illustrated in Figure 1.1 [10]. These emission arrays are formed by standard semiconductor processes, beginning with two conductive layers to form the cathode and gate sandwiched between an insulator. Holes are etched through the gate and insulating material down to the cathode, then metal is sputter deposited and automatically form tips in the holes as the opening through the gate is closed by the deposition process. This coating is lifted off the gate conductor and an anode is placed an arbitrary distance from the emission structure forming a Spindt-type FEA. These structures are under 1μm in size allowing high current densities. The emission can be quickly turned off and on by modulating the gate voltage with respect to the cathode, a characteristic that can not be accomplished with thermal emission and one that is useful for radio frequency and display modulation [11]. For Spindt FEAs with geometry shown in Figure 1.1, the gate voltage for field emission ranges from about 30-90V [12]. Moreover, if the anode is a phosphor screen, a flat panel display with CRT performance is produced.

For FEAs used in display applications, vacuum quality is a paramount factor in preventing emitter array degradation. Field emission display applications emphasize this

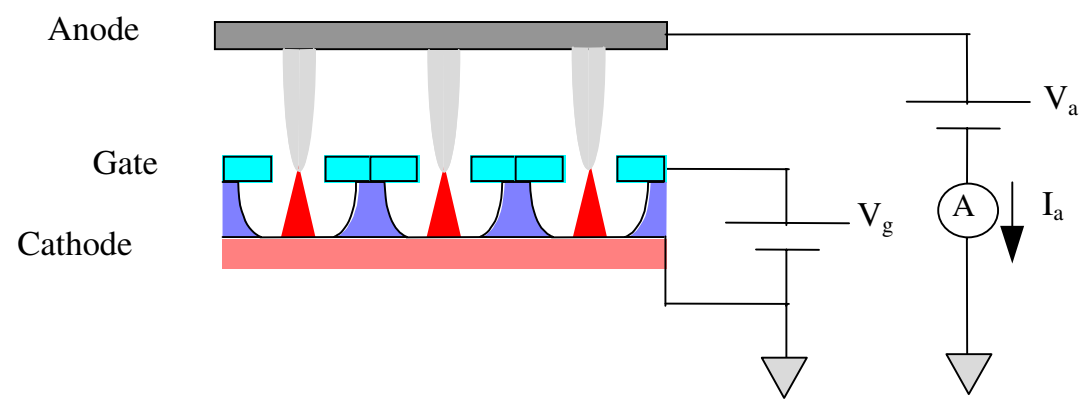

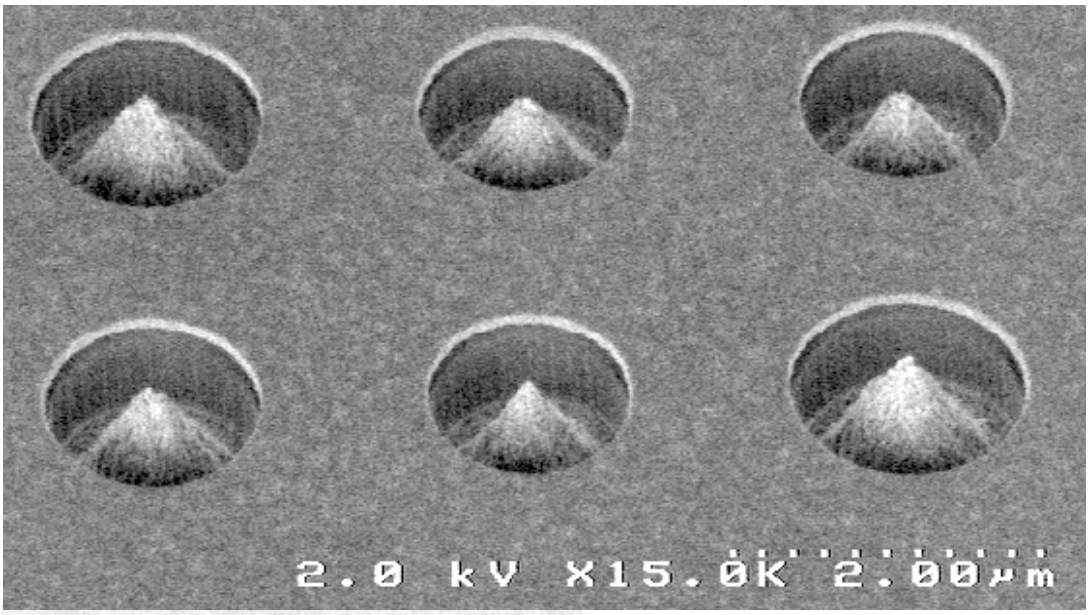

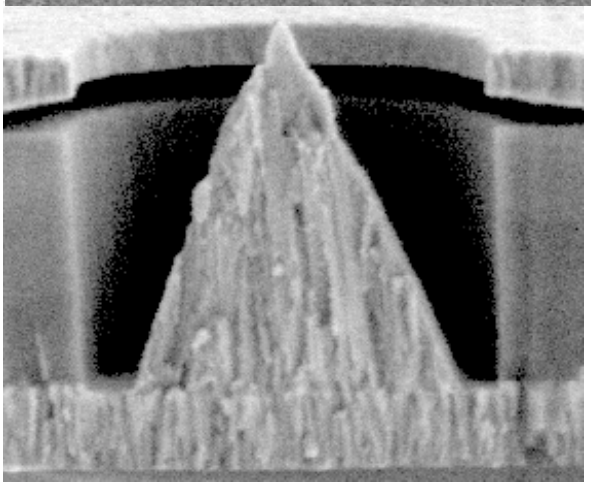

Figure 1.1. Top drawing is a schematic of the Spindt–type field emission array composed of emission tips, gate, and anode. The two SEM pictures are an overhead and cutaway view of the Spindt-type arrays under development at Motorola.

requirement because the phosphor screen out-gasses and must be located close to the emitters for good resolution giving a high surface to volume ratio in the display. Both these conditions lead to vacuum degradation. Background gases may be ionized by the extremely large electric field or by electron impact. The background gases and the ions react with the field emission surface, changing its geometry and work function. This induces current instabilities and device failures [13,14,15]. The analysis of surface modification under field emission conditions is the driving force behind this research, by providing a methodology to independently and simultaneously measure changes in work function and geometry. Particular interest is given to molybdenum and iridium oxide coatings because of their potential application in FEAs.

1.3 Molybdenum and Iridium Oxide Properties and Applications

Molybdenum is a group VIB metal, located directly above tungsten and possessing similar physical properties. The electrical, mechanical, and thermal robustness of the metal is good and the work function is average. The work functions values and some thermal and electrical parameters for molybdenum, molybdenum oxide (MoO_2), and iridium oxide are summarized in Table 1.1 [16,17]. Additionally, molybdenum Spindt-type FEAs form emitter tips with a high aspect ratio (tip height verses base diameter) providing a beneficial edge enhancement to field emission. Aspect ratios of some common metals used in Spindt-type FEAs are 1.3, 0.5, 2.0, 0.85, and 1.43 for Mo, Ti, Nb, Zr, and Cr [18]. However, oxides readily form on molybdenum under lower vacuum conditions and can increase the work function, with increases as large as 1.8 eV

Physical Property	Molybdenum (MoO_2)	Iridium Oxide, IrO_2
Work Function	4.6 eV (Poly) 4.36 eV (112) 4.53 eV (100) 4.55 eV (111) 4.95 eV (110)	To be determined
Melting Point	2623°C (1100°C)	1100°C
Electrical Resistance	4.85 μΩ cm	39-51 μΩ cm
Heat Capacity Cp	24 J/mol-K (56 J/mol-K)	57 J/mol-K
Thermal Conductivity	1.38 W/cm-K	?
Heat of Formation oxides $\Delta_f H^0$	(-588.9 kJ/mole)	-274.1 kj/mole
ΔG^0 for oxides	(-516 kJ/mole)	-161 kJ/mole
Crystal Structure	BCC a=3.14Å	Rutile a,b=4.51Å, c=3.15Å

Table 1.1.Summary of physical properties of molybdenum, molybdenum oxide (MoO_2) in parenthesis, and iridium oxide. Temperature dependent properties quoted at room temperature.

measured under 1×10^{-3} Torr pressure at room temperature [19]. This work function change leads to emission current reduction and instability, a process that has been directly measured from field emission arrays [20]. A low work function conductive oxidation barrier would be highly beneficial in maintaining stable emission for these arrays.

Iridium oxide has been used as an effective conductive oxidation barrier as junctions between conductive contacts and PZT ferroelectric thin film capacitors with applications in semiconductor memory [21]. The high electrical conductivity and thermal robustness of iridium oxide is quite good while the work function is unknown, Table 1.1 summarizes these values [6,16,22,23]. This oxide is also known to be very stable under hash chemical conditions as electrodes in electrolytic reactions, indicating stability under electric fields in ionic solutions [24,25]. All these above attributes indicate that iridium oxide has application as a protective coating for field emission tips, however the work function of this oxide needs to be determined. If the work function of iridium oxide is relatively low, field emission applications for this oxide are promising.

1.4 Methods to Determine Work Functions

Work functions were measured by two methods: (1) Ultraviolet Photoelectron Spectroscopy (UPS), and (2) Field Emission Energy Distribution (FEED) measurements with simultaneous Fowler-Nordheim (I-V) plots [1,26,27]. The first technique uses photoemission, where absorbed photons impart kinetic energy to electrons bound to the surface allowing them to overcome the surface potential barrier. The kinetic energy of these photoelectrons is measured, and their kinetic energy is equal to the difference

between the photon energy (hv) used to excite the sample and the work function (Φ) of the sample. This measurement is accurate if the photoelectrons originate near the Fermi level [28]. The second technique uses field emission, where an extremely large electrostatic field distorts the surface potential barrier allowing electrons to tunnel through the barrier from the Fermi level into the vacuum. The simultaneous measurement of FEEDs and Fowler-Nordheim I-V curves allows determination of; (1) the work function of a material from the inflection point of the FEED, and (2) tip geometry stability from the slope of the Fowler-Nordheim I-V curve. This slope is dependent on tip geometry (b) and work function (Φ) were the Fowler-Nordheim I-V slope = $-b\Phi^{3/2}$ [1,29,30]. FEEDs spectrum have a sharp onset located at the Fermi level of the emitter with an exponential decay at energies below the Fermi level, however the distribution is broadened thermally and by the finite energy resolution of the spectrometer. These distributions can be fitted with exponentially modified Gaussians where the inflection point on the Gaussian edge corresponds to the location of the emitter Fermi level with the energy difference between the Fermi and vacuum level equal to the work function [31]. Both methods involve electrons being removed from the solid at the Fermi level into vacuum free particle states overcoming the potential barrier found at the material's surface which is equal to the work function.

1.5 Scope of Present Work

The purpose of this work is to study work functions and their stability for molybdenum and iridium oxide coatings under field emission conditions. Single emission

tips and flat samples of molybdenum and iridium oxide were prepared for characterization. The flat samples were characterized using X-ray Photoelectron Spectroscopy, X-ray diffraction, and Ultraviolet Photoelectron Spectroscopy to determine elemental composition and chemical shift, crystal structure, and work function. This study was conducted to confirm sample composition and have two sources of work function information. Additionally, the flat samples of iridium oxide were scanned by Atomic Force Microscopy to examine topography of the coatings. Single emission tips were etched from pure molybdenum wire and molybdenum wire coated with iridium oxide to characterize the materials under field emission conditions. Scanning Electron Microscope (SEM) pictures were taken of the emission tips before and after field emission measurements. Field emission characterization was conducted in a custom build analytical chamber capable of simultaneously measuring FEEDs and Fowler-Nordheim I-V plots to independently evaluate geometric and work function changes.

References.

1. R.H. Fowler and L. Nordheim, Proc. Roy. Soc. London, **A119**, 683 (1928).
2. W.P. Dyke and W.W. Dolan, Adv. Electronics and Electron Phys., **8**, 90 (1956).
3. J.D. Jackson, *Classical Electrodynamics*, John Wiley & Sons, New York, 75-78 (1962).
4. S. Itoh, T. Niyamam, and M. Yokoyama, J. Vac. Sci. Tech., **B11**, 647 (1993).
5. W.D. Ryden, A.W. Lawson, and C.C. Sartain, Phys. Rev, **B1**, 1494 (1970).
6. E.H.P. Cordfunke and G. Meyer, Recueil, **81**, 495 (1962).
7. C.A. Spindt and I. Brodie, Adv. Electron. Electron Phys., **83**, 1 (1992).
8. I. Brodie and P.R. Schwoebel, Proc. IEEE, **82**, 1006 (1994).
9. H.F. Gray, Infor. Displ., **3**, 9 (1993).
10. C.A. Spindt, J. Appl. Phys., **39**, 3504 (1968).
11. T Utsumi, J. Soc. Infor. Displ., **1/3**, 313, (1993).
12. C.A. Spindt, United States Patent: 4926056 (1990).
13. J.H. Block, *Chemistry and Physics of Solid Surfaces*, CRC Press, Boca Raton FL, ch3., (1977).
14. P.R. Schwoebel and I. Bordie, J. Vac. Sci. Technol., **B13**, 1391 (1995).
15. P.H. Holloway, J. Sebastian, T. Trottier, H. Swart, and R.O. Peterson, Solid State Tech., **38**, 47 (1995).
16. CRC Handbook of Chemistry and Physics, 77^{th} ed., (1997).
17. S. Berge, P.O. Gartland, and B.J. Slagsvold, Surf. Sci., **43**, 275 (1974).

18. S. Itoh, T. Watanabe, K. Ohtsu, M. Taniguchi, S. Uzawa, and N. Nishimura, J. Vac. Sci. Tech., **B13**, 487 (1995).

19. J. Müller, Surf. Sci., **69**, 708 (1077).

20. B.R. Chalamala, R.M. Wallace, and B.E. Gnade, J. Vac. Sci. Technol., **B16**, 2859 (1998).

21. T. Nakamura, Y. Nakao, A. Kamisawa, and H. Takasu, Appl. Phys. Lett., **65**, 1522 (1994).

22. M.A. El Khakani, M. Chaker, and E. Get, Appl. Phys. Lett., **69**, 2027 (1996).

23. D.B. Rogers, R.D. Shannon, A.W. Sleight, and J.L. Gilson, Inorganic Chem., **8**, 841, (1969).

24. K. Kreider, Sensors and Actuators, **B5**, 165 (1991).

25. M. Blouin and D. Guay, J. Electrochem. Soc., **144**, 573 (1997).

26. A. Einstein, Annalen der Physik, **17**, 132 (1905).

27. A. Modinos, *Field, Thermionic, and Secondary Electron Emission Spectroscopy*, Plenum Press, New York, 1-18 (1984).

28. C.N. Berglund and W.E. Spiecer, Phys. Rev., **136**, A1030 (1964).

29. R.D. Young, Phys. Rev., **113**, 110 (1958).

30. R. Gomer, *Field Emission and Field Ionization*, Harvard Univ. Press, Cambridge MA, 6-33 (1961).

31. R.D. Young and C.E. Kuyatt, Rev. Sci. Inst., **39**, 1477 (1968).

CHAPTER 2

THEORY OF PHOTOEMISSION AND FIELD EMISSION FROM SOLIDS

2.1 Introduction

The emphasis of this research is an in depth study of molybdenum and iridium oxide with particular interest in their work functions. To characterize this quantity two methods were used: (1) Ultraviolet Photoelectron Spectroscopy (UPS), and (2) simultaneous Field Emission Energy Distribution (FEED) and Fowler-Nordheim current-voltage (I-V) plots. Both methods remove electrons from a solid into vacuum by overcoming the potential barrier at the material's surface. The strength of this potential barrier is dependent on the material, crystalline planes, and surface topography. In photoemission, photons impinging on the surface are absorbed and impart kinetic energy to electrons allowing them to overcome the surface potential barrier, while in field emission, an electrostatic field distorts the surface potential barrier allowing electrons to tunnel through the barrier into the vacuum. This chapter will review physical theories and characterization methods associated with photoemission and field emission.

2.2 Theory of Photoemission from Solids

The first theoretical description of the photoelectric effect introduced the existence of photons, quanta in energy of electromagnetic fields [1]. The energy (E) of these photons corresponds to the photons frequency (v).

$$E = h\,v \tag{2.1}$$

Where the constant h is Plank's Constant. This straightforward treatment by Einstein concludes that electrons excited from a sample by photons have a maximum kinetic energy (KE) that is determined by the photons energy and the work function (Φ) of the sample.

$$KE = h\,v - \Phi \tag{2.2}$$

Photoemission can be used to probe the electronic band structure and surface conditions. Lattice planes of crystalline material can be distinguished and characterized with photoemission. Photoelectrons can be excited in the bulk of the crystal, where an electron is excited between energy levels in or between the valence and conduction bands. Alternatively, excitation can happen on the surface, where surface states (plasmon creation and annihilation) and electron gas in the solid coupling to vacuum interface leads to photoelectron emission. The work function of a material is a measure of how far the Fermi level is below the vacuum level and the electron Density of States (DOS) around that level. If there is no band bending at the surface, a phenomenon found in some semiconductors, the work function can be related to the bulk material. Therefore the bulk properties are of interest in this research, and an effective model of photoemission was

developed by Berglund and Spicer that detailed electron excitation from the bulk in a three step process: (1) optical excitation of electrons from the bulk by evaluating the optical density of electron states; (2) transportation of excited electrons through the crystal lattice to the surface by an energy-dependent mean free path scattering process; and (3) ejection of electrons from the surface to vacuum through the surface barrier [2]. Given that the bulk optical density of states is independent of transportation and surface barrier effects, excited electrons with sufficient energy to cross the surface barrier have a probability to escape from the solid into free space.

2.2.1 Photon Excitation via Direct and Indirect Transitions

The calculation of the photon excitation of a bound electron in the bulk involves the coupling of the quantum mechanical lattice electron and its associated energy levels to the electric field component of electromagnetic radiation exciting the sample. Note this assumes that the photon wavelength is large and slowly varying compared to the bound orbital structure of the electrons, and the magnetic component of radiation is unimportant in the excitation process. The first-order quantum mechanical perturbation ($\mathbf{H_1}$) for radiation added to the standard atomic lattice and electron Hamiltonian ($\mathbf{H_0}$) is a coupling between the radiation's electric vector potential ($\mathbf{A}$), momentum ($\mathbf{p}$), and position ($\mathbf{r}$) of the electrons. This perturbation is summed over the number of electrons (n) [3].

$$\mathbf{H_1} = \sum_n \left(\frac{e}{2mc} \left(\mathbf{p}_n \bullet \mathbf{A}(\mathbf{r}_n, t) + \mathbf{A}(\mathbf{r}_n, t) \bullet \mathbf{p}_n \right) \right) \tag{2.3}$$

Applying this perturbation ($\mathbf{H_1}$) to the one-electron approximation with unperturbed ($\mathbf{H_0}$) eigenvalue energies (E_ω) and eigenfunctions ($|\omega\rangle$) the one electron density matrix (ρ_o) satisfies the following.

$$\rho_o|\omega\rangle = f(\omega)|\omega\rangle \tag{2.4}$$

$$ih\frac{\partial\rho}{\partial t} = [\mathbf{H_0} + \mathbf{H_1}, \rho] \tag{2.5}$$

Function $f(\omega)$ is some distribution dependent on the eigenfunctions and corresponding eigenvalue energies, for example a Fermi-Dirac distribution. The probability of radiation excitation is dependent on the change in ρ, where ρ is a series expansion of ρ_o and higher order terms. An expansion of ρ using equation 2.5 gives the following equations for the first and second order terms in the expansion series.

$$ih\frac{\partial\rho_1}{\partial t} = [\mathbf{H_0}, \rho_1] + [\mathbf{H_1}, \rho_0] \tag{2.6}$$

$$ih\frac{\partial\rho_2}{\partial t} = [\mathbf{H_0}, \rho_2] + [\mathbf{H_1}, \rho_1] \tag{2.7}$$

Equation 2.6 is the first-order linear correction and equation 2.7 is the second-order quadratic correction. For external currents corresponding to electron photoemission the first order correction does not contribute because the corresponding first order current density correction goes to zero. So external current density is quadratic (second-order) and evaluation of 2.7 and current density gives the "golden rule" for photo excitation [4].

$$\mathbf{J}(\omega) = \frac{2e\pi}{S\hbar}\sum_{i,f} f(\omega)\left|\langle f|\mathbf{H_1}|i\rangle\right|^2 \delta\left(E_f - E_i - \hbar\omega\right) \tag{2.8}$$

J is the averaged photo current density as a function of photon frequency (ω) and *S* is the surface area exposed to photons. Equation 2.8 is a two-body process where a photon directly liberates an electron from a filled steady state (*i*) to an empty excited state (*f*) and is called a direct optical transition. The law of conservation of energy and momentum require that $E_f - E_i$ equal the photon energy absorbed ($\hbar\omega$) and that the difference in electron wave vectors ($\mathbf{k}_f - \mathbf{k}_i$) be equal to the photon wave vector ($\mathbf{k}_\omega$). However the photon wave vector is very small compared to the electron wave vector so it is approximated that the electron wave vector is conserved ($\mathbf{k}_f = \mathbf{k}_i$). Conservation of energy is explicitly stated in the above equation with the delta function, and conservation of momentum is implied by requiring that the initial and final states have the same wave vector. The following equation calculated by Kane for photon absorption (*w*) of a given volume (V) explicitly states both conservation laws and performs the wave vector calculation on the perturbation Hamiltonian ($\mathbf{H_1}$) [5].

$$w = \frac{2\pi}{\hbar}\frac{e^2}{m^2c^2}\frac{2\mathrm{V}}{(2\pi)^3}\sum_{i,f}\int_{B.Z.}\left|\mathbf{A}\bullet\underset{f\,i}{\mathbf{p}}(\mathbf{k})\right|^2\delta\left(E_f(\mathbf{k})-E_i(\mathbf{k})-\hbar\omega\right)d\mathbf{k} \qquad (2.9)$$

The equation has a factor of two included for spin, and the integration of **k** is over one Brillouin Zone corresponding to a particular crystalline lattice face and its band structure in **k** space. The summation *i* runs over all filled valence bands and summation *f* runs over all empty conduction and valence bands.

As previously mentioned the above is a two-body process, however indirect transitions can occur where the electron wave vector is not conserved in a three-body

process. Phonon emission or absorption in a photon, electron, and phonon indirect transition maintains momentum and energy conservation. The second-order "golden rule" describes this two-step three-body process of (1) photon creation of an electron-hole pair and (2) phonon scattering with either electron or hole to their final states [5]. This second-order equation has a double summation over the states in each step of the two-step process, and a double integration over the final wave vector of the electron and corresponding hole/phonon. In general, the photon absorption will be greater for two-body one-step process verses a three-body two-step process. However, for some materials and particular lattice planes the indirect process is dominant at low photon energies because the direct energy gap between filled and empty electron bands is greater than the indirect gap. In this study, polycrystalline surfaces were characterized where many lattice planes and grain boundaries were exposed to photo excitation. This type of surface has a high probability of providing lattice planes with direct transitions that will dominate over indirect transitions.

The electron energy distributions for direct and indirect transitions have distinct characteristics illustrated in Figure 2.1.A and B. Figure 2.1.A shows a hypothetical ban structure of a solid where the k vector is along the **x**-axis and energy is along the **y-**axis. For both transitions the electron kinetic energy is determined by how far the final energy band is located above the vacuum energy level. The difference between direct and indirect transitions can be graphically represented by restricting direct transitions to only vertical jumps between energy levels in the band diagram and indirect transitions do not

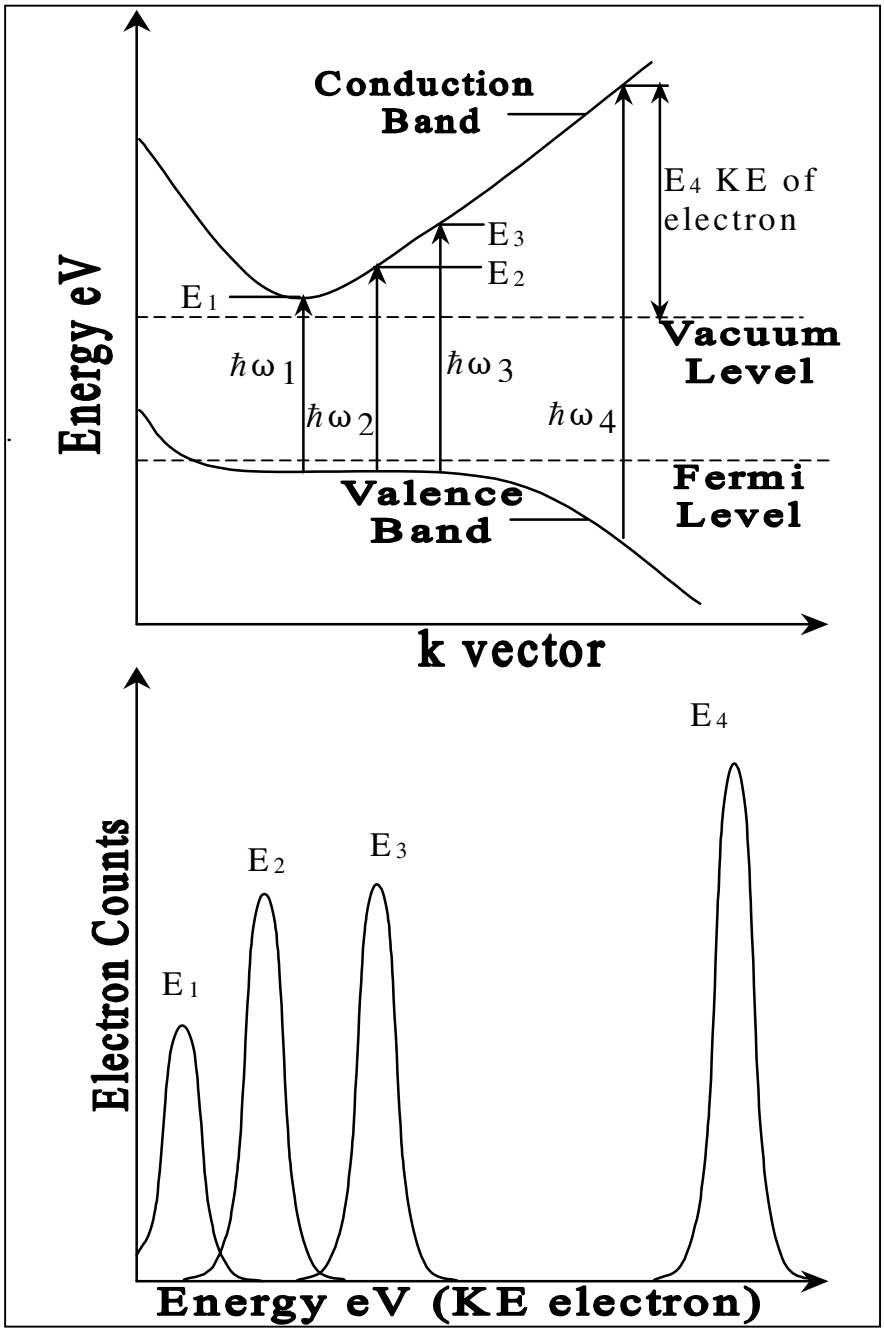

Figure 2.1.A. The figure represents direct transitions where **k** is conserved, giving narrow energy distributions. E_1 to E_3 distributions move with photon energy and E_4 is lower when compared to its photon energy due to a lower energy initial state.

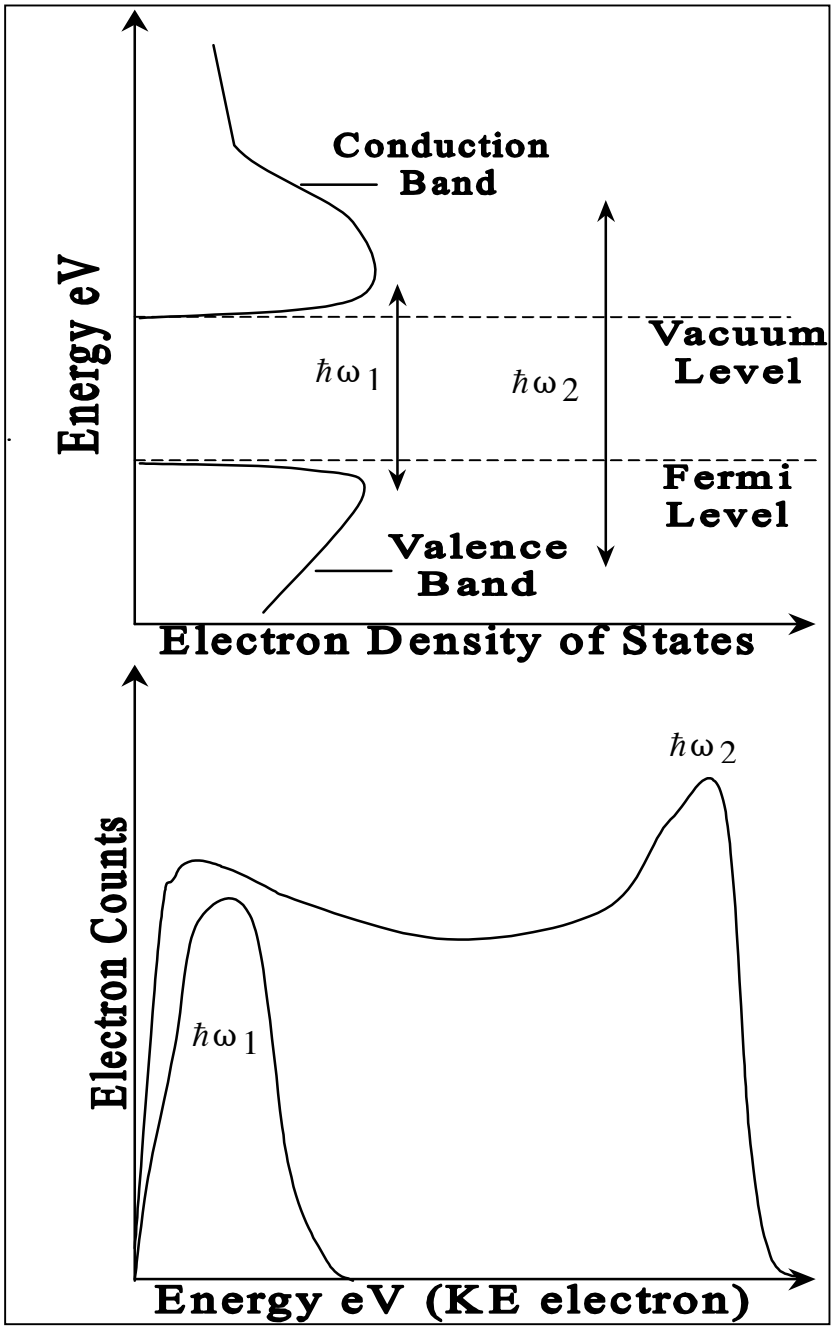

Figure 2.1.B. The figure represents indirect transitions that reflect the DOS and the leading high energy edge of the distributions move with photon energy, followed by lower energy electrons that originated deeper in the valence band.

have this restriction. Therefore, direct optical transitions are more restricted in their energy distribution with well-defined Gaussian forms, with mean values corresponding to the energy difference between the vacuum level and final state. For direct transitions, a particular photon energy excites an electron from a distinct location in the initial and final electron bans that have an energy separation equal to the photon energy. The electron kinetic energy for direct transitions does not shift linearly with photon energy unless the initial energy band is flat, if this is not the case different photon energies will excite electrons from initial states of different energy causing a non linear shift in the electron emission distribution. Indirect transitions, shown in Figure 2.1.B, have energy distributions that reflect the electron density of states corresponding to the transition. This excitation process sweeps out the distribution of states where the highest energy electrons correspond to the highest energy in the initial states and the lower energy electrons are excited from deeper initial states. So the leading, high energy, edge sweeps linearly with photon energy and the lower energy distributions are detected dependent on the electron density of states [6].

2.2.2 Kinematics of Photoelectron Transportation and Surface Emission

To determine quantum yield (Y) electrons liberated per photon absorbed at threshold photon energies for direct transitions, Kane first evaluated equation 2.9 with restrictions on the integration over k space that allow electron ejection into vacuum [5].

$$\frac{\partial E_f(\mathbf{k})}{\partial \mathbf{k_n}} > 0 \qquad (2.10)$$

$$E_f(\mathbf{k}) = \frac{\hbar^2\left(\mathbf{k}_t^2 + \mathbf{k}_{\mathbf{n}'}^2\right)}{2m} \tag{2.11}$$

In the above equations $\mathbf{k_t}$, $\mathbf{k_n}$, and $\mathbf{k_{n'}}$ are tangential and normal components of the **k** vector to the surface where the normal component can have different values in the solid (**n**) and in vacuum (**n′**). This extra restriction is placed on the integral in equation 2.9 and the yield is the ratio below, where the prime (′) denotes the restrictions from equation 2.10 and 2.11.

$$Y = \frac{\sum_{i,f}\int' \left|\mathbf{A}\bullet\underset{fi}{\mathbf{p}}(\mathbf{k})\right|^2 \delta\left(E_f(\mathbf{k}) - E_i(\mathbf{k}) - \hbar\omega\right)d\mathbf{k}}{\sum_{i,f}\int_{B.Z.} \left|\mathbf{A}\bullet\underset{fi}{\mathbf{p}}(\mathbf{k})\right|^2 \delta\left(E_f(\mathbf{k}) - E_i(\mathbf{k}) - \hbar\omega\right)d\mathbf{k}} \tag{2.12}$$

These conditions represent yield with no scattering and no surface threshold or work function. A work function can be introduced as threshold energy (E_T) and the following restriction added to the prime integration in 2.12.

$$\hbar\omega - E_T = \left[\nabla_{\mathbf{k}}\left(E_f(\mathbf{k}) - E_i(\mathbf{k})\right)\right]_{\mathbf{k_d}} \bullet \hat{\mathbf{k}}_{\mathbf{n}} + \text{higher order terms} \tag{2.13}$$

At threshold where $\hbar\omega$ is equal to E_T the prime integral in 2.12 collapses to a vector or a set of vectors symmetric about the normal vector ($\mathbf{k_n}$) and this is referenced by the vector $\mathbf{k_d}$. The vector $\mathbf{k_d}$ represents the most direct path/direction from solid to vacuum from an energy perspective, and is the origin for the gradient function in equation 2.13. When all of the above restrictions on the **k** vector are applied to the numerator in equation 2.12 the Yield (Y) is found to have a linear dependence in photon energy (E_ω) $Y \propto (E_\omega - E_T)$ when $E_\omega > E_T$, note this relation ignores any scattering processes. If electron scattering is

included, the calculated yield is a product of four quantities: (1) (p_s) the probability that the electron is scattered with minimal electron loss, (2) (p_e) the probability of electrons escaping before scattering with substantial loss of energy, (3) ($f_e(E_\omega - E_T)$) fraction of excited electrons with sufficient energy to escape, and (4) ($f_s(E_\omega - E_T)$) fraction of scattered electrons that have their tangential momentum to the surface confined to the escape cone that provides enough kinetic energy normal to the surface to overcome the surface potential [5].

$$Y = p_e p_s f_e(E_\omega - E_T) f_s(E_\omega - E_T) \tag{2.14}$$

The values of p_e and p_s are constants with respect to photon energy over the limited energy range correlated to threshold energies, $p_e = \exp(-\omega t)$ where ω is the inelastic scattering rate and inversely proportional to the mean free path length, and p_s is the ratio of scattering that causes minimal energy loss maintaining levels above E_T over total scattering events. Both f_e and f_s are linear in response to photon energy when it is above threshold. The term f_e is like the calculation for the non-scattering case above (Y) except $\mathbf{k_d}$ direction(s) are expanded to include elastic and phonon scattering. While f_s is a direct calculation between initial and final states in **k** space and what fraction have sufficient energy normal to the surface to overcome its potential. This calculation is similar to the yield calculation except the coupling term between electrons and radiation (**A•p**) is excluded because the electrons are already excited. Equation 2.14 leads to a yield that is quadratic in photon energy and agrees with experimental results of clean metal surfaces by Spicer and Fowler [6,7].

$$Y \propto (E_{\omega} - E_T)^2 \quad E_{\omega} > E_T \tag{2.15}$$

2.2.3 Correlation of Work Function and Threshold Energy for Photoemission

The threshold photon energy (E_T) the minimum photon energy required to excite electrons from a solid has previously been correlated with the work function of the material. This is true for metals where there is a continuous electron density of states above and below the Fermi level, however not all materials (for example semiconductors and insulators) have a continuous distribution around the Fermi level. Figure 2.2 represents the band diagram seen in semiconductors and metals. In the figure the labeled quantities are: (E_{vac}) vacuum level, the energy level of a free electron with zero kinetic energy; (E_F) Fermi level, the energy of the least bound electrons in solids at absolute zero; (E_V) valence band, the upper energy limit of the valence band; (E_C) conduction band, the lower energy limit of the conduction band; (E_G) energy gap, the difference between filled and empty electron states, for semiconductors this is the difference between E_C and E_V; (E_T) threshold energy, the minimum photon energy needed for photoemission and the difference between E_{vac} and E_v; (Φ) work function, the difference between E_{vac} and E_F; and (χ) electron affinity, the difference between E_{vac} and E_C and can be positive or negative if the conduction band is below or above the vacuum level. The work functions of most materials fall in the range of 3–5 eV. The threshold energy is the lowest photon energy needed to excite an electron from the highest occupied electron energy level to the vacuum level, for a semiconductor this would be from the top of the valence band to vacuum.

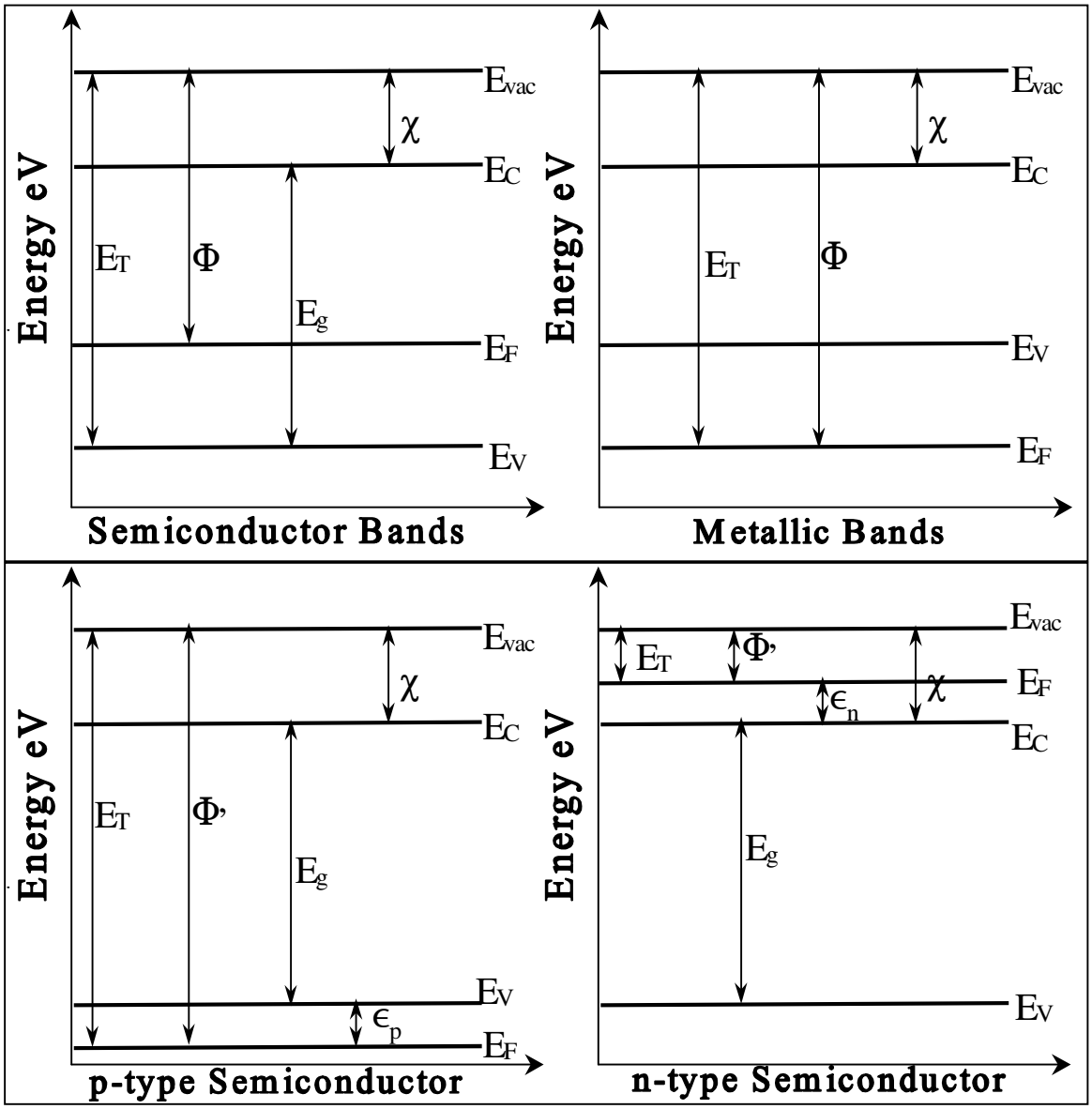

Figure 2.2. The top left schematic is the band structure of an intrinsic semiconductor, and the right is for an intrinsic conductor or metal. The bottom schematic is the band structure for heavily doped semiconductors p-type (left) and n-type (right).

$$E_T = \chi + E_g \tag{2.16}$$

Note that χ can be positive or negative depending on whether the material has a negative electron affinity or positive value. For a heavily doped p-type semiconductor the Fermi level is pushed to just below the valence band edge by a small value (ϵ_p) increasing the threshold energy.

$$E_T = \chi + E_g + \epsilon_p \tag{2.17}$$

For heavily doped n-type semiconductors the Fermi level is pushed to just above the conduction band edge by a small value (ϵ_n) lowering the threshold energy.

$$E_T = \chi - \epsilon_n \tag{2.18}$$

For conductors the Fermi level is naturally located in the valence band, therefore the energy gap (E_g) between empty and filled electrons states goes to zero and threshold energy equals the work function.

$$E_T = \Phi \tag{2.19}$$

Thus, the work function evaluation of metals and conductors is very straightforward in comparison to semiconductors where doping and band gap influence the photoemission characteristics. The continuous electron density of states around the Fermi level make conductors conductive and dictate that the photoemission electrons originate from the Fermi level at threshold photon energies allowing the straightforward correlation of equation 2.19 that was first postulated by Einstein. This is shown in equation 2.2 where the kinetic energy approaches zero as the photon energy goes to the work function value of Φ.

2.3 Theory of Field Emission from Solids

Field emission discharge is a common phenomenon found in high-voltage experiments under vacuum, especially under vacuum in the millitorr range where the breakdown voltage of air is at a minimum. This emission is inherently transcendental and R.W. Wood has the first to detail field emission in 1897 [8]. At first, theoretical analysis of field emission was unsuccessful in predicting current verses voltage responses, due to the classical treatment of electrons being thermally excited over a reduced potential surface barrier [9]. In reality, field emission is a quantum mechanical process where the electron "tunnels" through the reduced potential surface utilizing the wave and de-localization aspects of the electron to be transmitted/reflected by this potential. Fowler and Nordheim utilizing the Sommerfeld electron theory of metals in 1928 developed a successful quantum mechanical theory to predict the current verses voltage response found in field emission from metals [10,11]. This model correctly predicted that the electrons originated from the Fermi level in the metal. A more detailed theoretical analysis by Young of the field emission energy distribution (FEED) of electrons revealed that the total energy distribution of the electrons was being measured not just the energy component normal to the surface [12,13]. This is because high potentials found around a sharp emission tip focus all of the kinetic energy of the electrons towards the anode acting as an electrostatic lens. Young also evaluated the influence of thermal excitation leading to a Gaussian smoothing of the FEED due to the broadening of the electron DOS around the Fermi level.

2.3.1 The Free Electron Model and Reduced Surface Potential for Field Emission from Metals

The Fowler-Nordheim calculation of field emission uses the free electron theory of metals proposed by Sommerfeld, which treats conduction electrons as free particles with a corresponding quantum mechanical plane wave distribution (Ψ).

$$\Psi(\mathbf{k},\mathbf{r}) = \frac{1}{V^{1/2}}\exp(i\mathbf{k}\bullet\mathbf{r}) \tag{2.20}$$

$$\mathbf{k} = \frac{2\pi}{L}(n_x, n_y, n_z) \quad ; E = \frac{\hbar^2 k^2}{2m} \tag{2.21}$$

Where **k** and **r** are the wave vector and position of the electron, **k** is quantified by integers $n_{x,y,z}$, and E and m are energy and mass of the electron. The quantities V and L are volume and length of the solid metal and considered very large relative to the electron wave function (Ψ). The electrons also have an energy distribution corresponding to the Fermi-Dirac distribution function [14]. This valid free particle approximation greatly simplifies the calculation of reflection/transmission probabilities through the reduced surface barrier.

Figure 2.3 is a potential energy diagram for an electron distance x away from a metal surface located at x = 0 with an applied electric field (F) where E_F and Φ are the Fermi level and work function of the metal. The following equations define the potential.

$$V(x) = \left(E_F + \Phi - \frac{e^2}{4x} - eFx\right) \; ; \; x > X_C \tag{2.22}$$

$$V(x) = 0 \; ; \; x < X_C \tag{2.23}$$

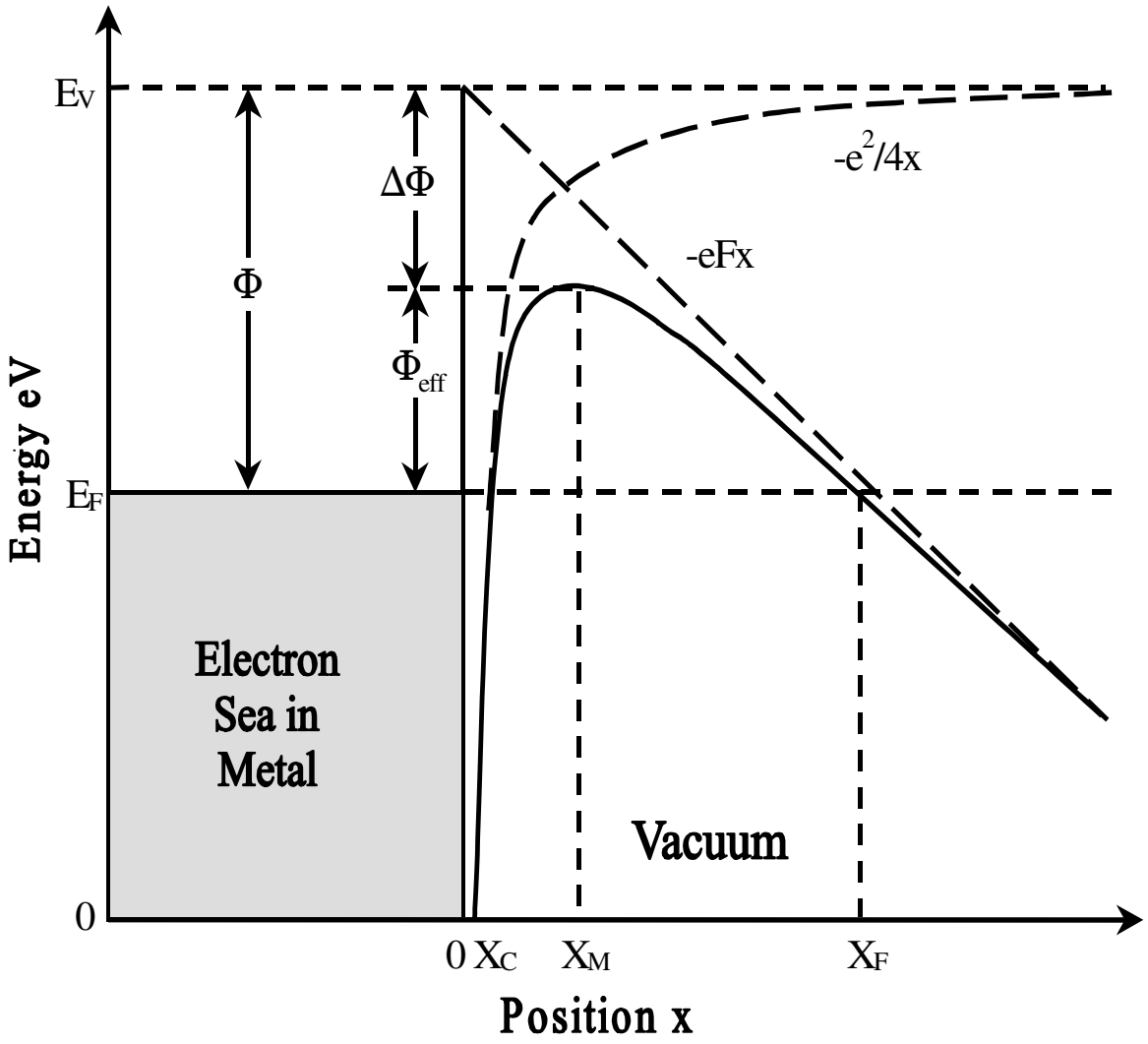

Figure 2.3. The potential energy of an electron near a metal surface with a Fermi level and work function (E_F and Φ). The position dependent potential in vacuum is due to image charge potential ($-e^2/4x$) and applied external electric field (-eFx). The electron feels zero potential very close to the surface and inside the metal ($x < X_C$).

When the electron is in the metal the free particle approximation puts the potential at a constant, equation 2.23. If the electrons in the metal are at V= 0 the vacuum level (E_V) is $E_F + \Phi$, the $-e^2/4x$ term is due to attraction between an external electron and imaginary positive image charge induced in conductors, the $-eFx$ is an additional potential on the electron from an external applied electric field. The value X_C satisfies $V(X_C) = 0$ and has the value of $e^2/4(E_F + \Phi)$ approximating that the field effect ($-eFx$) is small so close to the surface. The reduced potential barrier due to applied electric field has a maximum at X_M where $dV(x)/dx = 0$ and $X_M = (e/4F)^{1/2}$, this is called the Schottky saddle point. Putting X_M back in equation 2.22 leads to a reduced surface potential (Φ_{eff}) and is called the Schottky effect, defined by the following equations [15].

$$V_{MAX} = E_F + \Phi - \left(e^3F\right)^{1/2} \tag{2.24}$$

$$\Delta\Phi = -\left(e^3F\right)^{1/2} \tag{2.25}$$

$$\Phi_{eff} = \Phi - \left(e^3F\right)^{1/2} \tag{2.26}$$

2.3.2 Field Emission Tunneling and Fowler-Nordheim Equation for Metals

In order for quantum mechanical tunneling to occur from the Fermi level in the solid through the barrier, the uncertainty in the electrons position must be greater than the width of the barrier at E_F level [16]. Solving equation 2.22 at E_F gives two solutions and the difference between these solutions gives the width (Δx).

$$\Delta x = \sqrt{\left(\frac{\Phi}{eF}\right)^2 - \frac{e}{F}} \cong \frac{\Phi}{eF} \tag{2.27}$$

The Heisenberg uncertainty principle gives the relation between Δp and Δx, where Δp is the uncertainty in momentum corresponding to the barrier height the electron must tunnel through (Φ).

$$\Delta p \times \Delta x \cong \frac{\hbar}{2} \tag{2.28}$$

$$\Delta p = \sqrt{2m\Phi} \tag{2.29}$$

Substituting 2.29 and 2.27 into equation 2.28 and solving for F gives the threshold voltage necessary for filed emission to begin [16].

$$F = \frac{2\sqrt{2m\Phi^3}}{e\hbar} \tag{2.30}$$

Using the above equation a metal surface with a work function of 4.5 eV would require a field $F \geq 3\times10^7$ V/cm in order to initiate appreciable field emission tunneling [16].

The Fowler-Nordheim model of field emission from a metal uses the free particle approximation with Fermi-Dirac distribution at 0K to calculating the probability of electrons tunneling through the reduced surface potential defined above. For calculation of transmission probabilities, the kinetic energy normal to the surface (W) is the relevant parameter and a parameter of the total kinetic energy (E).

$$W = \frac{\hbar^2 k_Z^2}{2m} \tag{2.31}$$

$$E(W) = \frac{\hbar^2}{2m}\left(k_Z^2 + k_Y^2 + k_X^2\right) \tag{2.32}$$

The number of electrons in the energy range W and W+dW that tunnel through the barrier (P(W,F)) is dependent on the initial Fermi-Dirac distribution (N(W)) and the

transmission probability of electrons through the barrier (D(W,F)) where the total current density is the integration of P(W) times electron charge.

$$P(W,F) = N(W)D(W,F)dW \tag{2.33}$$

$$J = e\int_0^\infty P(W,F)dW = e\int_0^\infty N(W)D(W,F)dW \tag{2.34}$$

The initial electron density found in a metal (N(W)) is derived from the Fermi-Dirac distribution ($f(E)$ or $f(E(W))$) and has the following form [17].

$$f(E) = \left(1 + \exp\left(\frac{E - E_F}{k_B T}\right)\right)^{-1} \tag{2.35}$$

$$N(E,W)dE\,dW = \frac{m}{2\pi^2\hbar^3} f(E(W))dE\,dW \tag{2.36}$$

$$N(W)\,dW = \frac{mdW}{2\pi^2\hbar^3}\int_W^\infty f(E)dE \tag{2.37}$$

$$N(W)dW = \frac{mk_B T}{2\pi^2\hbar^3}\ln\left(1 + \exp\left(\frac{E_F - W}{k_B T}\right)\right)dW \tag{2.38}$$

The calculation of the transmission probability (D(W,F)) is greatly simplified by the free electron gas model of the electrons in the metal allowing use of the WKB approximation. The calculation is further simplified by the fact that the reduced surface barrier has two simple roots putting D(W,F) in the closed form below [17,18]

$$D(W,F) = (1 + \exp(Q(W,F)))^{-1} \tag{2.39}$$

$$Q(W,F) = -2i\int_{Z1}^{Z2} \lambda(x)dx \;;\; Z1, Z2 \text{ roots of } \lambda^2(x) \tag{2.40}$$

$$\lambda(x)=\left(\frac{2m}{\hbar^2}\left(W - E_F - \Phi + \frac{e^2}{4x} + eFx\right)\right)^{1/2} \tag{2.41}$$

The transmission probability (D(W)) goes to unity when the kinetic energy normal to the surface (W) goes above a certain level that corresponds to electrons with energy above the barrier height. In lower energy (tunneling) situations commonly found D(W) can be represented by elliptical integrals.

Solving for J gives two integrals because D(W) has a value approximately equal to unity when electrons have energy above the reduced surface barrier and exponentially decaying for electrons tunneling through the barrier. At room temperatures, all electrons originate close to the Fermi level and the integral corresponding to field emission or tunneling dominates over the thermionic emission or D(W) ≅ 1 integral to give the following.

$$J=\frac{em k_B T}{2\pi^2\hbar^3}\int_{-\infty}^{\infty}\exp[-Q(W,F)]\,\ln\left[1+\exp\left(\frac{E_F - W}{k_B T}\right)\right]dW \tag{2.42}$$

Representing Q(W,F) with Nordheim's elliptical function *v* and *t* which are composed of elliptical integrals and solving the integral in equation 2.42 for very low temperatures gives the following equation where Φ is in eV and F is V/Å [17].

$$J=\frac{1.537\times10^{10}F^2}{\Phi t^2\left(3.79F^{1/2}/\Phi\right)}\exp\left[-\frac{0.683\Phi^{3/2}}{F}v\left(\frac{3.79F^{1/2}}{\Phi}\right)\right]\frac{A}{cm^2} \tag{2.43}$$

Converting current density (J) into current (I) and electric field (F) into potential (V) by use of the following equations leads to the final form of the Fowler-Nordheim equation

with the approximation that *v* and *t* are constant over the limited range of F corresponding to turn on of field emission.

$$I = JA \tag{2.44}$$

$$F = \beta V \tag{2.45}$$

$$I = aV^2 \exp\left(-\frac{b\Phi^{3/2}}{V}\right) \tag{2.46}$$

$$\ln\left(\frac{I}{V^2}\right) - \ln(a) = \frac{-b\Phi^{3/2}}{V} \tag{2.47}$$

In the above equations, A is emission area, β is edge enhancement factor corresponding to emission tip sharpness. The parameters *a* and *b* are constants in the Fowler-Nordheim equation, the constant *a* is proportional to emission area (A) and *b* is inversely proportional to tip sharpness (β). It can be seen from equation 2.47 that a plot of $\ln(I/V^2)$ verses 1/V will give a linear relationship and is called a Fowler-Nordheim Plot. Actual field emission data from metals fitted to Fowler-Nordheim plots gives straight lines where the slope of the line is equal to $-b\Phi^{3/2}$. If the tip shape (*b*) is constant, changes in work function (Φ) can be determined from changes in the Fowler-Nordheim Slope, or *b* can be determined if Φ is constant.

2.3.3 Energy Distributions of Field Emission Electrons

The calculation of total energy distributions of field emission electrons originally done by Young utilizes equation 2.34 to 2.41 where the total kinetic energy (E) is integrated over in equation 2.37. However, if this total energy is not integrated out the current density will become energy dependent [12,17].

$$J(E) = e\int_0^E N(W,E)D(W,F)dW \tag{2.48}$$

In the above equation, N(W,E) is defined by equation 2.36 and D(W,F) by 2.39. After some approximation for low temperature field emission, the energy dependent current density becomes [19]:

$$J(E) = \frac{J_0}{d}\frac{\exp\left(\frac{E - E_F}{d}\right)}{1+\exp\left(\frac{E - E_F}{k_B T}\right)} \tag{2.49}$$

$$d = \frac{\hbar eF}{2\sqrt{2m\Phi}\; t\left(e^{3/2}F^{1/2}\Phi\right)} \tag{2.50}$$

where J_0 is the total current density from equation 2.43, T is temperature in K, and *d* is a function of the almost constant Nordheim's elliptical function *t* and electric field (F). Plots of equation 2.49 at different temperature are shown in Figure 2.4 where it can be seen that higher temperatures distribute the sharp onset of field emission energy distribution at 0°K to a more Gaussian structure. It also can be seen from the figure that the onset of the distribution happens at the Fermi level with the vacuum level being the zero voltage reference. Actual field emission energy distribution data fits the theoretical total energy distribution. This demonstrates that electrons coming off a field emission tip after moving a few tip radii away have a velocity vector pointing directly away from the emission tip towards the anode, due to the strong focussing found around a sharp tip [13].

The act of measuring an energy distribution with a hemispherical energy analyzer also distributes the original distribution by multiplying it by a Gaussian (G(E)) that is a function of the full width at half maximum (ΔE) of the energy analyzer [19].

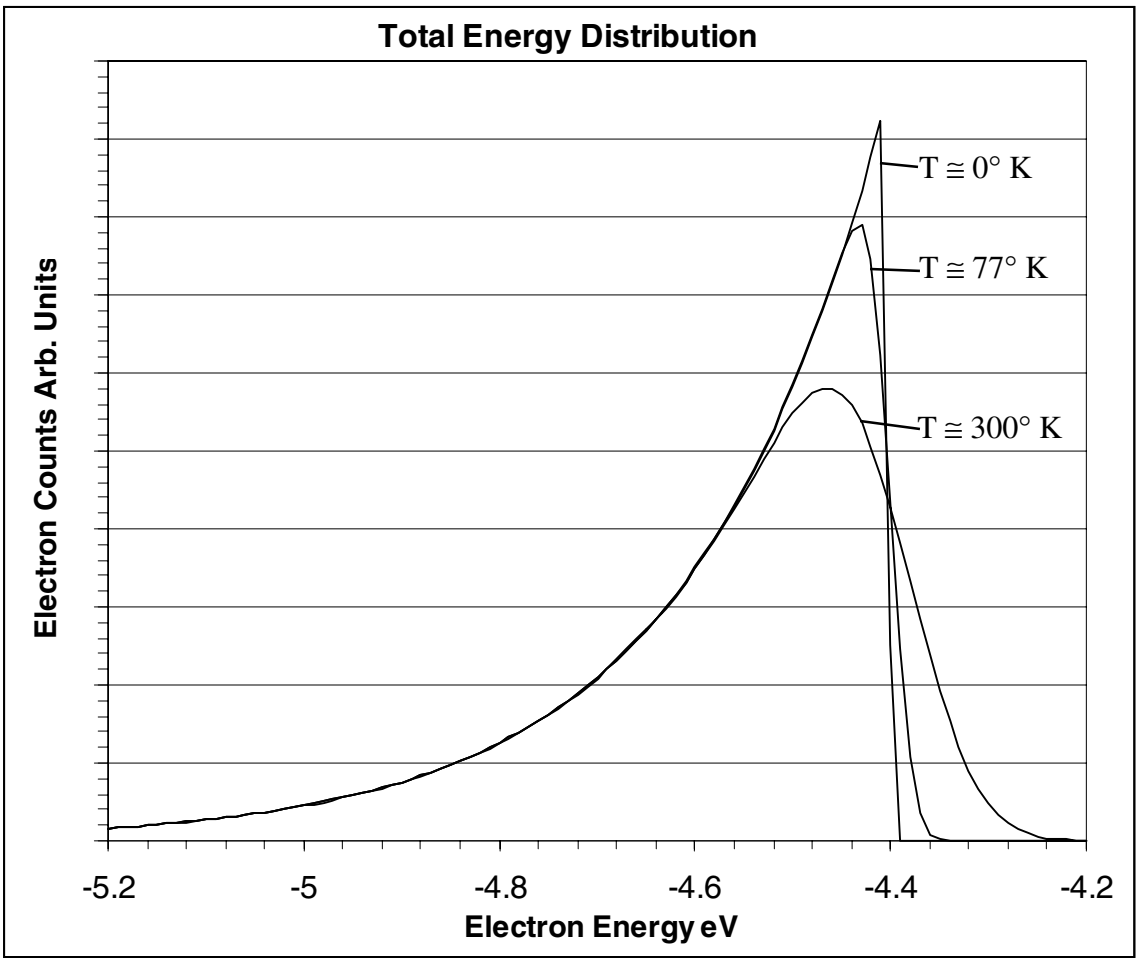

Figure 2.4. Theoretical Electron Field Emission Energy Distributions (FEED) from a metal with temperature ranges from about 0°K to room temperature. This plot is for a material with $\Phi = 4.4$ eV and $F = 4.5 \times 10^7$ V/cm. Actual data fits the theoretical model closely after broadening due to analyzer resolution ($\Delta E/E$).

$$J_{MEASURED}(E) = \int_{-\infty}^{\infty} J(E')G(E'-E)dE' \tag{2.51}$$

$$G(E) = \frac{0.939}{\Delta E}\exp\left(-\frac{2.77\,E^2}{\Delta E^2}\right) \tag{2.52}$$

The effect on the spectra is almost identical to broadening from thermal excitation, Figure 2.4. For 0 °K equation 2.51 can be expressed in closed form where $\Gamma = \Delta E / 3.44$ [20].

$$J_{MES}(E) = \frac{J_O}{2d}\exp\left(-\frac{\Gamma^2}{2d^2}\right)\exp\left(\frac{E - E_F}{d}\right)\left\{1 + \mathrm{erf}\left(\frac{E_F - E - \Gamma^2/d}{\sqrt{2}\Gamma}\right)\right\} \tag{2.53}$$

This equation has the form of a Gaussian possessing an exponential decay to one side called an Exponentially Modified Gaussian. The parameters to this equation are exponential decay rate (*d*), Gaussian width (Γ), area (J_0), and inflection point (E_F). Thermal broadening at low temperature (room temperature and below) can be incorporated with minimal error as an increase in width (Γ). The inflection point in these curves is the point where the second derivative becomes negative on the side of the Gaussian without exponential decay. The location of this inflection point is insensitive to broadening of the Gaussian/exponential decay distribution, and corresponds to the Fermi level. If the sample is a metal and the kinetic energy is referenced to the vacuum level, this inflection point also corresponds to work function, and is the fitting technique used to evaluate field emission energy distribution spectra.

References.

1. A. Einstein, Annalen der Physik, **17**, 132 (1905).
2. W.E. Spicer, Phys. Rev., **112**, 114 (1958).
3. B. Feuerbacher, B. Fitton, and R. F. Willis, *Photoemission and the Electron Properties of Surfaces*, John Wiley, New York, 28 (1978).
4. W.L. Schaich and N.W. Ashcroft, Phys. Rev., **B3**, 2452 (1971).
5. E.O. Kane, Phys. Rev., **127**, 131 (1962).
6. C.N. Berglund and W.E. Spiecer, Phys. Rev., **136**, A1030 (1964).
7. R.H. Fowler, Phys. Rev., **33**, 45 (1931).
8. R.W. Wood, Phys. Rev., **5**, 1 (1897).
9. R.A. Millikan and C.F. Frying, Phys. Rev., **27**, 51 (1926).
10. R.H. Fowler and L. Nordheim, Proc. Roy. Soc. London, **A119**, 683 (1928).
11. A. Sommerfeld, Z. Phys., **47**, 1 (1928).
12. R.D. Young, Phys. Rev., **113**, 110 (1958).
13. R.D. Young and E.W. Müller, Phys. Rev., **113**, 115 (1958).
14. K. Huang, *Statistical Mechanics*, John Wiley & Sons, New York NY, 224 (1963).
15. W. Schottky, Z. Phys., **14**, 63 (1923).
16. R. Gomer, *Field Emission and Field Ionization*, Harvard Univ. Press, Cambridge MA, 6-33 (1961).
17. A. Modinos, *Field, Thermionic, and Secondary Electron Emission Spectroscopy*, Plenum Press, New York, 1-18 (1984).

18. S.C. Miller and H.R. Good, Phys. Rev., **91**, 174 (1953).

19. R.D. Young and C.E. Kuyatt, Rev. Sci. Inst., **39**, 1477 (1968).

20. J.W. Gadzuk, Surface Sci., **15**, 466 (1969).

CHAPTER 3

EXPERIMENTAL TECHNIQUES AND EQUIPMENT DESIGN FOR WORK FUNCTION STUDY

3.1 Introduction

In this chapter, a description of the experimental techniques and apparatus is presented for characterization of field emission materials by examining their work function properties. This study was conducted in two chambers. One chamber examined the field emission characteristics by obtaining simultaneous Field Emission Energy Distributions (FEEDs) and Fowler-Nordheim I-V plots [1,2], and the other chamber obtained Ultraviolet Photoelectron Spectroscopy (UPS) information [3]. Both sets of data can be correlated to work functions of materials studied. The location of the lowest FEED and UPS energy spectral peak gives the work function, and the slope of the Fowler-Nordheim I-V plot also depends on the work function. In this study molybdenum, iridium, and iridium oxide were characterize.

The first apparatus was designed and constructed for this research and measures the FEED, and current versus extraction voltage (I-V) of a field emission tip.

The simulated hemispherical energy analyzer used in FEED measurements is a low cost alternative to commercially built spectrometers, consisting of easily machined cylindrically shaped components that will be detailed later. Two modes of operation were used, in the first mode simultaneous FEED spectra and Fowler-Nordheim plots were obtained. In this mode of operation, the extraction voltage on the anode is stepped, and between each voltage step a complete energy spectra scan in conjunction with current measurements made before going to the next higher voltage. The spectra scan is a FEED spectrum and the current verses voltage measurements used for Fowler-Nordheim plots. The other mode of operation was to keep the extraction voltage constant and take consecutive energy spectra scans along with current readings over extended time periods. This endurance test was conducted to study the emission tip degradation to determine the current change and energy spectra shift after several hours of use. Gases could be introduced during these endurance tests through a leak valve and partial pressures measured with a RGA to evaluate exposure responses of the emission tips. For our particular study oxygen was the gas introduced to evaluate oxidation effects.

The second chamber is a VG ESCALAB MKII, which has been modified to run under PC control, a UV lamp is used to obtain low energy UPS spectra. This instrument allows flat samples to be characterized. A voltage-biased aperture was also fitted to the chamber to conduct field emission studies and obtain FEED spectra to compare with those obtained in the other chamber.

3.2 Field Emission Energy Distribution, FEED / Fowler-Nordheim Chamber

The field emission characterization chamber shown in Figure 3.1 is a stainless steel Ultra High Vacuum (UHV) chamber, with of an 8-inch diameter ConFlat flange cross as the main chamber. There is a 350 cfm turbo molecular pump and 40 L/sec ion pumps attached to the right of the cross, attached to the left of the cross is a 300 L/sec ion pump. The turbo pump is attached to the main chamber through a bellows to isolate vibration from the main chamber. A gate valve between the turbo pump and main chamber is used to close off the main chamber and a turbo molecular pump to allow pumping exclusively from the vibrationless ion pumps. Base pressure is measured by a glass encapsulated ion gauge, with a chamber base pressure of less than 1×10^{-9} Torr. A sapphire sealed variable leak valve is used for gas introduction. A residual gas analyzer (RGA) manufactured by SRS is used to measure partial pressures of ambient gases and gases introduced through the leak valve.

3.2.1 Field Emission Tip Manipulator and Positioning

A high precision XYZ and theta motor driven UHV manipulator is used to position the field emission tips over the extraction aperture (anode electrode). This is attached to the top of the UHV cross. Up to four tips may be mounted to this manipulator at a time. The manipulator is a Huntington MPM-600-RM with a position resolution of 0.002 mm and six MHV electrical feedthroughs for contact to the emission tips. The stepper motors used to position the emission tips are controlled by RS-232 serial ASCII commands that can be typed into a hand held unit.

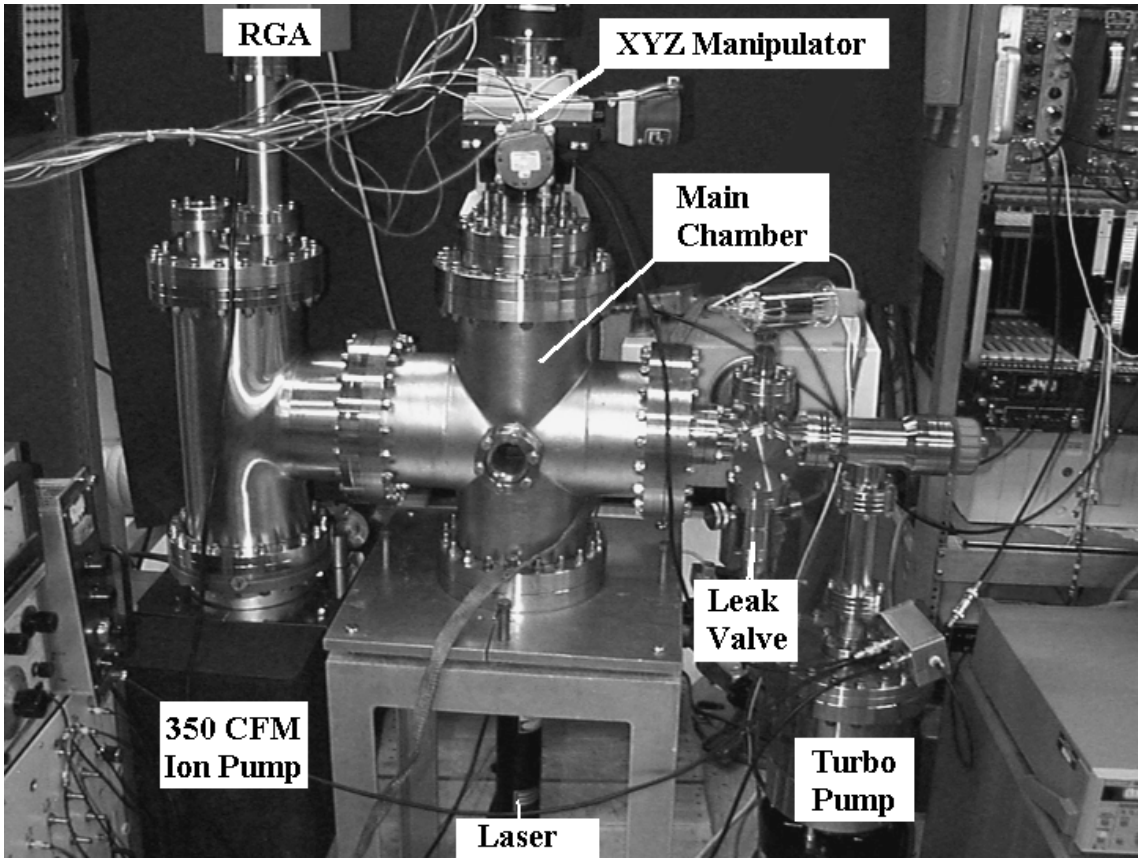

Figure 3.1. Picture of FEED/Fowler-Nordheim chamber. The power supply rack is on the left side, and the electronics rack is on the right side.

A view port is located above the extraction aperture so that approximate positioning of a field emission tip can be viewed. A He-Ne laser is used to help in tip positioning. The laser beam passes directly through a view port located on the bottom of the UHV cross, through an opening in the energy analyzer and lens system below the extraction aperture. This laser beam illuminates the aperture form below, the side opposite the field emission tip. Thus, the laser light passing through the aperture illuminates one of the field emission tips when it is directly over the aperture opening.

Fine positioning of a tip is accomplished after approximate positioning by optimizing the measured field emission current coming off one emission tip, and maximizing the electron count rate at the detector after energy analysis. An initial energy scan gives the general location and structure of the emission spectra and peak at a reduced count rate. Then fine positioning is done at a constant extraction voltage on the aperture, and with the energy analyzer detecting electrons at a kinetic energy that is approximately centered on the FEED peak of the tip positioned over the aperture.

3.2.2 Energy Analyzer Overview and Extraction / Lens System and Simulation

Shown in Figure 3.2 is a compact extraction and collimating lens system followed by a simulated hemispherical energy analyzer and channel plate detector. This energy spectrometer is attached to the bottom of the UHV cross. All parts of this detection system were manufactured from oxygen free copper. The extraction lens has an aperture with an opening of 0.012 inches to create a high electric field to induce field emission from a sharp tip when it is placed close to the aperture and sufficient voltage is applied.

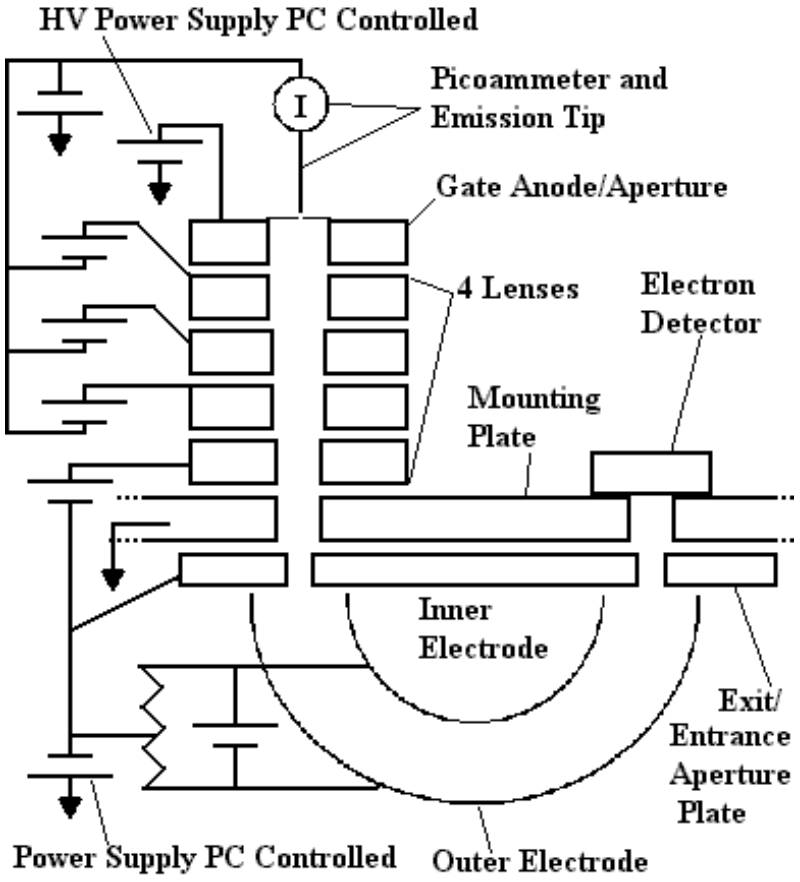

Figure 3.2. A diagram of the FEED energy analyzer electrodes and how the voltage power supplies are wired to them. Two power supplies are computer controlled, one controls emission field strength, the other controls electron energy detected.

The aperture is tapered to a sharp edge to minimize collisions and inelastic interactions with the extracted electrons. After the aperture the electron beam passes through a set of four collimating and focusing electrostatic lenses that were modeled using the program Simion [4] to maximize the amount of divergent electrons that can enter the energy analyzer. The diameter of each pair of lenses decreases as the electron passes from the extraction tip to the energy analyzer entrance. This change allows good focusing and electron throughput but minimizes the inelastic interactions between electrons and surfaces of the lens system. This configuration was determined to be the optimal after extensive modeling of the system using Simion. A plot of modeled electron trajectories is shown in Figure 3.3.

A mounting plate is located after the lens system, and is supported by four threaded connecting rods that are mounted into a ConFlat flange that is bolted to the bottom of the UHV main chamber cross. The plate has two openings that align with the entrance and exit apertures of the energy analyzer. The extraction anode and lens system are mounted on top of this plate over the energy analyzer entrance aperture. The simulated hemispherical energy analyzer is mounted under the plate, and the channel plate detector is mounted on top of the plate over the exit aperture of the energy analyzer.

3.2.3 Simulated Hemispherical Energy Analyzer

The energy analyzer is a simulated 180-degree spherical spectrometer as reported by K Jost in 1979 [5]. The analyzer achieves hemispherical fields by using a small number of cylindrical, conical, and disk shaped electrodes that do not require any

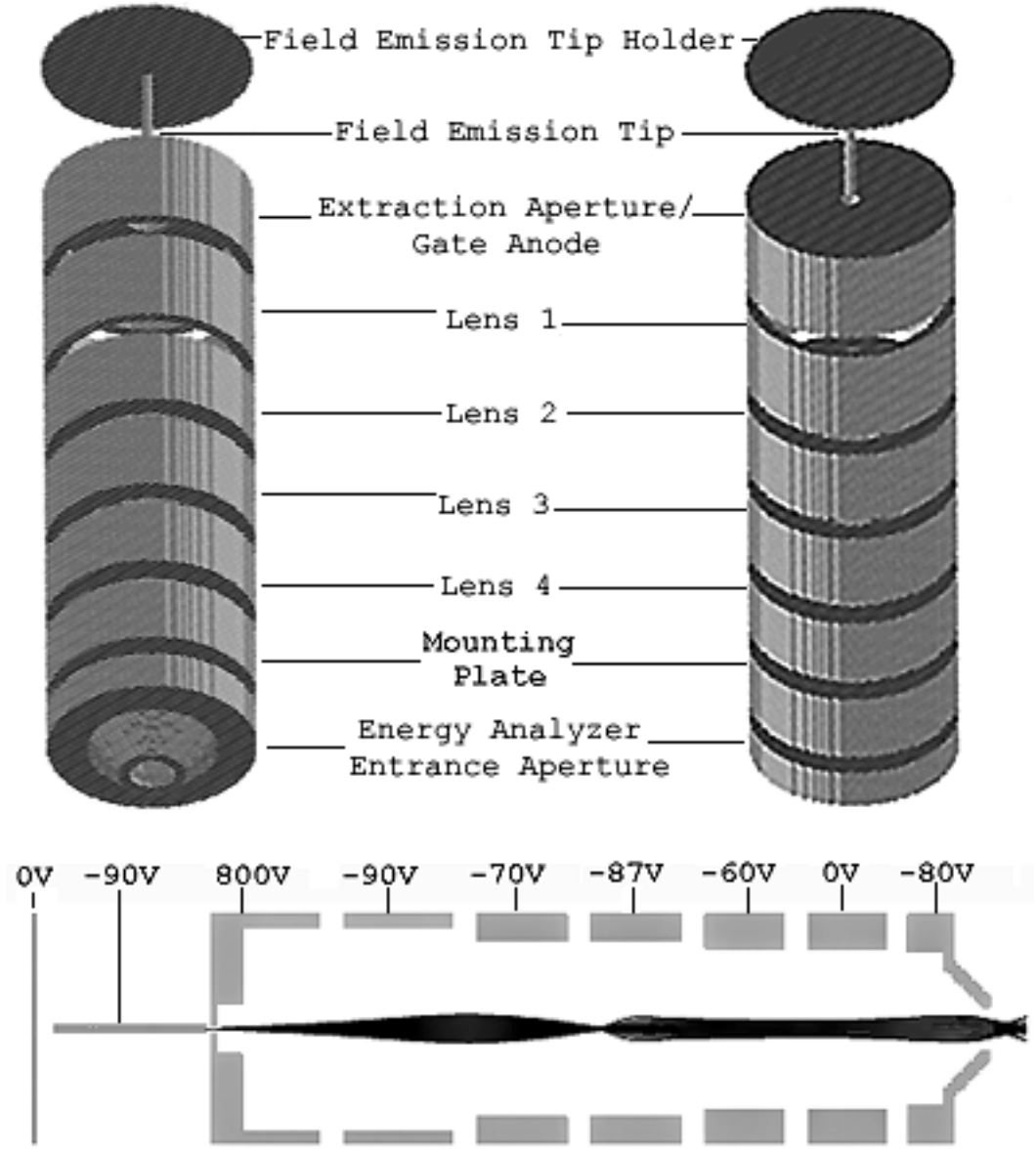

Figure 3.3. Top figure is a 3D Simion geometric model of the lens system, apertures, and emission tip. The lower model is a cut away view of this system with operating voltages applied to each element. These voltages are very close to the standard operating voltages. The central beam simulates an 85 eV electron beam with +/- 5 degrees spread in trajectory.

specialized machining tools or techniques that are required for a true hemispherical energy spectrometer. This detector is composed of a base plate electrode that contains entrance and exit apertures for the analyzer, a cylindrically shaped inner electrode, a cylindrically shaped outer electrode that is made from wire mesh supported by two half disk plates, and two half disk auxiliary electrodes located between the inner and outer electrodes, as shown in Figure 3.4. The dimensions of the energy spectrometers are 2.56 inches for the outer electrode diameter, 1.6 inches for the inner electrode diameter and 2.08 inches diameter for the electron beam path. The entrance and exit apertures have a diameter of 0.16 inches. For the geometry and dimensions above, by correctly biasing the auxiliary electrodes relative to the inner and outer electrodes an electric field that mimics a true hemispherical energy analyzer with hemispherical shaped inner and outer electrodes is produced. Jost has determined the parameter p, which is a function of the voltage placed on the analyzer's electrodes.

$$p = \frac{\left(V_{aux} - V_{outer}\right)}{\left(V_{inner} - V_{outer}\right)} \tag{3.1}$$

The value of p=0.4 creates electric fields in the energy analyzer that mimic a hemispherical energy analyzer with a radial electric field that falls off as $1/r^2$ ($E \propto 1/r^2$). If p=0.76 then the analyzer mimics a cylindrical energy analyzer with a radial electric field that falls off as 1/r ($E \propto 1/r$). For a hemispherical application the following equations apply.

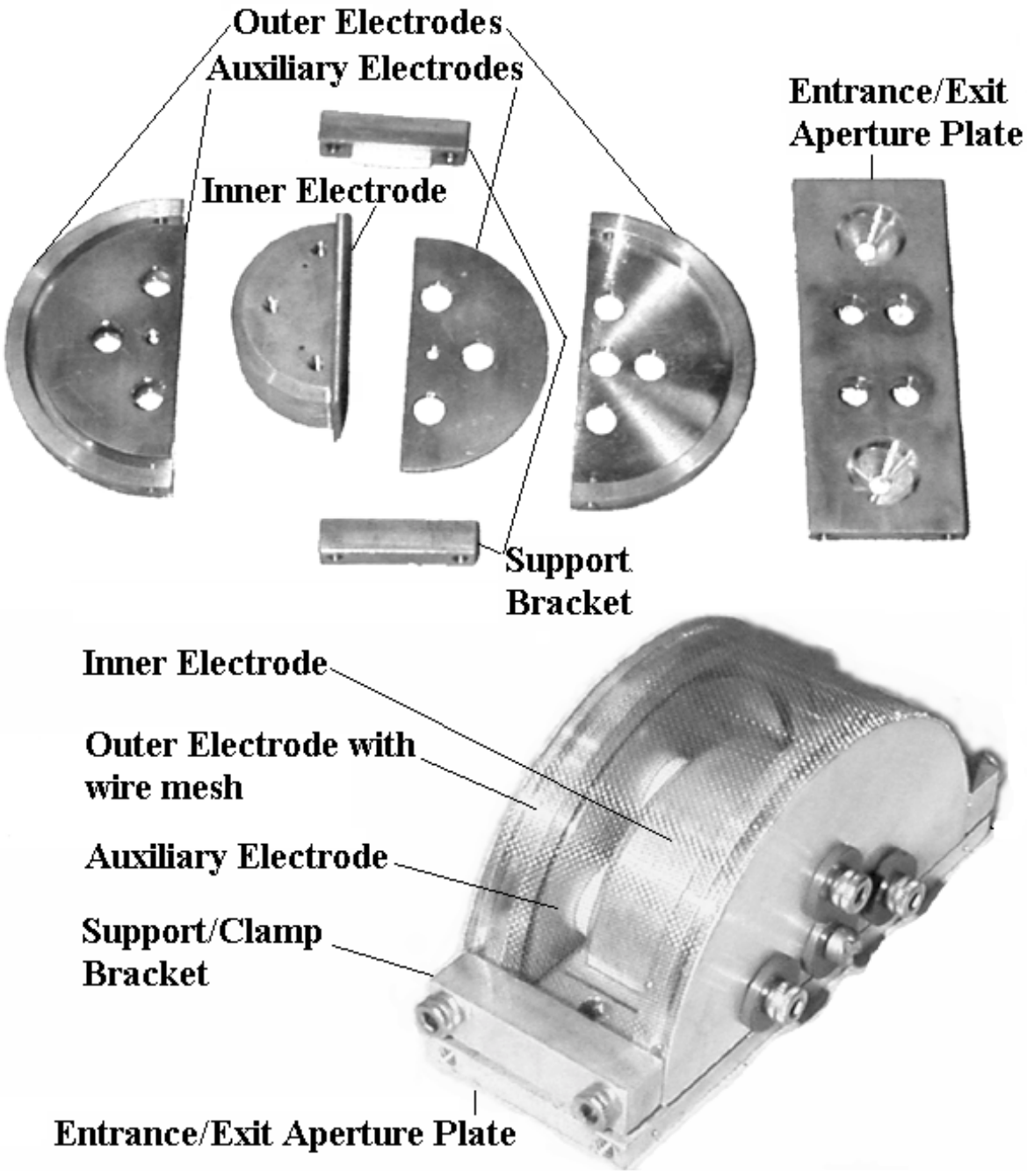

Figure 3.4. Top figure shows energy analyzer disassembled displaying all machined electrode pieces. Bottom figure shows analyzer assembled with necessary bolts and insulating ceramic washers. Bottom picture is slightly larger than actual size.

$$0.4 = \frac{(V_{aux} - V_{outer})}{(V_{inner} - V_{outer})} \tag{3.2}$$

$$V_{aux} = 0.4(V_{inner}) + 0.6(V_{outer}) \tag{3.3}$$

$$\Delta V = (V_{inner} - V_{outer}) \tag{3.4}$$

$$V_{aux} = 0.4(\Delta V) + V_{outer} \tag{3.5}$$

Note that for electron or negatively charged energy analysis the inner electrode will be more positive (attractive) than the outer electrode, thus $\Delta V > 0$. From the equations above a voltage divider between the inner and outer electrode voltage (ΔV) that is 40% above the outer sphere voltage and 60% below the inner sphere will give correct bias to the auxiliary plates to run in hemispherical applications.

After biasing the auxiliary plates to simulate hemispherical ($E \propto 1/r^2$) fields the parameters of the energy analyzer were determined by applying the standard 180^{o} spherical electrostatic spectrometer equations to the dimensions of the analyzer, with one minor adjustment. As previously stated the inner electrode is 1.6 inches in diameter, the beam path is 2.08 inches in diameter, and the apertures are 0.16 inches in diameter. However, the outer electrode is composed of mesh grid that allows field penetration and makes the outer electrode seem father away. Therefore, this diameter was approximated to be 2.6 inches versus 2.56 for the calculations. This approximation has physical relevance and allows the base plate containing the entrance and exit apertures to be at the same potential as the auxiliary plates, as determined by the following equations derived by Kuyatt and Simpson [6]. In the following equations R_1, R_0, R_2, are inner sphere, beam

path, and outer sphere radii, ΔV is the potential between inner and outer spheres, and V_0 is the kinetic energy in electron volts of electrons that travel through the detector at radius R_0, and is also the attractive potential place on the base plate (V_R) in the particular case of measuring electrons from a source of zero voltage reference.

$$\Delta V = V_0\left(\frac{R_2}{R_1} - \frac{R_1}{R_2}\right) \quad ; \quad \Delta V = V_0(1.0) \tag{3.6}$$

$$V_{inner} = V_0\left[3 - 2\left(\frac{R_0}{R_1}\right)\right] \quad ; \quad V_{inner} = V_0[0.4] \tag{3.7}$$

$$V_{outer} = V_0\left[3 - 2\left(\frac{R_0}{R_2}\right)\right] \quad ; \quad V_{outer} = V_0[1.4] \tag{3.8}$$

Note for this particular application, electrons have a negative charge so V_{outer} having a higher potential would be more negative. Substituting V_{inner} (equation 3.7) and V_{outer} (equation 3.8) into equation 3.3 gives the auxiliary plates the same potential as the base plate.

$$V_{aux} = V_0 \tag{3.9}$$

The resolution of the analyzer is determined by the ratio between the diameter of entrance and exit apertures to the diameter of the beam path ($2R_0$). Kuyatt and Simpson have calculated the energy resolution given below [6]. Where ΔE is the full width at half-maximum energy distribution, E is the pass energy (V_0), ω is the entrance and exit aperture diameter and R_0 is the beam radius.

$$\frac{\Delta E}{E} = \frac{\omega}{2R_0} \quad ; \quad \frac{\Delta E}{E} = \frac{1}{13} \tag{3.10}$$

To scan an energy range, a fixed voltage was placed across the inner and outer electrodes of the spectrometer so that electrons' energy going through the analyzer (E or V_0) was a constant, and the whole spectrometer's reference voltage (V_R) was varied to retard electrons entering the analyzer at the base plate. This variation in retardation allows the unit to scan over an energy range with a fixed energy resolution (ΔE) and is known as Constant Analyzer Energy mode.

3.2.4 Data Acquisition Hardware and Software

The PC based data acquisition and control is shown in Figure 3.5. It was programmed using HP-VEE graphics based data acquisition software [7]. The PC is connected to a CAMAC crate and Keithley 486 picoammeter via a GPIB interface. The picoammeter is connected between a field emission tip and bias power supply to obtain the field emission current from the tip. The CAMAC crate receives the electron counts from the channel plate detector located after the exit aperture of the energy analyzer, and the CAMAC crate sends out two DAC voltages that control the power supplies for the extraction or gate anode, and the energy analyzer base plate (retarding voltage). In normal operation, the DAC sets the voltage on the extraction anode and then steps the base plate (retarding voltage) to scan electron energies of interest. During the energy scanning steps, a dwell time of approximately five seconds is used. During this time, channel plate counts are summed and a current reading measured before stepping to a higher energy. The average of the current readings is used to construct a Fowler-Nordheim I-V plot and the accumulated counts are plotted to obtain FEED spectra.

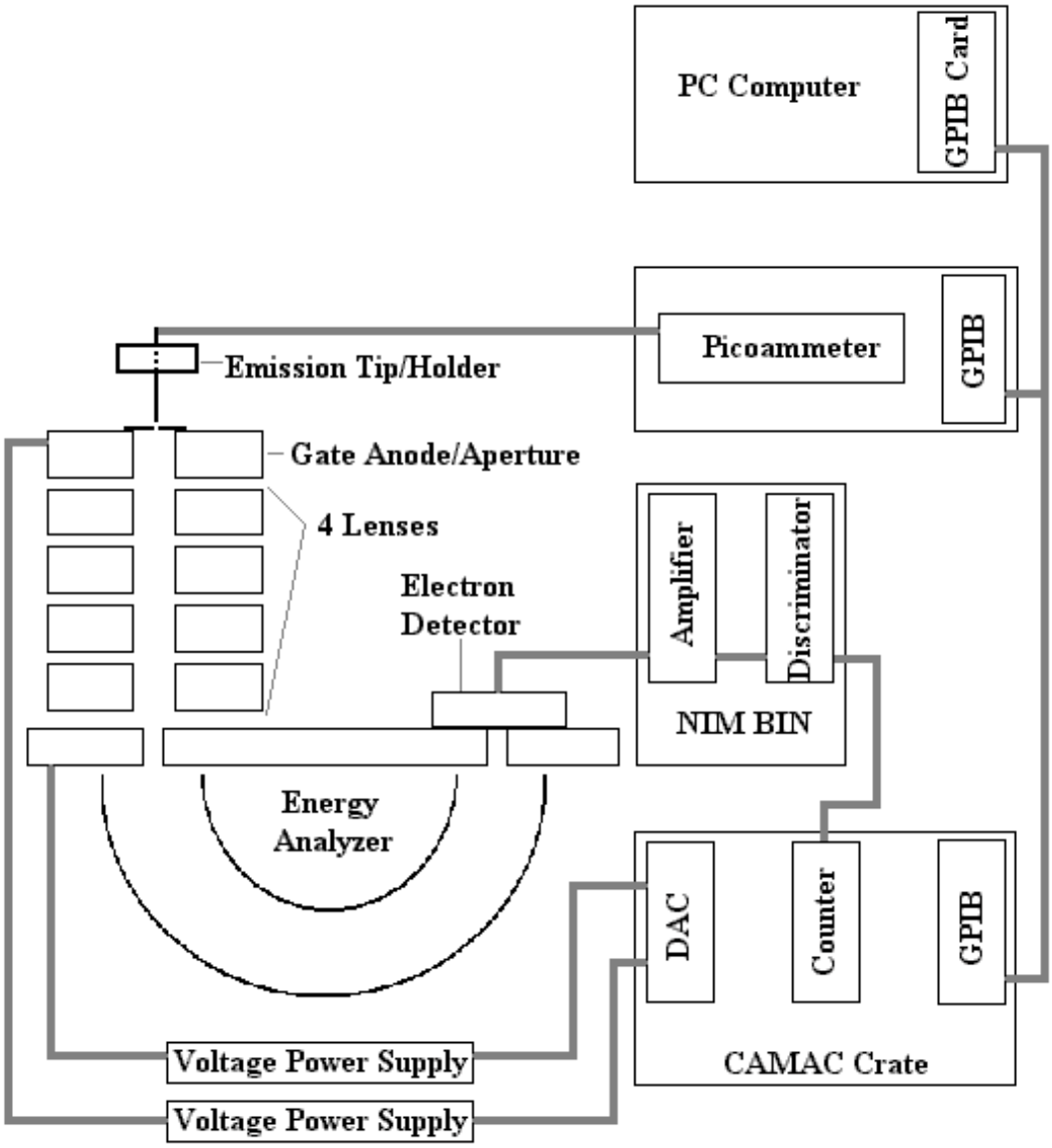

Figure 3.5. A simple electronic diagram of how the FEED chamber's electronic data acquisition and control is arranged. The individual electrons are detected by a channel plate electron detector, and current is measured off the emission tip. Two power supplies are voltage controlled. One power supply regulates the electric field applied to the tip, and the other sweeps the electron energy that is allowed through the energy analyzer into the electron detector.

At the end of this scan the extraction anode steps up in voltage and another FEED scan taken under higher extraction field conditions. The process is almost identical in endurance mode except the extraction voltage remains constant and scans are repeated at a constant electric field, while the emission tip is exposed to an ambient gas of interest. In this mode of operation, the gases' partial pressure is measured by an RGA serially connected to the PC.

3.2.5 Energy Analyzer and Equipment Characterization

To characterize the energy analyzer system a Tungsten filament was centered in the extraction electrode opening with the aperture removed. The filament was biased at - 90 volts and approximately 2 volts across the filament to obtain thermal emission. The energy spectrometer was scanned through the energy range at different values of voltage placed between the inner and outer electrodes (1V, 4V, 5V, 6V, and 10 V). As the voltage was changed between inner and outer electrodes (ΔV) a linear shift of the spectra maximum relative to the base plate retarding voltage (V_R) occurred. A straight line was fitted to the data and the line slope used to determine the analyzer constant (K) to be 1.05.

$$KE_{electron} = V_R + K \times \Delta V \quad ; \quad K = 1.05 \tag{3.11}$$

This value of 1.05 is close to the calculated value of 1 for a spherical energy analyzer. This K value was also measured from field emission spectra while varying the ΔV between 5 and 20 volts. The linear fit also gave a value of 1.05 for K. Figure 3.6 shows spectra of thermal and field emission calibration results.

To examine the transmission function of the energy analyzer, different voltages

were applied to a tungsten filament and a molybdenum field emission tip while energy spectra were obtained. The spectrum was examined for changes in count intensity and to make sure that the retarding aperture and lens system did not distort the spectral results, as shown in Figure 3.7. These results demonstrate the transmission function is flat over the energy range of 80 to 95 eV and that the energy scale is accurate over this energy range. Note that all data was taken in the energy range of 80 to 90 eV.

3.2.6 Preparation of Field Emission Tips

Emission tips were made of 0.02-inch diameter Molybdenum wire electrolytically etched in a 2% KOH aqueous solution. A positive 10V or greater was applied to the Molybdenum wire for etching. This etch would give a tip radii of approximately 10 μm. Smaller radii could be obtained, but this size provided good emission and minimized geometric change due to ion sputtering under high emission conditions. The tips were crimped between two grooved ceramic plates for mounting on the manipulator. Four tips could be mounted at one time and the XYZ manipulator bolted to the main chamber for pump down. SEM images were taken before and after field emission studies, and it was determined that tip geometry mostly remained stable, however if the pressure was above 1×10^{-7} Torr and high emission current or sparking was observed tip degradation occurred.

3.2.7 Field Emission Results and Conclusions

A FEED spectrum and simultaneous Fowler-Nordheim I-V characteristic are shown in Figure 3.8. This data is for a - 90-volt bias applied to a molybdenum tip with the extraction anode ramped between 640V and 880V in steps of twenty volts.

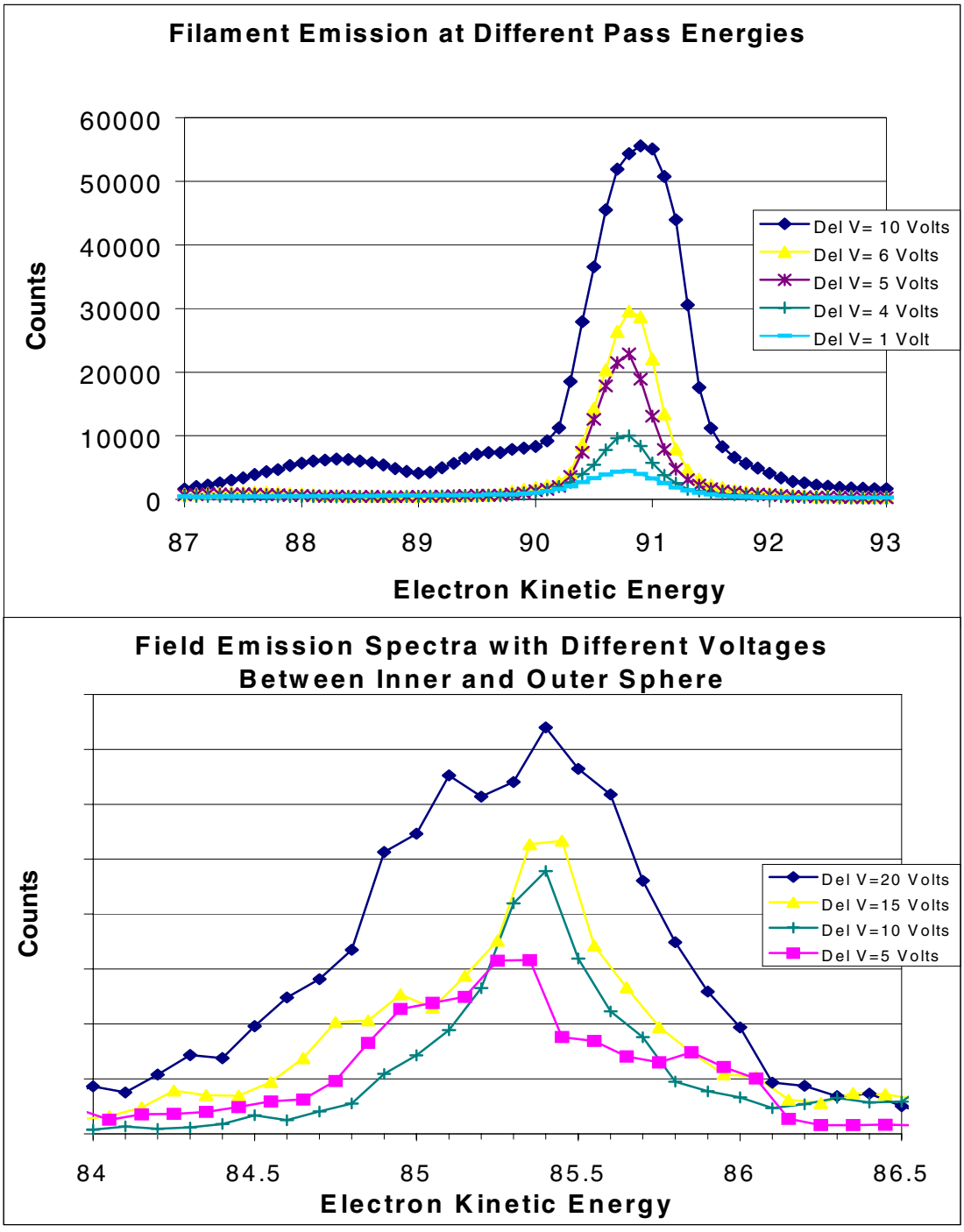

Figure 3.6. Top figure is spectra from a hot Tungsten filament. Lower figure is field emission spectra from a coated Molybdenum tip. Electron Kinetic Energy (KE) is $KE = V_{base} + K \times \Delta V$, V_{base} is the base plate voltage, K is the analyzer constant = 1.05, and ΔV is the voltage difference between inner and outer sphere.

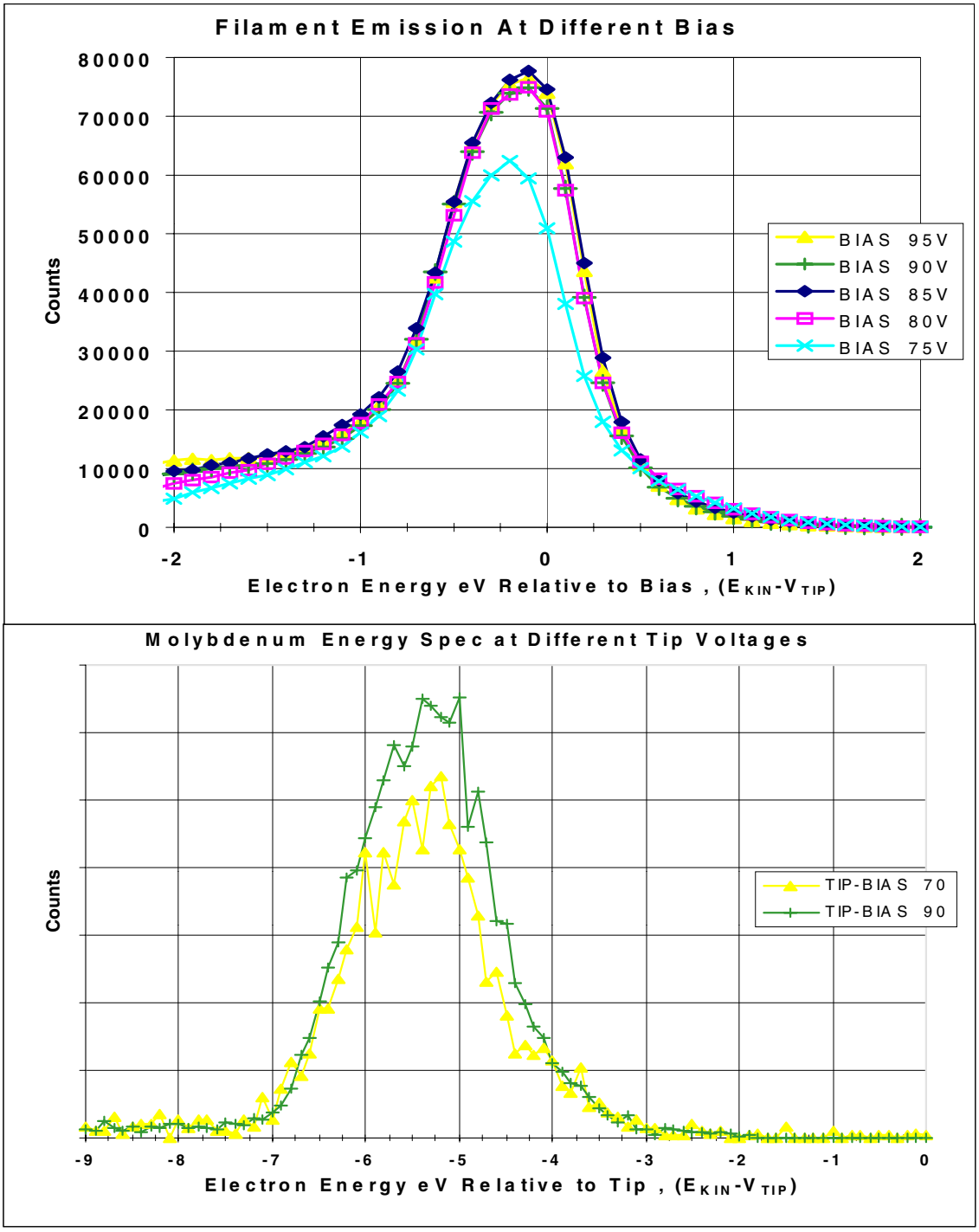

Figure 3.7. Emission spectra at different biases: top a Tungsten filament, and below a Molybdenum FE tip at different tip biases. Electron Energy is kinetic energy in eV minus the voltage applied to the tip.

The energy analyzer had 7 volts between the inner and outer electrode giving the analyzer a pass energy of 7.35 eV. The energy distribution is the kinetic energy of emitted electrons relative to the voltage applied to the tip. This spectrum shows a work function of approximately 4.6 eV, which is the accepted value for polycrystalline molybdenum [8]. The UPS data shown later in this chapter also agrees with this result.

The VG ESCA LAB MKII, which will be described below, was modified to study field emission by mounting a voltage bias aperture in the chamber and mounting an emission tip on the sample holder. The chamber's energy analyzer was set to scan electrons with a fixed energy resolution in constant energy analyzer (CAE) mode with electrons of 5 eV passing through the hemispherical energy analyzer. The emission tip was biased to – 60V and the aperture (gate anode) was biased to 700V. After centering the tip in the aperture and measuring the field emission current, FEED spectra was obtained, shown in Figure 3.9. As before, the energy distribution is kinetic energy of emitted electrons relative to the voltage applied to the tip. As can be seen, the spectra agree with those given in Figure 3.8 and Figure 3.7. This demonstrates that our FEED instrument made from much less expensive components is an accurate spectrometer and comparable to an expensive commercial unit.

The work function of Molybdenum for particular lattice planes falls in the range of 4.36 eV for the (112) plane to 4.95 eV for the (110) plane, and 4.6 eV for polycrystalline molybdenum [8]. All our data for clean molybdenum falls in this range.

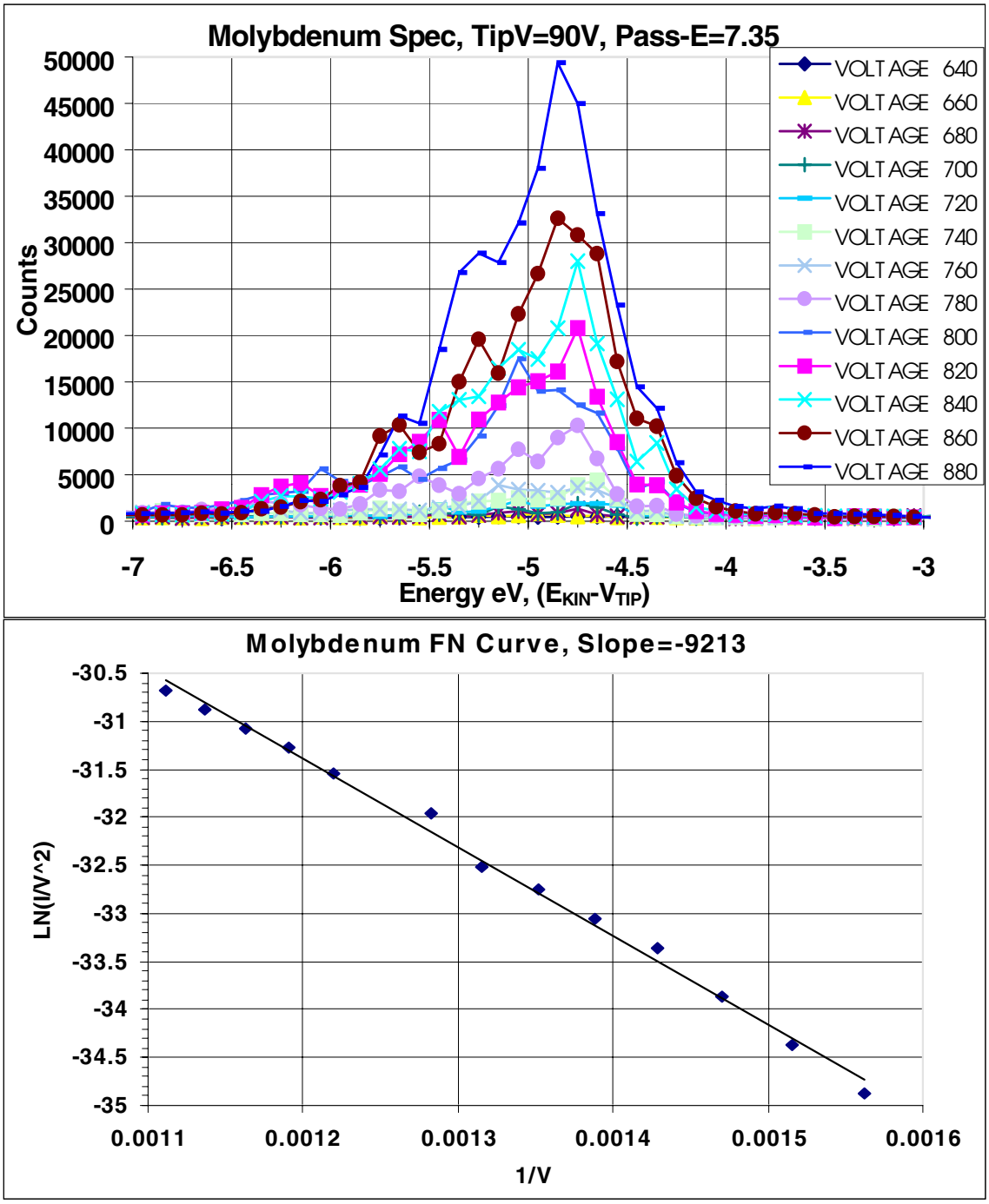

Figure 3.8. Field emission spectra and simultaneous Fowler-Nordheim plots from a Molybdenum tip using the custom built FEED/Fowler-Nordheim chamber.

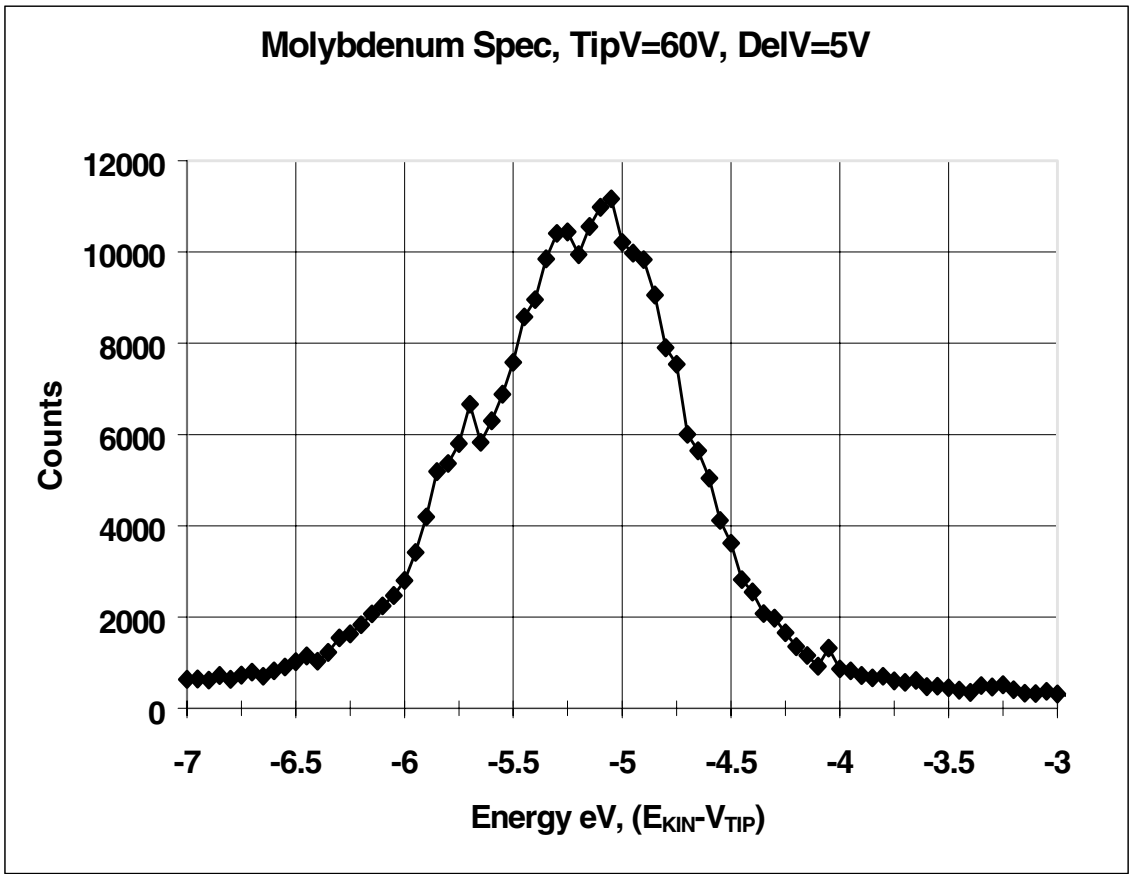

Figure 3.9. Field emission spectra from a Molybdenum tip using the commercial VG ESCA LAB MKII chamber.

3.3 VG ESCALAB Mark II Spectroscopy Chamber

Figure 3.10 is a picture of the experimental apparatus used to obtain UPS data and the field emission data shown above. This analytical system is a commercial Ultra High Vacuum system designed to obtain electron spectra for surface analysis. There are four excitation sources on the chamber to excite electrons from samples; the sources are a 10 kV electron gun, an X-ray source with Aluminum or Magnesium K alpha photons, and two UV sources detailed below. The energy analyzer is a hemispherical design with a beam path radius of 6 inches, with a resolution constant ($\Delta E/E$) of 0.04 or less depending on what size entrance and exit apertures are used. The aperture size can be adjusted on this expensive energy analyzer. The main chamber is spherical and made of UHV stainless steel with all ports pointing to the center where the sample is positioned with an XYZ and theta manipulator. To place samples in the main chamber a small introduction chamber is used that can be brought up to atmosphere while the main chamber remains under vacuum.

3.3.1 VG ESCALAB Mark II Spectroscopy Chamber Modifications

There have been a number of modifications to enhance the system. These modifications consist of, replacing an oil diffusion pump with a 450 L/sec ion pump and sublimation pump with cold trap, addition of a UV lamp with monochromator, a plasma discharge high energy UV source, PC control system, and field emission gate anode assemblies. The main chamber can obtain and maintain a pressure under 1×10^{-9} Torr without bake-out, with ultimate pressure below 1×10^{-10} Torr.

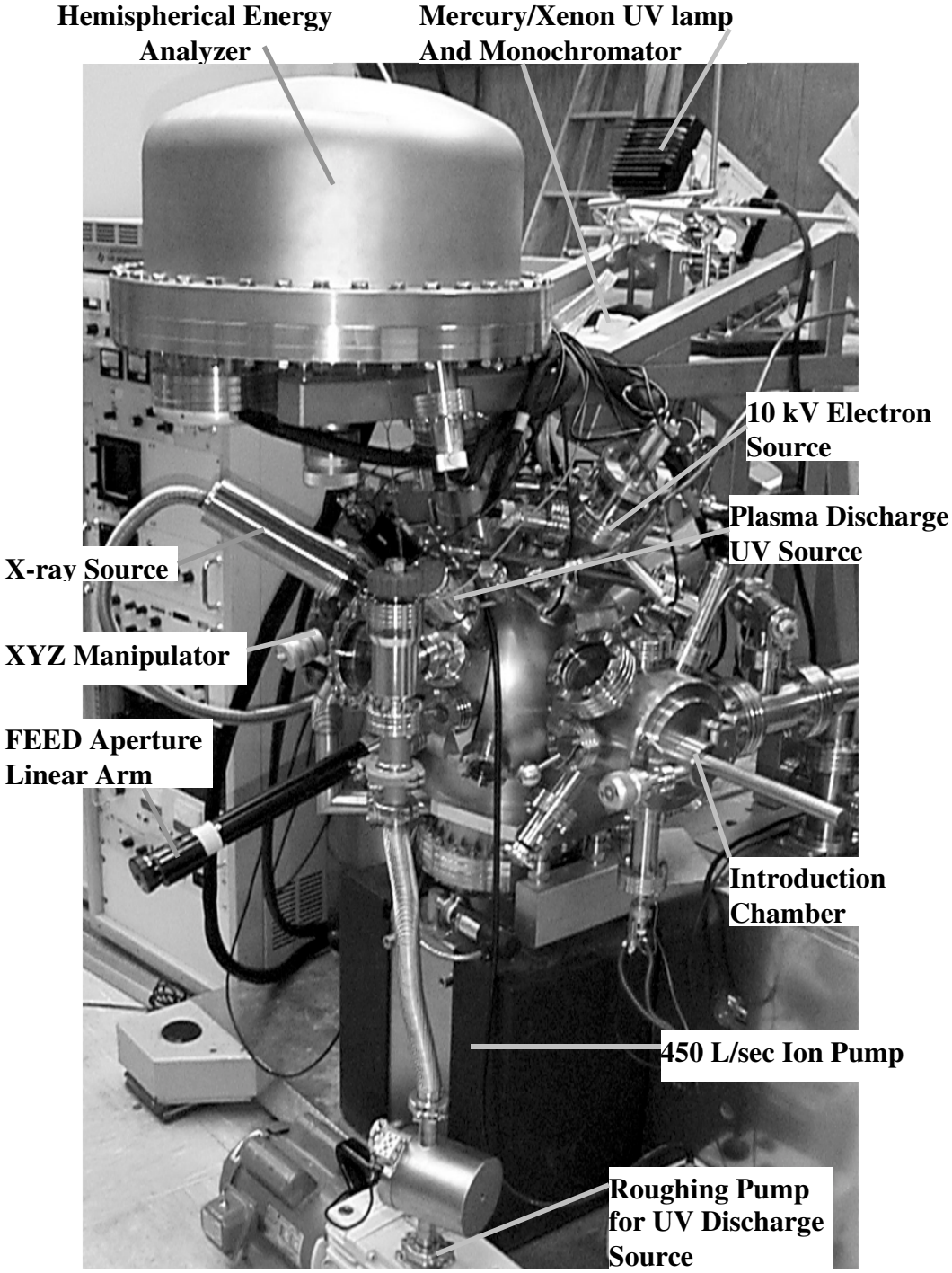

Figure 3.10. VG ESCA LAB MKII chamber used to obtain UPS data and field emission spectra for comparison with custom built chamber. All major components are labeled, with control rack to the left.

The two UV sources were added to measure work functions and band gaps. The near UV light source consists of a Mercury/Xenon discharge lamp, monochromator, quartz focusing lenses, and a quartz UHV view port to allow focused monochromatic light on a sample. This source gives photon energies close to the work function of most materials. The plasma discharge source is directly connected with the main vacuum chamber and has two pumping stages. This source creates plasma, usually of a noble gas and the UV discharge is focused directly on the sample through a capillary tube that extends into the analytical chamber close to the sample. The most common used gas is helium, which emits 21.2 eV and 40.8 eV photons. These high-energy photons can probe the band structure of materials liberating electrons from deep in the valence band.

Figure 3.11 shows a schematic of the computer upgrade to a Pentium PC based system using HP-VEE graphics based data acquisition software. The PC communicates to the energy analyzer power supplies via a VXI crate with TTL digital IO. The connection between PC and VXI crate is over a GPIB interface. The energy analyzer is scanned by sending a 15-bit binary number to the power supplies, controlling the energy analyzer with the binary number being proportional to the energy scanned. Three digital IO bits control the pass energy, with values ranging from 2 eV to 200 eV. Two digital IO bits control the energy range that is scanned by the 15-bit binary number, these ranges go from 0 eV to 82 eV, 164 eV, 1640 eV, and 3280 eV. Between each analyzer setting counts are summed from three channeltron detectors located after the energy analyzer. These counting pulses pass directly to a counter board plugged into the PC, while the

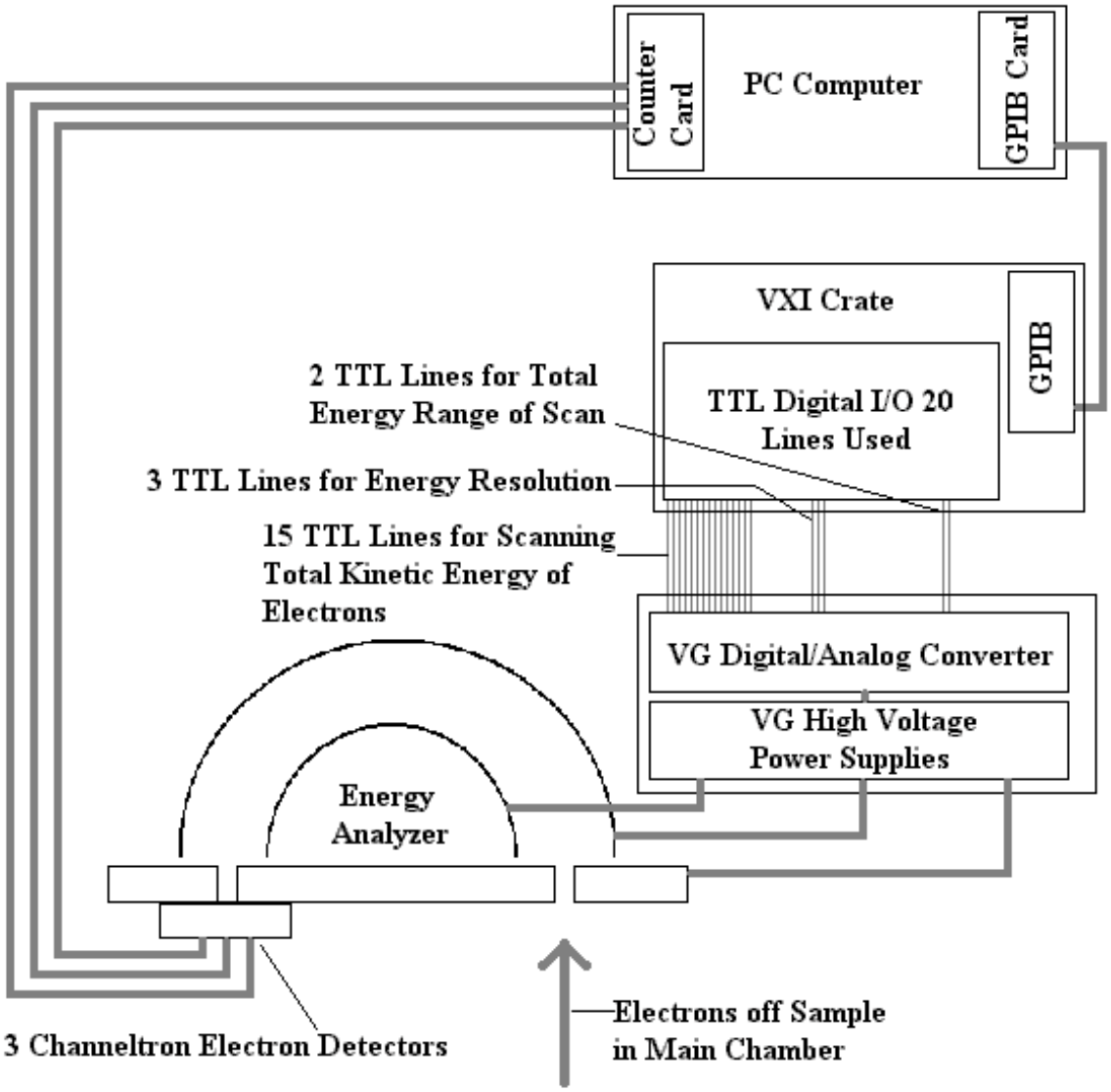

Figure 3.11. PC based electronic data acquisition system for VG ESCA LAB MKII chamber, used to obtain electron energy spectra.

dwell time is controlled by HP-VEE software. The upgrade to a PC from a DEC PDP-11 facilitates data analysis with an abundance of PC based software for data analysis. To scan electron spectra the program sends a total of 20 digital IO bits to the energy analyzer power supplies over a standard computer ribbon cable and clears the counters, then the counters sum for the desired dwell time and after this allotted time store the counts. This process is repeated for each energy step in the spectral scan, and the resulting spectra displayed on the PC.

To conduct field emission studies, an aperture was mounted on a linear motion UHV arm with ceramic bolts and washers to electrically isolate it. The aperture is oxygen free copper and has 0.012 inch diameter opening, similar to the one used in the custom built chamber. The linear motion arm extends to position the aperture in the center of the spherical analysis chamber for field emission experiments. After centering the tip relative to the aperture opening and applying voltages to the tip and aperture, FEED spectra can be acquired.

3.3.2 UPS Results from VG ESCALAB Mark II Spectroscopy Chamber

For this research, the VG chamber was mainly used to acquire UPS data for work function determination. To characterize work functions, a flat sample made of or coated with a material to be evaluated is introduced into the main chamber via the side introduction chamber. The Mercury/Xenon UV source is turned on and the monochromator set to pass visible light to the sample. First the lenses are positioned to maximize the light hitting the sample then the monochromator is set to pass UV light.

Minor adjustments can be made to the lenses to maximize the count rate seen at the channeltron detectors. This procedure was used on molybdenum and surfaces coated with iridium oxide to characterize their work functions. The UPS result from a molybdenum sheet is shown in Figure 3.12 where the energy scale is in binding energy, a gaussian fit with background subtraction gives a mean of 4.65 eV in close agreement with our FEED data.

3.4 Data Analysis and Analytical Software

The computer programs that control the equipment during data acquisition record the data output to files in ASCII format. The data is presented in columns, with the first column equal to the measured parameter for example electron energy or electric potential applied for field emission and the second column equal to the measured result for example electron counts or current. This data can easily be introduced into other programs for data analysis and presentation.

For electron energy spectral data (FEED and UPS data) the program Peakfit was used to fit the spectral results [9]. This program is very useful in fitting data curves with various well-defined peak functions. The measurement of energy spectra distorts the true spectra by introducing a Gaussian distribution characteristic of the energy analyzer.

For UPS data Gaussian functions were used in fitting, and for FEED data Exponentially Modified Gaussian functions (EMGs) were used. The theoretical model used for the spectral distribution (chapter 2) determined the function used for fitting. For UPS (in particular direct optical transition UPS) the theoretical distribution is highly

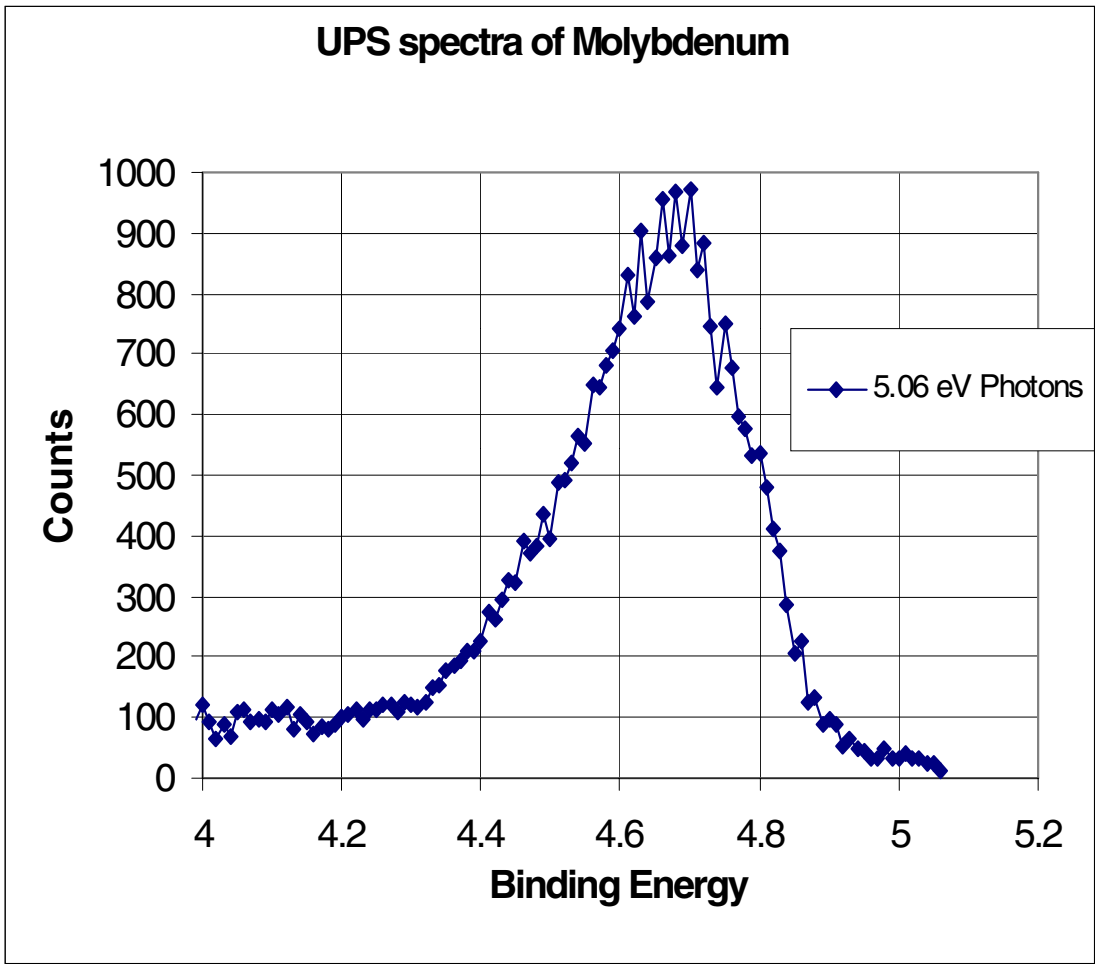

Figure 3.12. UPS spectra from the ESCA LAB MKII chamber of a Molybdenum sheet using 5.06 eV energy photons to excite the sample. A gaussian fit of the energy distribution gives a mean of 4.65 eV for the work function.

localized at a particular electron energy. Therefore, measurement of this localized distribution with an energy analyzer introduces a Gaussian distribution, where the mean corresponds to the localized theoretical distribution. For FEED results, the theoretical model predicts that the spectra should have a sharp onset at the Fermi level and then decay exponentially. Therefore, EMGs are used (chapter 2 equation 2.53), where the inflection point of the EMG on the side opposite the exponential decay corresponds with the theoretical onset.

This fitting software also calculates confidence intervals at 95% for each parameter of the fitting function and represents the percent chance that the true value falls with in that range. For almost all measurements this value was smaller than the equipment resolution full width at half maximum (ΔE) which ranges from 0.32 eV to 0.57 eV for FEED results, determined by multiplying resolution constant (0.077) and pass energy, and 0.12 eV for UPS measurements.

For fitting the Fowler-Nordheim slope a Linear Regression from Excel 97 was used [10]. Also Excel was used for data presentation.

References.

1. R.D. Young and C.E. Kuyatt, Rev. Sci. Instrum., **39**, 1477 (1968).
2. R.H. Fowler and L. Nordheim, Proc. Roy. Soc. London, **A119**, 683 (1928).
3. W.E. Spicer, Phys. Rev., **112**, 114 (1958).
4. D.A. Dahl and J.E. Delmore, SIMION Version 4.0 EGG-CS-7233 Rev. 2, Idaho National Engineering Laboratory (1988).
5. K. Jost, J. Phys., **E12**, 1006 (1979).
6. C.E. Kuyatt and J.A. Simpson, Rev. Sci. Instrum., **38**, 1 (1967).
7. Hewlett-Packard Co., HP VEE Ver. 3.12 (1995).
8. CRC Handbook of Chemistry and Physics, 77th ed., 12-122 (1997).
9. Peakfit, Jandel Scientific, San Rafeal, CA.
10. Excel 97, Microsoft Corporation 1983-1997.

CHAPTER 4

ULTRAVIOLET PHOTOELECTRON SPECTROSCOPY AND CHARACTERIZATION OF MOLYBDENUM AND IRIDIUM OXIDE

4.1 Introduction

In this chapter, experimental results for work function measurements of molybdenum and iridium flat samples are presented. In addition, the composition, and structure are characterized. The work functions of molybdenum and different states of iridium oxide were determined by UPS. Crystalline structure and composition of molybdenum and iridium oxide were determined by X-ray diffraction (XRD) and X-ray photoelectron spectroscopy (XPS). Additionally, the structural topography of iridium oxide was determined by atomic force microscopy (AFM). In the work, emphasis was on work functions results, while the other characterization techniques were used to confirm sample composition.

The equipment used to measure the work function via UPS for both molybdenum and iridium oxide was the VG ESCALAB MKII detailed in the previous chapter. XPS results were measured on the VG ESCALAB MKII equipment for molybdenum and

iridium oxide. AFM topography measurements of iridium oxide were done on a Digital Instruments Model D5000 atomic force microscope. The XRD measurements of iridium oxide were performed on a Rigaku X-ray diffractometer, and the XRD measurements of molybdenum were done on a Siemens D500 diffractometer.

The molybdenum sample was a 0.01 mm thick 99.95% pure foil sample from a commercial source, Alfa Aesar. The iridium oxide samples were prepared by the Department of Materials and Nuclear Engineering, University of Maryland with a laser ablation technique detailed below. XPS and UPS of the laser ablated iridium oxide samples was done at University of North Texas while AFM and XRD was conducted by Motorola, Flat Panel Display Division [1]. The molybdenum sample was prepared and analyzed exclusively at University of North Texas.

4.2 Preparation and Characterization of Molybdenum with XRD, XPS, and UPS

A polycrystalline sheet of 99.95% pure molybdenum was cut to 1 cm^2 size and characterized with XPS and UPS before and after sputter cleaned with 5 kV argon gun to remove any contamination and oxidation from the surface. The sputter cleaning lasted approximately 20 minutes at 0.75 μA over 0.25 cm^2 area of the sample. Using calculated sputter rates for this particular gun on molybdenum, approximately 35 nm were removed. After XPS and UPS the sample was removed to air and characterized with XRD.

The characterization of the molybdenum sample before and after sputtering by XRD, XPS, and UPS is summarized in Table 4.1 for quick reference.

Molybdenum Results	Before Ar^+ Sputter Clean	After Ar^+ Sputter Clean
XRD	Mo(200) Mo(211) Mo(110) Mo(220)	Mo(200) Mo(211) Mo(110) Mo(220)
XPS	Mo $3d_{5/2}$ 228.2 eV C 1s 286 eV O 1s 531.8 eV Na 1071.8 eV Mo 43%; C 25%; O 30% Na 1% Metallic Mo and surface contamination	Mo $3d_{5/2}$ 228.2 eV O 1s 531.5 eV Na 1072 eV Mo 79%; O 20%; Na 1% Metallic Mo and partial surface oxide
UPS 4.87eV Photon	4.39 eV Photo Threhold (due to surface contamination) 4.62 eV from Mo metal	4.60 eV Photo Threshold
UPS 5.38eV Photon	4.58eV Photo Threshold 4.96 eV and 5.14 eV Higher Bands	4.58eV Photo Threshold 4.80 eV and 5.04 eV Higher Bands

Table 4.1. Summary of characterization results of Molybdenum samples before and after sputter cleaning.

4.2.1 Composition of Molybdenum Sample using X-ray Diffraction and XPS

XRD of the molybdenum sample was done at atmosphere on a Siemens D500 diffractometer and is plotted in Figure 4.1. The XRD was taken in a location that was sputtered and non-sputtered, both spectra had very similar structure with no shifting in peak location and less background noise in the sputtered case. The XRD spectra correspond to metallic molybdenum with the 110, 200, 211, and 220 planes composing the spectra. These are all of the standard planes seen in polycrystalline molybdenum between the 2Θ angles of 30° and 90° [2]. Metallic molybdenum forms a body centered cubic with a lattice parameter a = 3.15 Å.

XPS of the molybdenum sheet before and after sputtering using Aluminum Kα radiation on a VG ESCALAB Mark II are shown in figure 4.2. XPS results were fitted with Peakfit to determine position and area, then the area and Atomic Sensitivity Factors for each element were used to determine composition [3, 4]. The elemental composition before sputter was; 43% Mo, 25% C, 30% O, and 1% Na, and after sputter clean was; 79% Mo, 20% O, and 1% Na. Table 4.1 shows no appreciable elemental peak shift was evident between sputtered and non-sputtered results. The molybdenum $3d_{5/2}$ peak had a XPS value of 228.2 eV. This demonstrates that the sample was predominantly metallic molybdenum with C and O surface contamination before and some O surface contamination after sputtering [5]. Molybdenum readily oxidizes under vacuum (1×10^{-3} Torr), so it is very difficult to totally remove the surface oxide, however high temperature anneals will vaporize the oxide at over 1200°C.

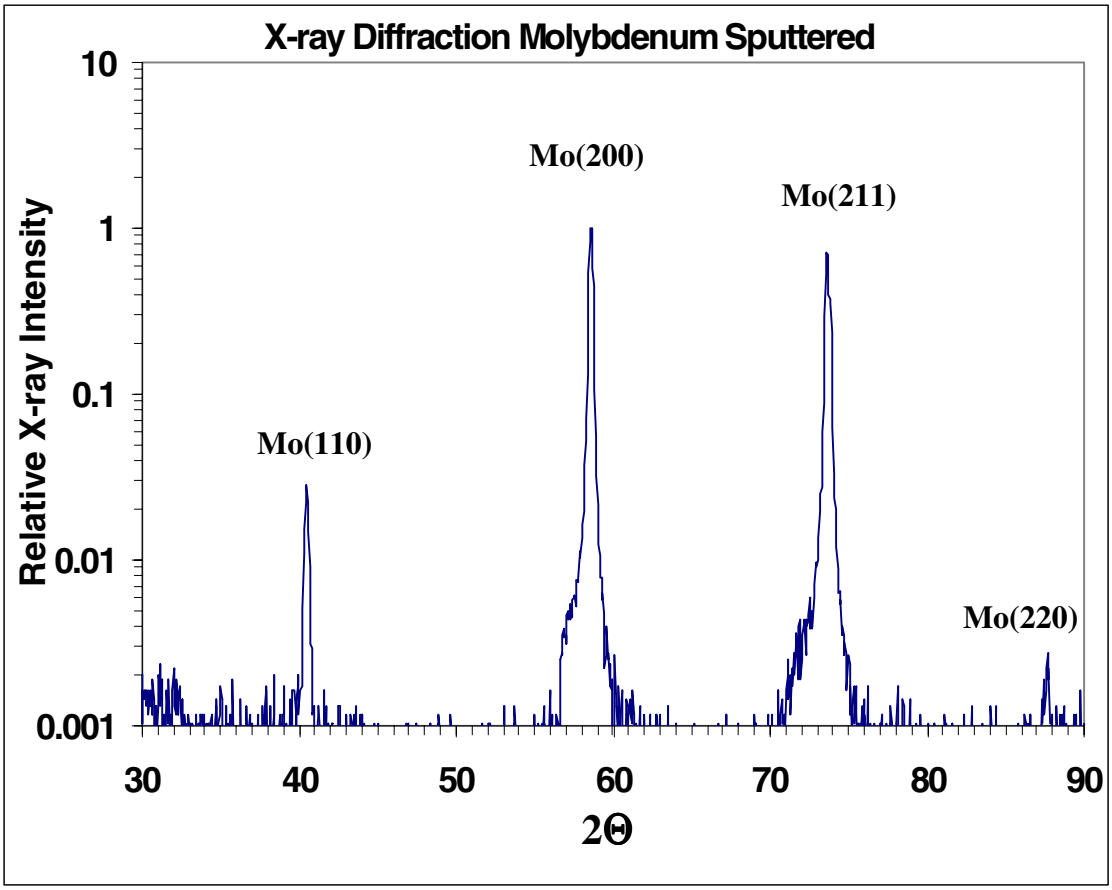

Figure 4.1. XRD spectra of Molybdenum after sputter clean. Sample illuminated with Cu Kα1 X-rays, with pertinent crystal structures labeled.

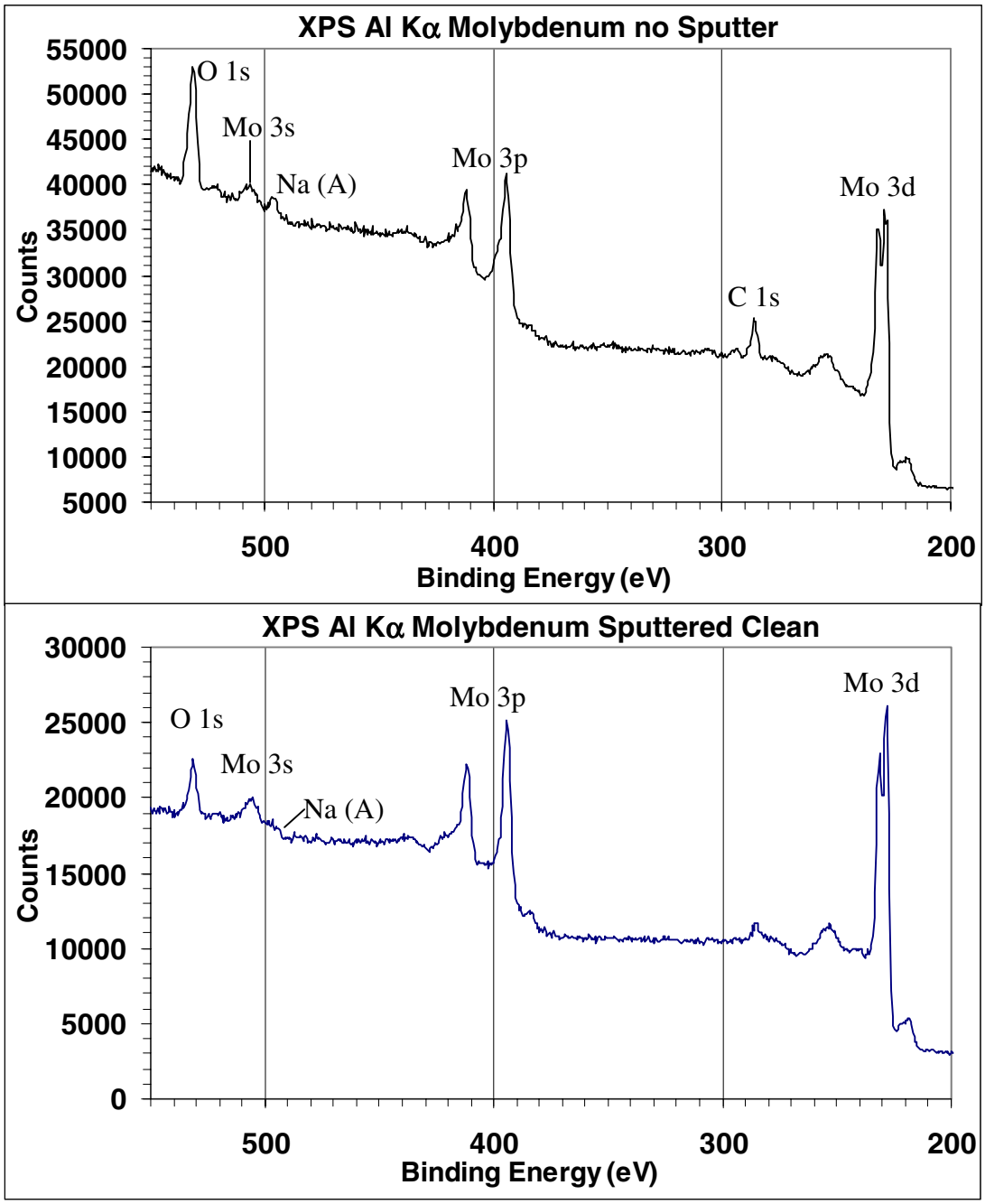

Figure 4.2. UPS spectra of Molybdenum before sputter clean (top) and after sputter clean (bottom). Both samples excited with Al Kα X-rays.

4.2.2 Work Functions of Molybdenum using UPS

The work function measurements were made with a VG ESCALAB II system using a Mercury/Xenon ultraviolet photon source and monochromator. The monochromator with a 2 nm wavelength resolution and UV source gave an energy resolution of 38 meV at a wavelength 254 nm. Work function measurements were made at photon energies of 4.87 eV (254 nm) and 5.38 eV (230 nm). Measurements were made before and after a 5 keV argon sputter gun removed approximately a 35 nm film to remove residual carbon and oxygen on the sample surface. The sample surfaces were irradiated with ultraviolet light at each frequency while the resulting photoelectron energy distribution was measured as a function of binding energy (the incident photon energy minus the electron kinetic energy). The overall energy resolution determined by the monochromator and hemispherical energy analyzer was approximately 0.12 eV for this data.

The UPS data were used to determine whether the photoelectrons were due to direct (no phonons involved) or indirect (phonons involved) optical transitions and then to determine the photoelectric thresholds [6, 7]. For a direct process, the peak in the photoelectron kinetic energy distribution moves to higher energy at approximately the same rate as the incident photon energy is increased, provided that the initial (pre-excited) energy band is relatively flat. In such a case, the position of a peak in the photoelectron energy distribution remains fixed when plotted verses binding energy with a well defined Gaussian shape because only particular initial and final electron states are

involved in the photoelectron process. The work function (Φ) is given by the position of the lowest energy Gaussian on plots of photoelectron counts verses binding energy. For an indirect process, a peak in the photoelectron energy distribution usually remains fixed as photon energy is increased. This distribution expands as the photon energy increases and higher binding energies are excited from a distribution of lower energy initial states. This leads to a non-Gaussian distribution, a distribution that reflects the numerous electron density of states in the energy range to be excited. Moreover, direct transition are generally dominant due to the fact that they are a two-body process involving a, photon and electron, verses a three-body indirect process where a, photon, electron, and phonon are involved [8].

UPS results for 4.87eV photons on non-sputtered and sputtered molybdenum are shown in Figure 4.3.A, and 5.38 eV photon results on non-sputtered and sputtered molybdenum are shown in Figure 4.3.B. All data sets were fitted with 3 Gaussians or less with a constant background using Peakfit [3]. The fits were very good for all conditions indicating that direct transitions or transitions with well-defined initial states were the predominant source of photoemission.

For 4.87 eV photon UPS spectra the peak that remains after sputtering is 4.60 eV with a very good fit (95% confidence interval of $\pm$ 0.001 eV). Before sputtering there are two peaks at 4.4 eV and 4.6 eV, with a 95% confidence interval of $\pm$ 0.01 eV for the 4.6 eV peak. The lower energy peak in the pre-sputtered case is attributed to surface contamination of carbon and oxygen and the value of 4.6 eV is from molybdenum and

corresponds to the work function. Both observations: (1) lowering of work function from surface contamination; and (2) a work function value of 4.6 eV for molybdenum are in agreement with previous observation [9].

For 5.38 eV photon UPS spectra the lowest energy peak for both pre and post sputter clean is located at 4.58 eV photon energy in close agreement with the work function value of 4.6 eV. The shift falls within equipment resolution of 0.12 eV, however this shift can also be attributed to a small shift in the initial state's energy level indicating a direct transition between an initial state with a small bend in the energy level and a particular final state. The higher energy states in the spectra are very effected by sputtering indicating emission from surface resonance states below the Fermi level by 0.5 eV of less. These surface resonance states are very sensitive to surface contamination, and theoretical modeling predicts such states for body centered cubit transition metals from spin-orbit coupling below the Fermi level along the ΓH direction in some transition metals. Previous research has found these surface resonance states on tungsten and the (100) plane of molybdenum [10]. This agrees with the molybdenum XRD results that show the (200) crystal plane which reduces to (100) is the major plane.

The good fit with Gaussian distributions and the relative stability of the lowest energy peak in binding energy when illuminated with different photon energies show the transition to be a direct transition with well localized initial and final states and corresponding energy levels. This direct transition has threshold energy of 4.6 eV, in agreement with previous results [9].

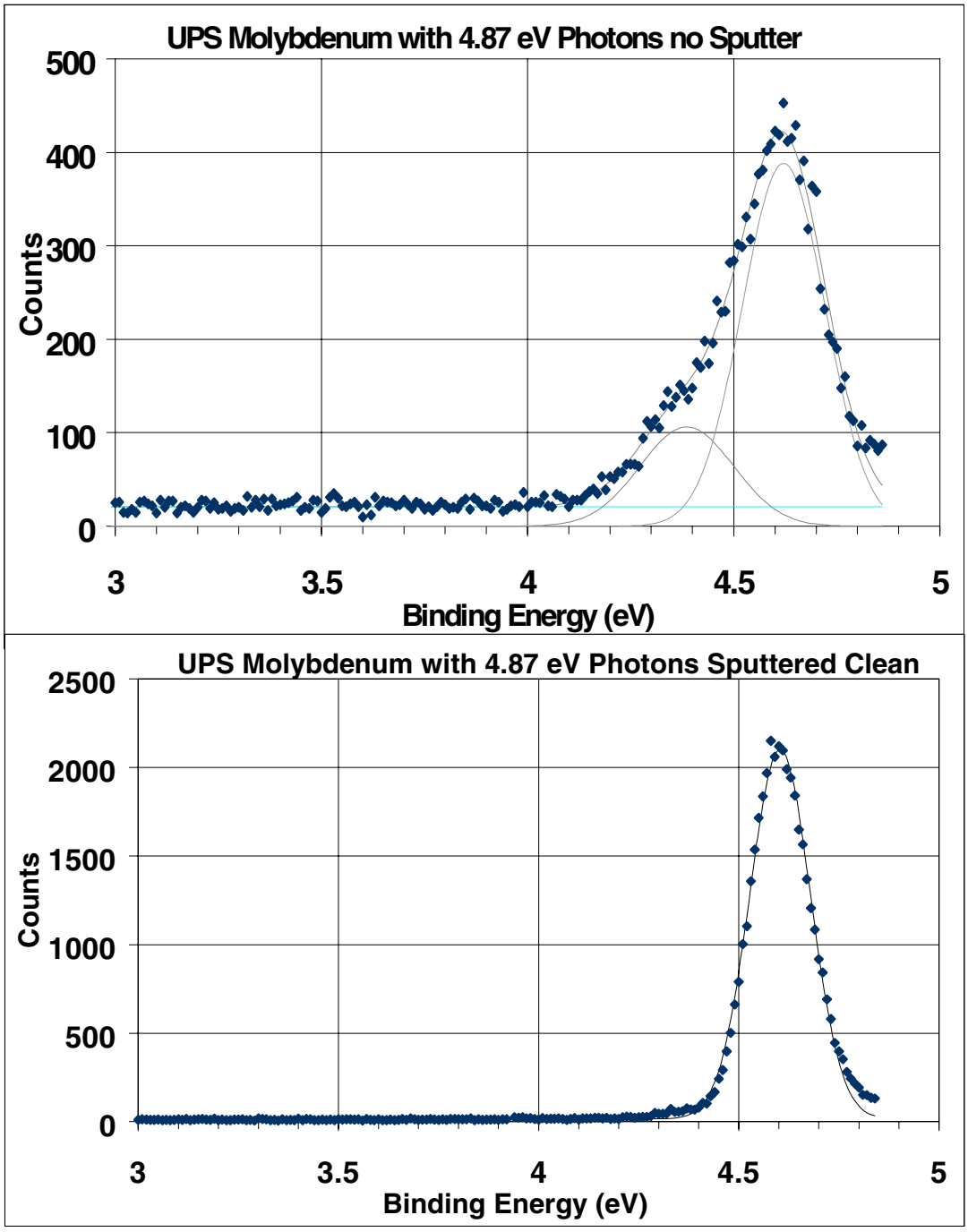

Figure 4.3.A. UPS spectra of Molybdenum before sputter clean (top) and after sputter clean (bottom). Both samples excited with 4.87 eV photons.

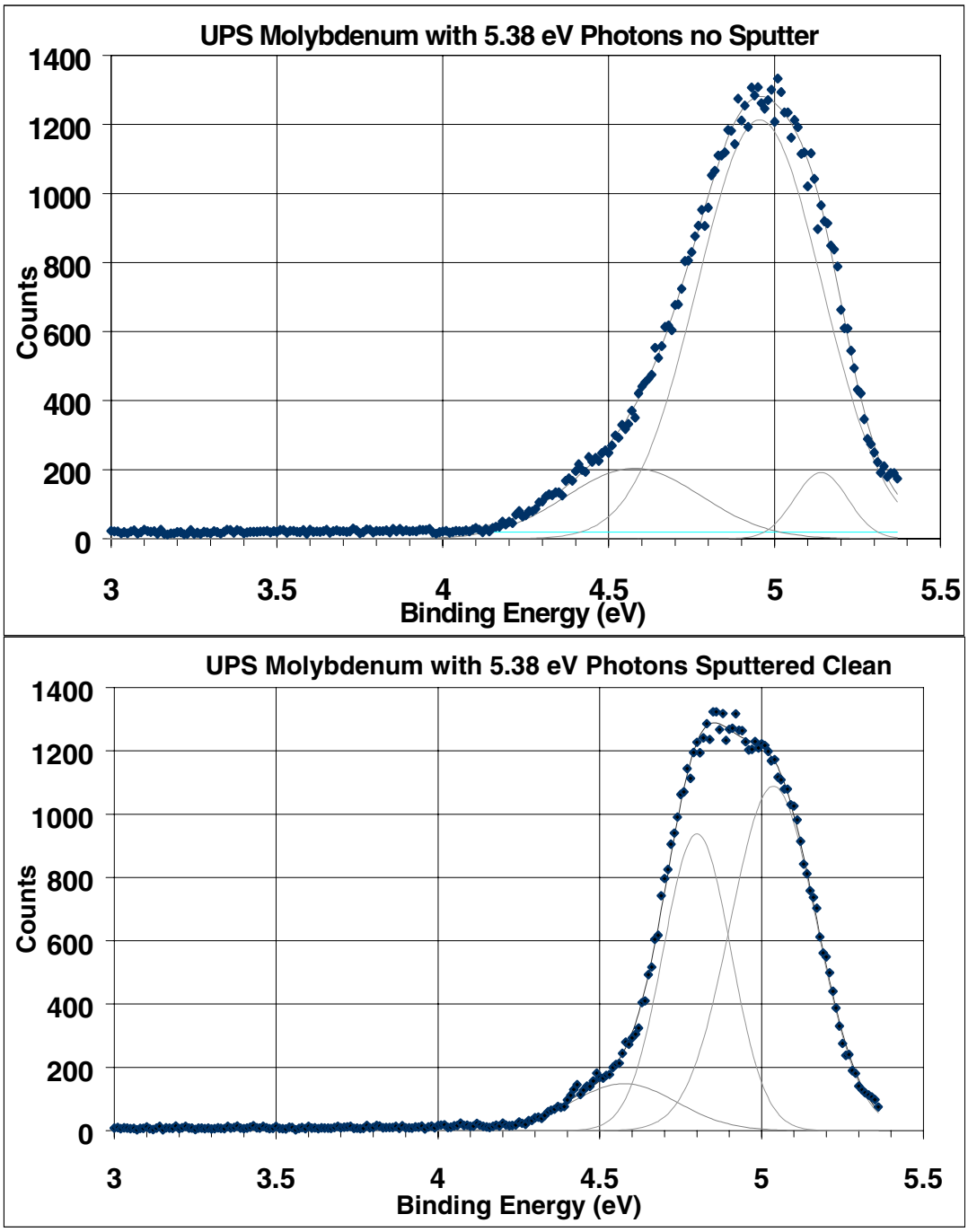

Figure 4.3.B. UPS spectra of Molybdenum before sputter clean (top) and after sputter clean (bottom). Both samples excited with 5.38 eV photons.

4.3 Iridium Oxide Samples

The highly conductive oxide of iridium was prepared by annealing over a broad temperature range to examine the process robustness for semiconductor and flat panel display applications. Iridium oxide is an effective conductor in corrosive and oxidizing environments and exceptionally resistant for cathodes in electrolytic reactions [11]. The conductivity, diffusion barrier properties, and ability of iridium oxide to adhere to other high dielectric oxides make it an applicable material in electronics devices as components of switching layers and ferroelectric memories [12,13]. Moreover, the work function of iridium oxide has been examined first by this research in correlation with the above characterization methods over a rage of thermal growths described below.

If iridium oxide possesses a low work function along with its other characteristics, another application could be in protective coatings on field emission arrays for future use in flat panel displays. In these applications, long-term stability requires the emission tips to be very stable in harsh conditions where oxidation can degrade performance [14]. In addition, the power required to operate these displays is exponentially dependent on the work function of the tips as defined by the Fowler-Nordheim equation [15]. Therefore, a low work function and strong resistance to harsh oxidizing conditions are needed for long term field emission application.

The characterization of the iridium oxide samples annealed at different temperatures in oxygen ambient by XRD, XPS, AFM, and UPS is summarized in Table 4.2 for quick reference.

Iridium Oxide Results	**NO O_2 Anneal**	**600°C O_2 Anneal**	**700°C O_2 Anneal**	**800°C O_2 Anneal**	**900°C O_2 Anneal**
XRD	No data.	Ir(111) IrO_2(110)	Ir(111) IrO_2(110)	Ir(111) IrO_2(110) IrO_2(101) IrO_2(200)	No Ir or IrO_2 only LAO substrate.
XPS	Ir 60.75 eV O 531.0 eV metallic Ir	Ir 62.0 eV O 530.0 eV IrO_2	Ir 62.0 eV O 530.0 eV IrO_2	Ir 62.0 eV O 530.0 eV IrO_2	Ir none O 529.4 eV $LaAlO_3$ sub.
AFM	rms 0.187nm range 2.06nm	rms 1.67nm range 13.1nm	rms 3.36nm range 34.1nm	rms 21.6nm range 201nm	rms 0.515nm range 8.42nm
UPS 4.87eV Photon	No data.	4.26 eV Photo Threshold	4.29 eV Photo Threshold	4.14 eV Photo Threshold	4.25 eV Photo Threshold
UPS 5.38eV Photon	No data.	4.23eV Photo Threshold 4.53 eV Higher Band	No data.	No data.	No data.

Table 4.2. Summary of characterization results of Iridium Oxide samples annealed at different temperatures.

4.3.1 Preparation of Iridium Oxide Samples

Pulsed laser ablation (PLD) was used to deposit thin films of iridium on 1mm thick single crystal substrates of $LaAlO_3$. A 248 nm KrF pulsed excimer laser was used to ablate a solid stoichiometric Iridium metal target on to the $LaAlO_3$ substrates by the Department of Materials and Nuclear Engineering, University of Maryland [16]. During iridium deposition, the base pressure of the deposition system was kept at 10^{-5} Torr. The excimer laser was operated in the pulse mode with pulses of 20 nsec and peak power densities reaching 2 J/cm^2 on the target. The grown iridium films have a thickness of approximately 1500Å and show (111) orientation. The samples were then annealed in a furnace with a continuous flow of O_2 at anneal temperatures of 600°C, 700°C, 800°C, and 900°C for one hour.

4.3.2 Composition of Iridium Oxide Samples using X-ray Diffraction and XPS

XRD results are plotted in Figure 4.4.A and 4.4.B showing continuous oxidation of Ir with increasing temperatures, the ratio of Ir(111) to IrO_2(110) is shown on the plots. An anneal temperature of 900°C resulted in almost a total loss of the iridium from the substrate due to the sublimation of the metal in the form of IrO_X at high temperatures. This sublimation confers with previous research demonstrating IrO_2 decomposes to the volatile oxide of IrO_3 above 800°C in oxygen ambient [17]. Further research revealed that indeed IrO_3 is the predominant volatile oxide with minimal amounts of volatile IrO_2 and possibly IrO [18,19].

The XRD spectra correspond to the crystal structure of IrO_2, which is rutile with a

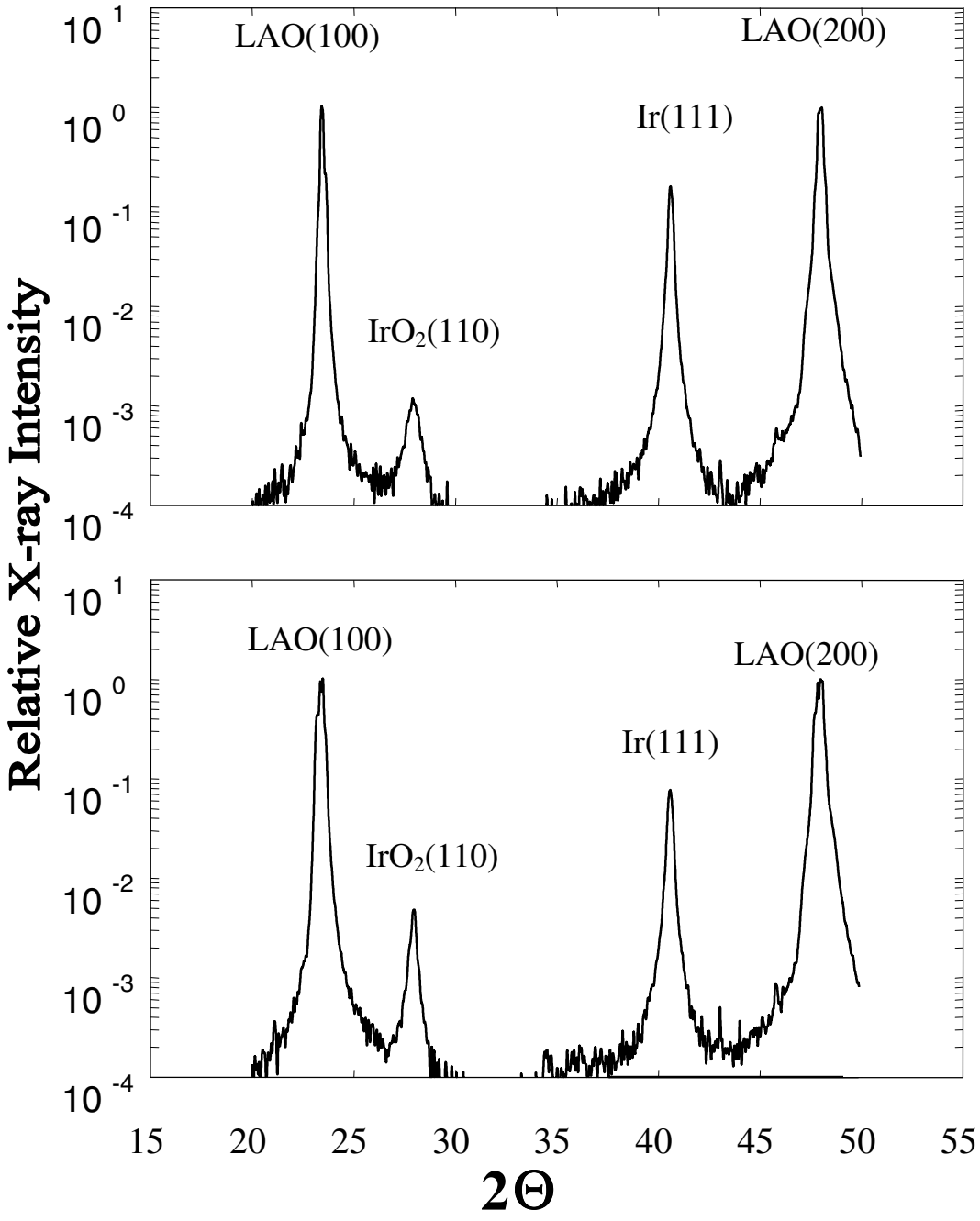

Figure 4.4.A. The X-ray diffraction for 600°C anneal iridium oxide sample is the top plot with pertinent crystal structures labeled, and the 700°C anneal sample is presented below.

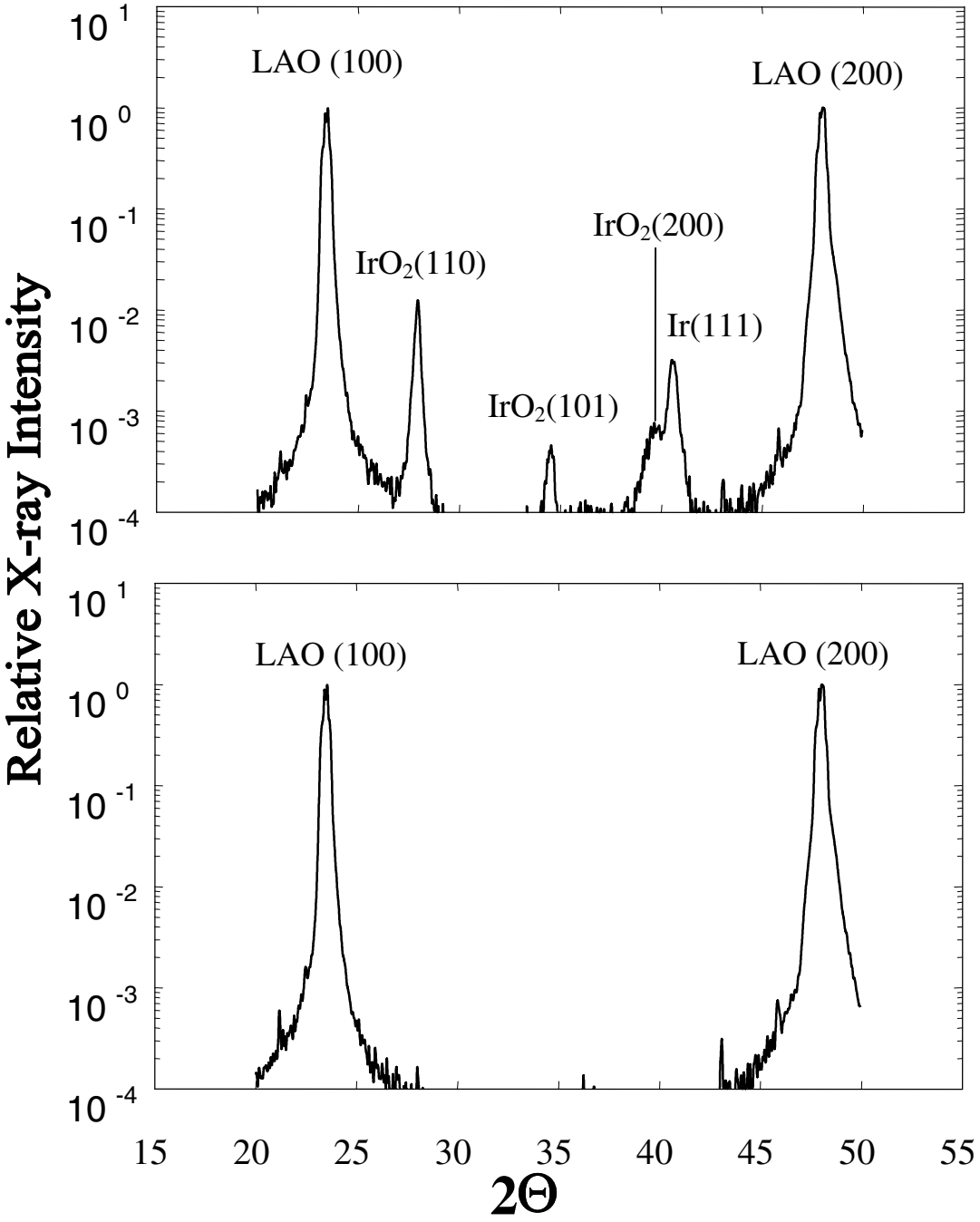

Figure 4.4.B. The X-ray diffraction for 800°C anneal iridium oxide sample is the top plot with pertinent crystal structures labeled, and the 900°C anneal sample is presented below.

structure depicted in Figure 4.5 [20,21]. Accordingly, the (100) planes have only Ir ions whereas the (200) planes have one Ir and two oxygen ions, a complete IrO_2 molecule. The rutile primitive tetragonal lattice parameters are a=4.51Å, b=4.51Å, and c=3.15Å. We also observe in the 800°C sample the (200) and (101) peak of IrO_2 is present unlike the 600°C and 700°C samples.

X-ray photoelectron spectroscopy was used to determine the surface chemical composition and oxidation states. Oxygen content increases with increasing anneal temperature. For annealing temperature of 600°C to 800°C, the average O to Ir ratio is (2.47 +/- 0.05), which agrees with previous XPS characterization [22]. Consistent with the XRD data, annealing at 900°C in O_2 for one-hour results in the complete loss of Ir from the film evidenced by the XPS detection of the substrate elements Al and La on these samples.

XPS results collected from the samples annealed at different temperatures are overlaid in Figure 4.6 for iridium (top plot) and oxygen (bottom plot). The metallic Ir $4f_{7/2}$ peak is at 60.75 eV, the $4f_{7/2}$ peak of Ir in the IrO_2 form is at 62.0 eV. From these XPS spectra, it is evident that the as deposited film is metallic Ir. After they are annealed in O_2, the surfaces of the films become IrO_2 [22]. The shapes of the XPS spectra from the surfaces annealed at 600°C, 700°C, and 800°C are very similar. A shift in the O 1s peak of the binding energy curve was also observed as a function of annealing temperature and this is clearly shown in Figure 4.6 lower plot. A small amount of oxygen was found on the as grown Ir film, with a binding energy of 531.0 eV.

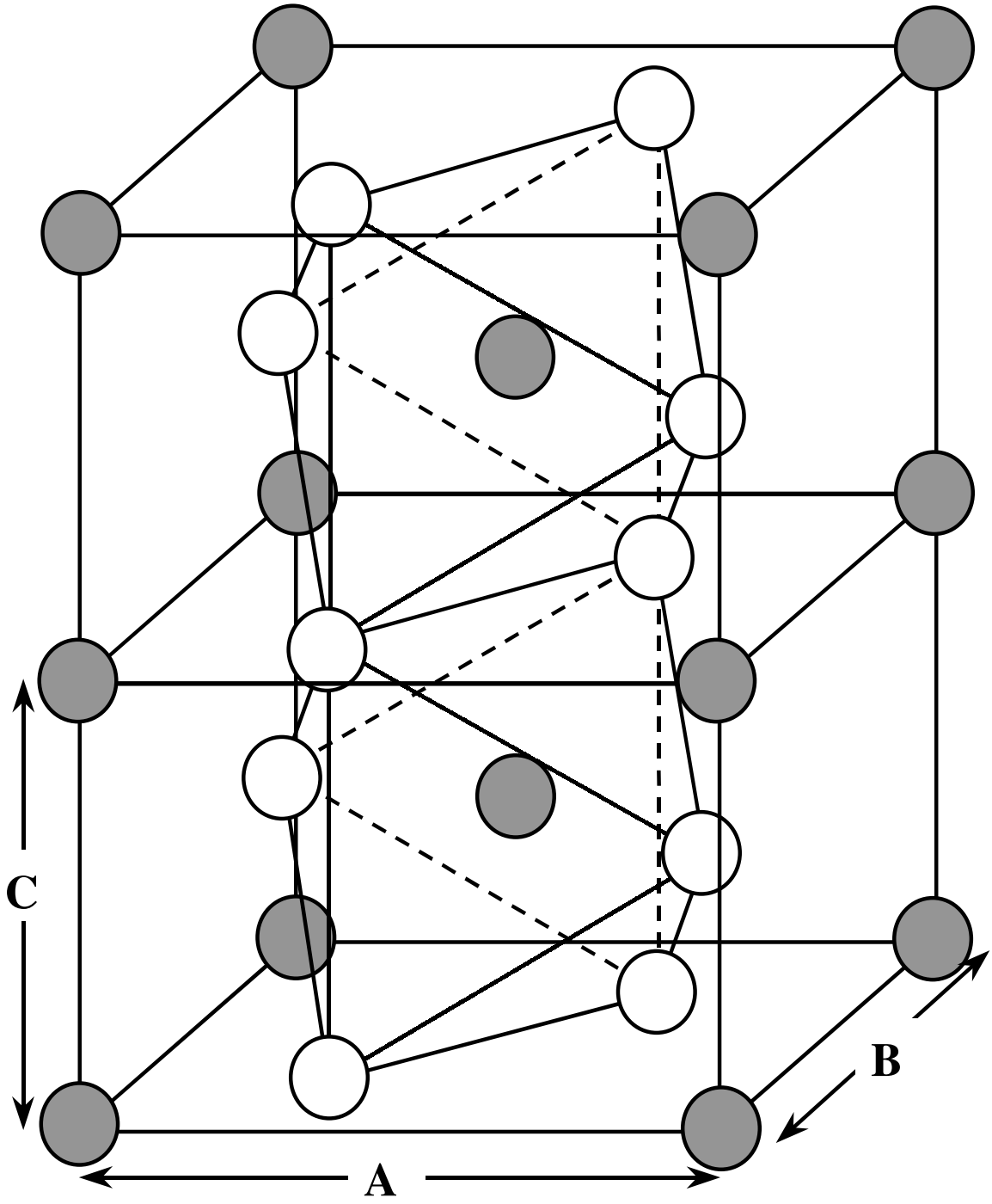

Figure 4.5. The rutile crystal structure of IrO_2 with lattice parameters A, B, and C labeled. The iridium metal atoms are gray and oxygen atoms are white.

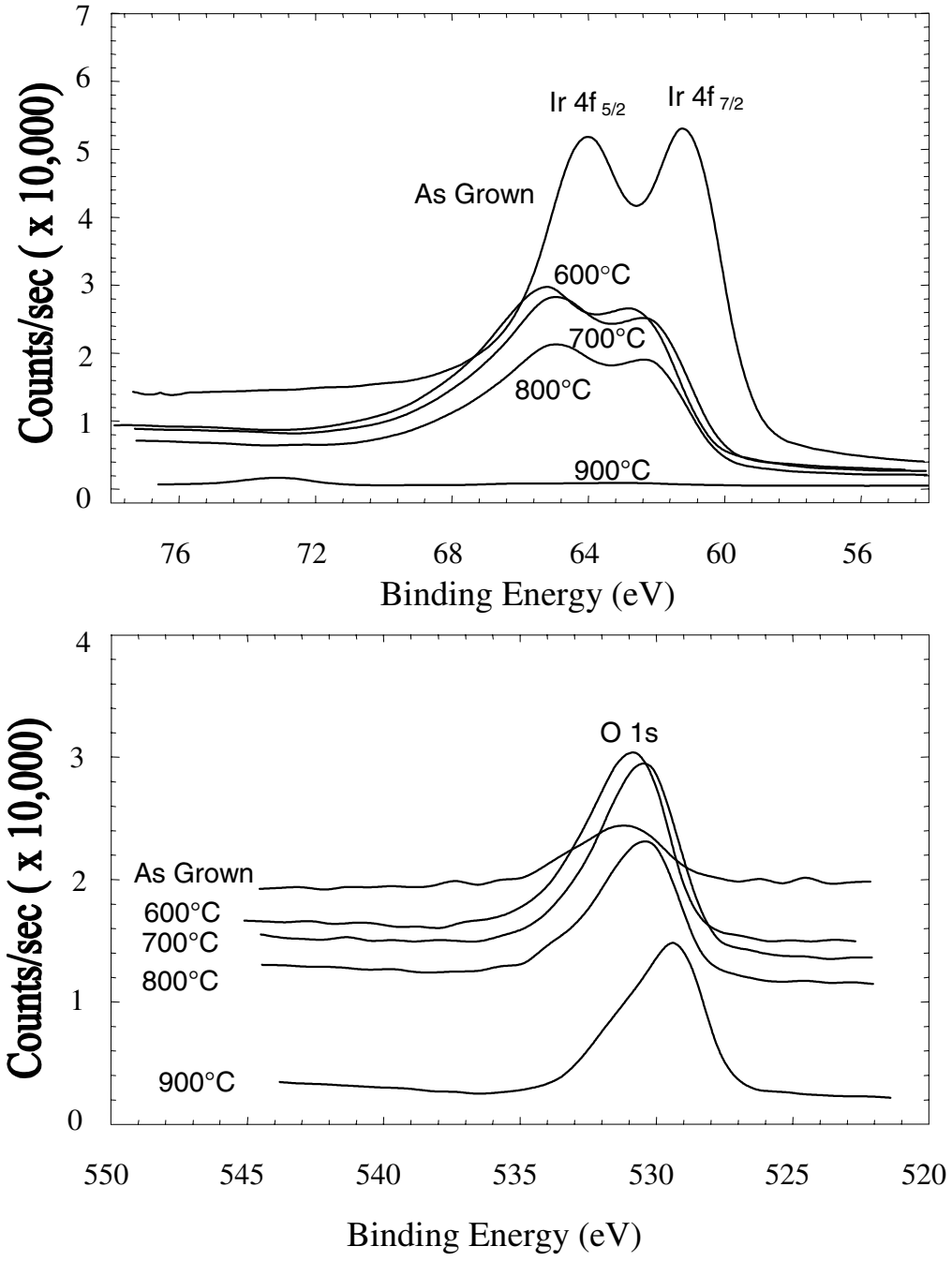

Figure 4.6. The XPS spectra for iridium displayed in top plot and oxygen displayed in bottom plot, for iridium oxide samples prepared at different anneal temperatures.

With increasing annealing temperature, the binding energy reduces to 530.0 eV, consistent with the formation of iridium oxide [22]. For annealing at 900°C, the binding energy of oxygen is 529.4 eV, which is the binding energy of oxygen in $LaAlO_3$. Preliminary results of temperature programmed desorption studies on thermally grown iridium oxides show increased stability with higher anneal temperatures up to 800°C [1].

4.3.3 Surface Morphology of Iridium Oxide Samples using AFM

Changes in the surface roughness as a function of growth temperature were determined using atomic force microscopy (AFM) measurements. The AFM surface morphology results are shown in Figure 4.7.A and 4.7.B. The deposited Ir film with no anneal is very smooth, with a root-mean-square (rms) roughness of 1.87 Å and a surface height range (low point to high point) of 20.6 Å. The grain size and thus the surface roughness increases with increasing anneal temperature. From the as deposited film to 700°C annealed film (Figure 4.7.B) the surface rms roughness and height range grow almost linearly, rms from 1.87 Å to 33.6 Å, height range from 20.6 Å to 340.6 Å. However, the film annealed at 800°C in O_2 (Figure 4.7.B) exhibits large jumps in the rms roughness (216 Å) and surface height range (2014 Å) which are clearly shown by the AFM images in the figure. The structural changes with increasing annealing temperatures are a result of the growth of IrO_2 crystalline structures. At 900°C anneal the surface losses almost all of its topography and returns to values close to the no annealed sample with rms of 5.15 Å and range of 20.6 Å indicating a loss of IrO_2 crystal structure between the 800°C and 900°C anneal.

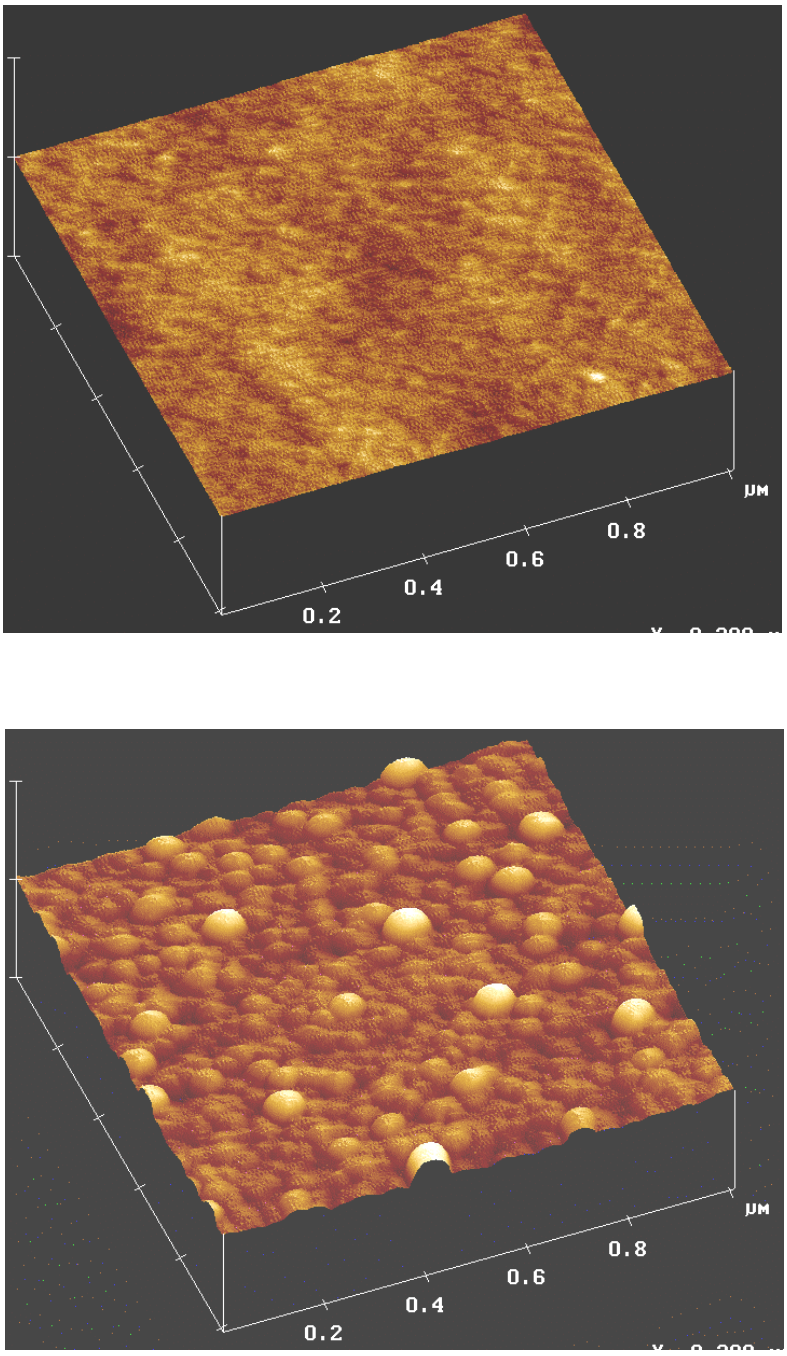

Figure 4.7.A. AFM surface scan of iridium oxide with no anneal displayed in top picture, and annealed at 600°C displayed in bottom picture.

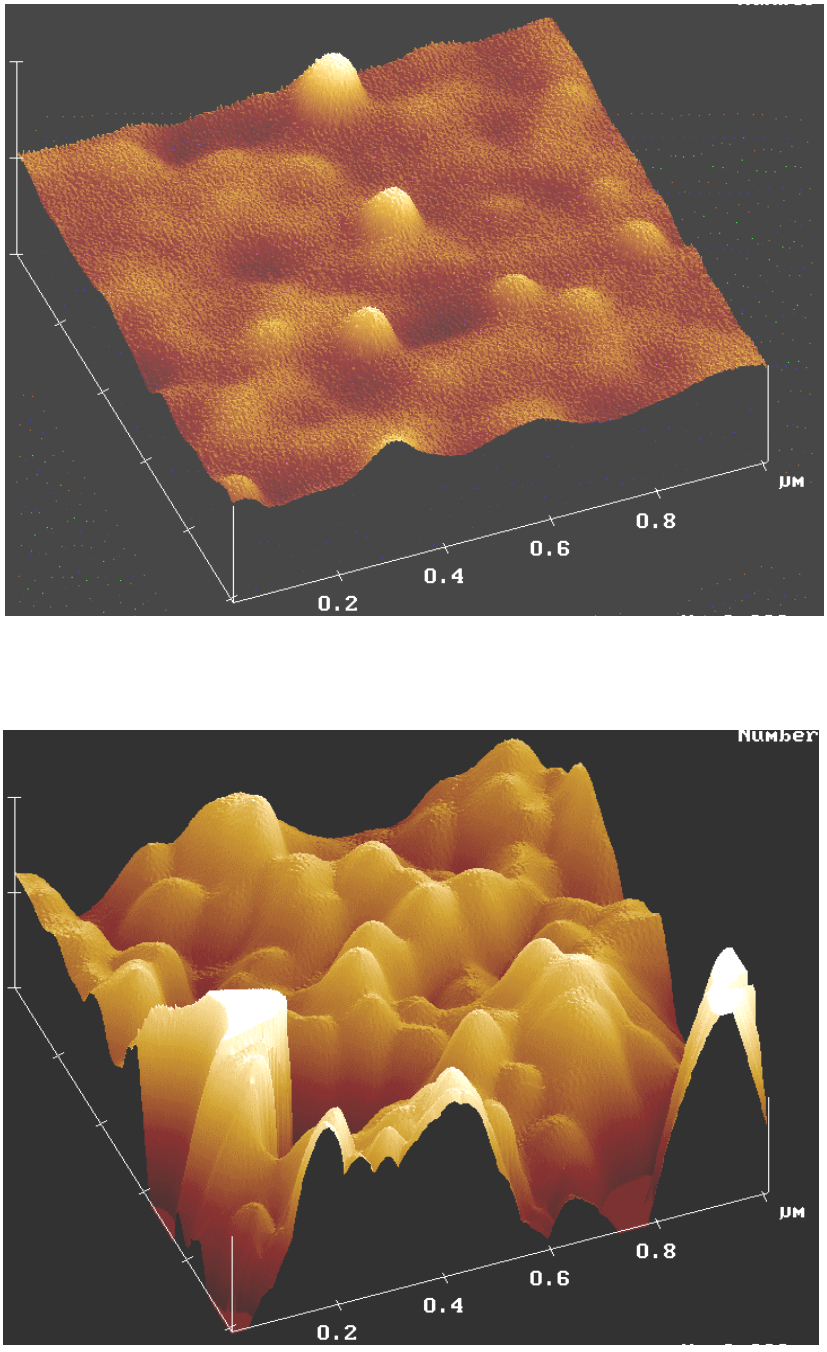

Figure 4.7.B. AFM surface scan of iridium oxide annealed at 700°C displayed in top picture, and annealed at 800°C displayed in bottom picture.

4.3.4 Work Functions of Iridium Oxide Samples using UPS

The work function measurements were made with the same VG ESCALAB II system that characterized the molybdenum samples under similar conditions; photon energies of 4.87 eV (254 nm) and 5.38 eV (230 nm) were used, energies are in binding energy (the incident photon energy minus the electron kinetic energy) and overall energy resolution determined by the monochromator and hemispherical energy analyzer was approximately 0.12 eV. However, UPS was conducted only after a 5 keV argon sputter gun was used to remove approximately 10 to 20 nm of each film to remove residual carbon on the sample surface.

The UPS results for films annealed at 600°C, 700°C, 800°C, and 900°C respectively are shown in Figure 4.8.A, 4.8.B, and 4.8.C. All data sets from 4.87 eV photon illumination were fitted with one Gaussians and a constant background using Peakfit computer program [3]. The fits were quite good for the films annealed at 600°C, 700°C, and 800°C with no indication of a lower energy peak for the photon energy of 4.87 eV. In all cases, the peaks are at approximately the same energy position. In addition, while the distributions observed at annealing temperatures of 600°C and 700°C have a FWHM of about 0.38 eV, the 800°C film has a width of only 0.19 eV at a lower binding energy. The 800°C film also showed more IrO_2 crystal planes were exposed from XRD data, and that the crystal size was larger in the AFM data.

UPS measurements were also made on samples annealed at 600°C using 5.38 eV photons. Higher energy photons were used to see if the position of the threshold observed

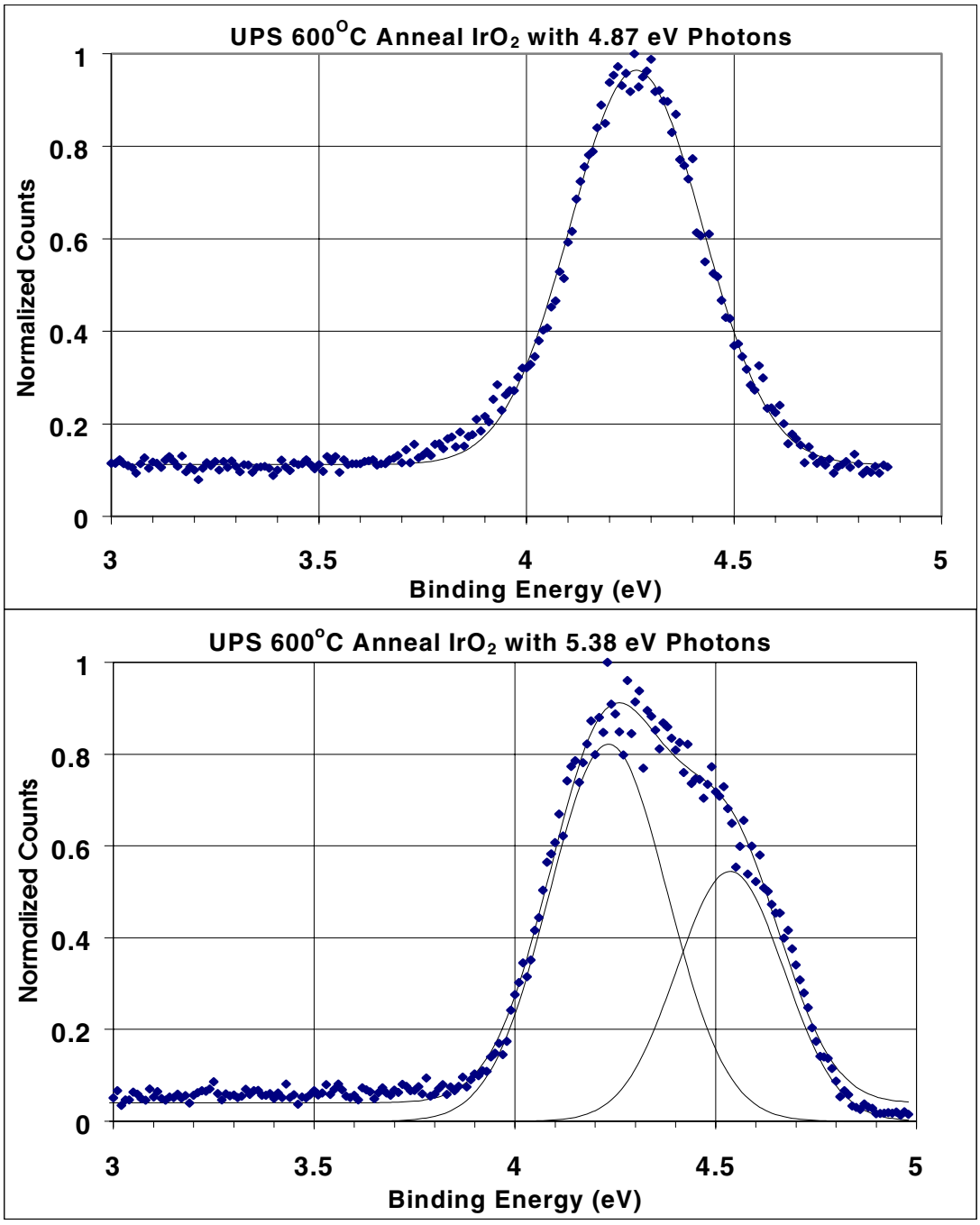

Figure 4.8.A. UPS work function measurement of 600°C anneal sample fitted with Gaussians, 4.87 eV incident photons top graph, and 5.38 eV photons bottom graph.

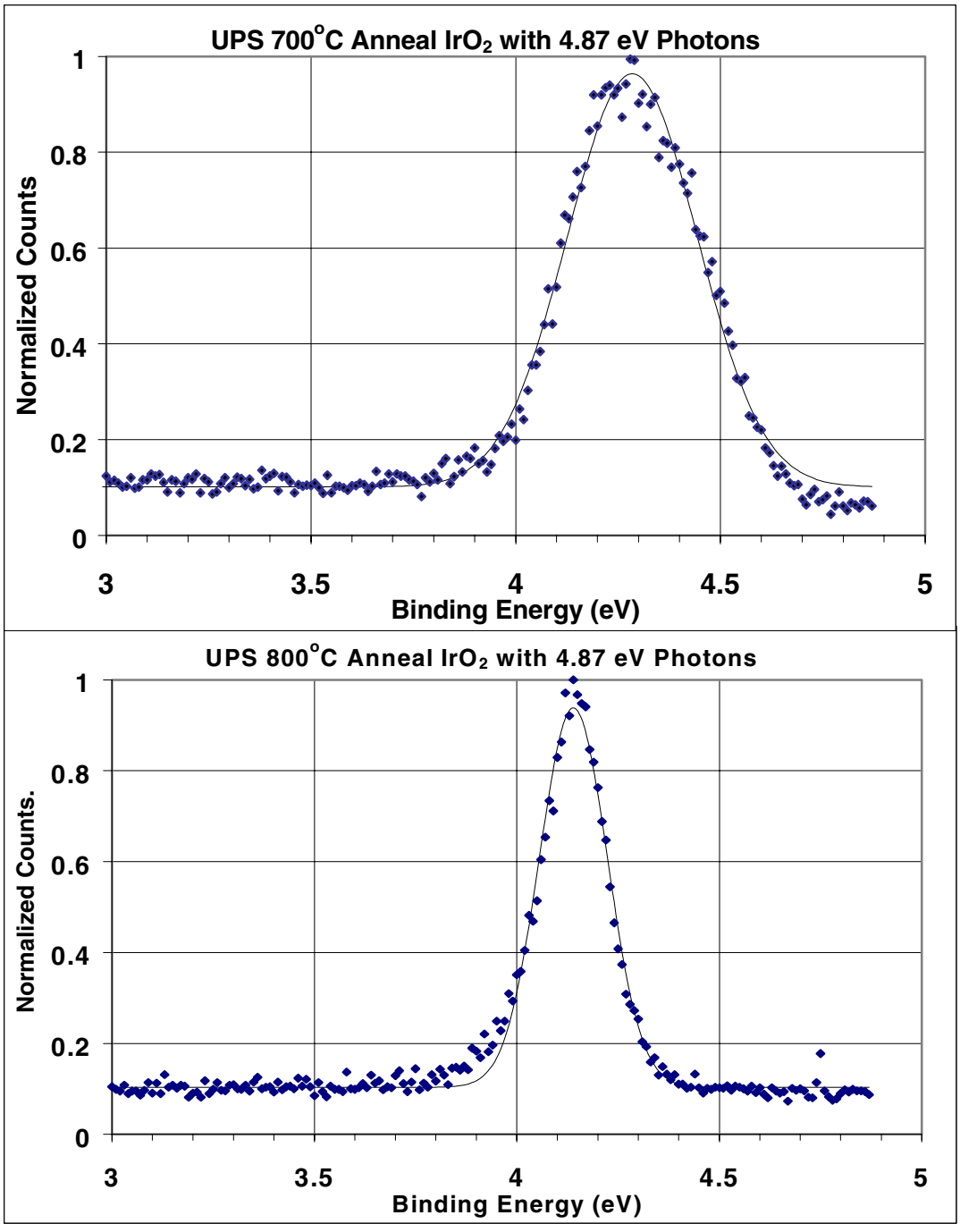

Figure 4.8.B. UPS work function measurement of 700°C anneal sample (top) and 800°C anneal sample (bottom). The photon energy is 4.87 eV, and both plots are fitted with a Gaussian.

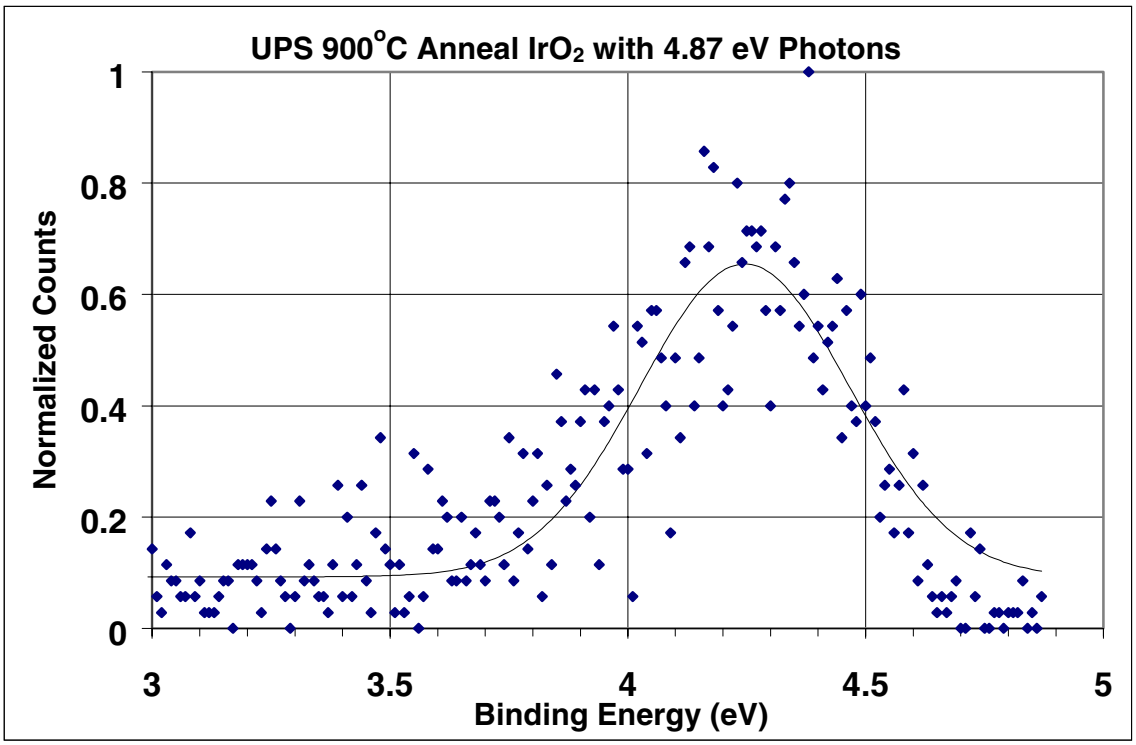

Figure 4.8.C. UPS work function measurement of 900°C anneal sample. The photon energy is 4.87 eV, and plot is fitted with a Gaussian.

with 4.87 eV photons moved in binding energy when higher energy photons were used. In this case, two Gaussians and a constant background are needed to fit the data. The position of the lowest energy peak is in agreement with the data for 4.87 eV photons and the higher energy peak is believed to be due to the direct excitation of a higher energy band.

To determine direct or indirect transitions for iridium oxide the same criteria stated in the molybdenum analysis are used. Therefore, the good fit with Gaussian distributions and the stability of the lowest energy peak in binding energy when illuminated with different photon energies show the transition to be a direct transition. The threshold energy is 4.23 eV ± 0.06 eV, average and standard deviation from all data. Note that the standard deviation found in the data set and equipment resolution agrees.

4.4 Conclusions

XRD, XPS, and UPS were used to characterize flat molybdenum samples before and after sputter cleaning. The spectra from XRD and XPS correspond to metallic molybdenum and are in agreement with previous work. Additionally the work function measurement of 4.6 eV is also in agreement with previous research validating our characterization techniques.

XRD, XPS, AFM, and UPS were used to study flat iridium films annealed at different temperatures in O_2 ambient. Continuous growth of IrO_2 (110) was observed with increasing temperature up to 800°C. XPS measurements show that the as grown Ir films are metallic. After they are annealed at higher temperatures up to 800°C in O_2

ambience, they oxidize to form IrO_2; annealing at 900°C for 1 hour leads to almost complete desorption of Ir film. AFM measurements show that the films become rougher and grain sizes become larger as the annealing temperature increases. This is a result of the growth of IrO_2 crystalline structure. Work function measurements by UPS show that when annealing temperature increases from 600°C to 800°C the UPS spectrum FWHM narrows from 0.38 eV to 0.19 eV. After the Ir film is converted to IrO_2 its work function is 4.23 eV. This data provides the conditions required for creating relatively smooth iridium oxide films for electrode materials, and suggests that IrO_2 will have important applications in vacuum microelectronics where electrical stability in the presence of oxygen is critical. In particular, the characteristics of iridium oxide are desirable for field emission applications and will be detailed in the next chapter.

References.

1. B. Chalamala, J. Bernhard, D. Golden, B. Gnade, E. Sosa, S. Aggarwal, Appl. Phys. Lett. **74**, 1394 (1999).
2. W. Schreiner, *XRD Pattern Processing for the PC*, Materials Data, Inc., Livermore CA.
3. Peakfit, SPSS, Inc., 444 North Michigan Avenue, Chicago, IL 60611.
4. C.D. Wagner, W.M. Riggs, L.E. Davis, J.F. Moulder, and G.E. Muilenberg, *Handbook of X-ray Photoelectron Spectroscopy*, Perkin-Elmer Corp., Eden Prairie MN, 188 (1979).
5. K.S. Kim, W.E. Baitinger, J.W. Amy, and N. Winograd, J. of Electron Spectroscopy and Related Phenomena, **5**, 351 (1974).
6. C. N. Berglund and W.E. Spicer, Phys. Rev., **A136**, 1044 (1964).
7. E.O. Kane, Phys. Rev, **127**, 131 (1962).
8. N. V. Smith, Phys. Rev., **B3**, 1762 (1971).
9. D.E. Eastman, Phys. Rev, **B2**, 1 (1970).
10. R.C. Cinti, E. Al Khoury, and B.K. Chakraverty, Phys. Rev, **B14**, 3296 (1970).
11. T. Nakamura, Y. Nakao, A. Kamisawa, and H. Takasu, Appl. Phys. Lett., **65**, 1522, (1994).
12. K. Kreider, Sensors and Actuators, **B5**, 165, (1991).
13. W. C. Dautremont-Smith, Displays, **3**, 67, (1982).

14. B.R. Chalamala, R.M. Wallace and B.E. Gnade, J. Vac. Sci. Technol., **B16**, 2859 (1998).

15. R. H. Fowler and L. Nordheim, Proc. Roy. Soc. London, **A119**, 683 (1928).

16. S. Madhukar, S. Aggarwal, A.M. Dhote, R. Krishnan, D. Keeble and E. Poindexter, J. Appl. Phys., **81**, 3543, (1997).

17. E. H. P. Cordfunke and G. Meyer, Recueil, **81**, 495 (1962).

18. J. H. Norman, H. G. Staley, and W. E. Bell, J. Chem. Phys., **42**, 1123 (1965).

19. V. S. Smentkowski and J. T. Yates, J. Vac. Sci. Technol, **A12,** 219 (1994).

20. D. B. Rogers, R. Shannon, A. Sleight, and J. Gillson, Inorganic Chem., **8**, 841 (1969).

21. M. A. El Khakani, M. Chaker, and E. Gat, Appl. Phys. Lett., **69**, 2027 (1996).

22. M. Peuckert, Surface Sci., **144**, 451 (1984).

CHAPTER 5

FIELD EMISSION ENERGY DISTRIBUTIONS AND FOWLER-NORDHEIM PLOTS OF MOLYBDENUM AND IRIDIUM OXIDE

5.1 Introduction

In this chapter, experimental results for etched emission tips of molybdenum and molybdenum coated with iridium oxide are presented to evaluate work functions and stability of tips under field emission conditions. The simultaneous measurement of FEED and Fowler-Nordheim I-V curves allows determination of; (1) the work function of a material from the inflection point of the FEED distribution for a conductive material, and (2) the tip geometric parameter from the slope of the Fowler-Nordheim I-V curve, which is dependent on tip geometry (b) and work function (Φ) were the slope = $-b\Phi^{3/2}$. Field Emission Energy Distribution data is presented as energy in eV below the vacuum level of the field emission tip, and is the difference between measured electron kinetic energy with respect to the vacuum energy level at ground (E_{KIN}) and the voltage placed on the field emission tip (V_{TIP}).

$$\text{Energy eV} = E_{KIN} - V_{TIP} \tag{5.1}$$

The low binding energy onset of the FEED and its correlation to work function is dependent on the material being conductive because resistive losses and band bending at the surface could influence the distribution for other materials. For conductors the transition should be a direct tunneling from the Fermi level to the vacuum level, if surface resonance states exist the distribution has extra structure below the Fermi energy [1]. Under the above conditions, the inflection point of the FEED with electron kinetic energy referenced to the vacuum level corresponds to the work function [2].

This experiment uses a custom built analytical chamber detailed in chapter 3 that was calibrated using thermal emission to determine vacuum level, transmission function, analyzer energy constant, and linearity of energy scale. Additionally the FEED was compared to FEED obtained on a VG ESCA LAB MKII that was reference to the vacuum energy level and calibrated by UPS from a pure copper sample at various photon energies. The FEED from molybdenum tips measured in the custom built analytical chamber and VG ESCA LAB MKII agreed, with the inflection point of the Exponentially Modified Gaussian fit located 4.6 ± 0.1 eV below the vacuum level. This value is confirmed by the UPS data in chapter 4 and the stated work function value of 4.6 eV for polycrystalline molybdenum [3].

The field emission tips were made from 0.02-inch diameter molybdenum wire electrolytically etched as detailed in chapter 3. The iridium oxide tips were prepared by pulsed laser ablation deposition of iridium on etched molybdenum tips, and then annealing in oxygen ambient at 600°C for one hour. A 248 nm KrF pules excimer laser

was used to ablate a stoichiometric iridium target in the same method the flat UPS samples were made and detailed in chapter 4.

5.2 Field Emission Characterization of Molybdenum Tips

The pure molybdenum tips showed some changes in energy distribution on initial startup that stabilized after a few hours of field emission under 1×10^{-7} Torr pressure. This shifting is attributed to the build up of surface oxides between field emission runs and subsequent removal under field emission conditions with high current densities by field desorption cleaning [4]. This concurs with the observation that the shifting was greater for a molybdenum tip characterized under pressures greater than 1×10^{-7} Torr and minimized when 1×10^{-9} Torr was obtained by addition of an ion pump. Also, SEM pictures showed that sever etching of the tip occurred at the higher pressures during field emission, confirming the desorption process of molybdenum oxide and molybdenum [5].

5.2.1 FEED and Fowler-Nordheim Plots of Molybdenum Tips, 1×10^{-7} Torr Pressure

Figure 5.1.A and 5.1.B show two consecutive runs of FEED and Fowler-Nordheim plots of a molybdenum tip under 1×10^{-7} Torr or greater pressures. Figure 5.1.A is the first run after a few days of no field emission and figure 5.1.B the second scan done immediately after the first.

Fitting the first FEED at 680 V anode voltage in figure 5.1.A gives an inflection point located 6.35 $\pm$0.1 eV below vacuum level. This spectrum shifting is approximately 1.8 eV below the FEED inflection point of clean molybdenum located at 4.6 eV. This shift is in agreement with previous research measuring the work function change of

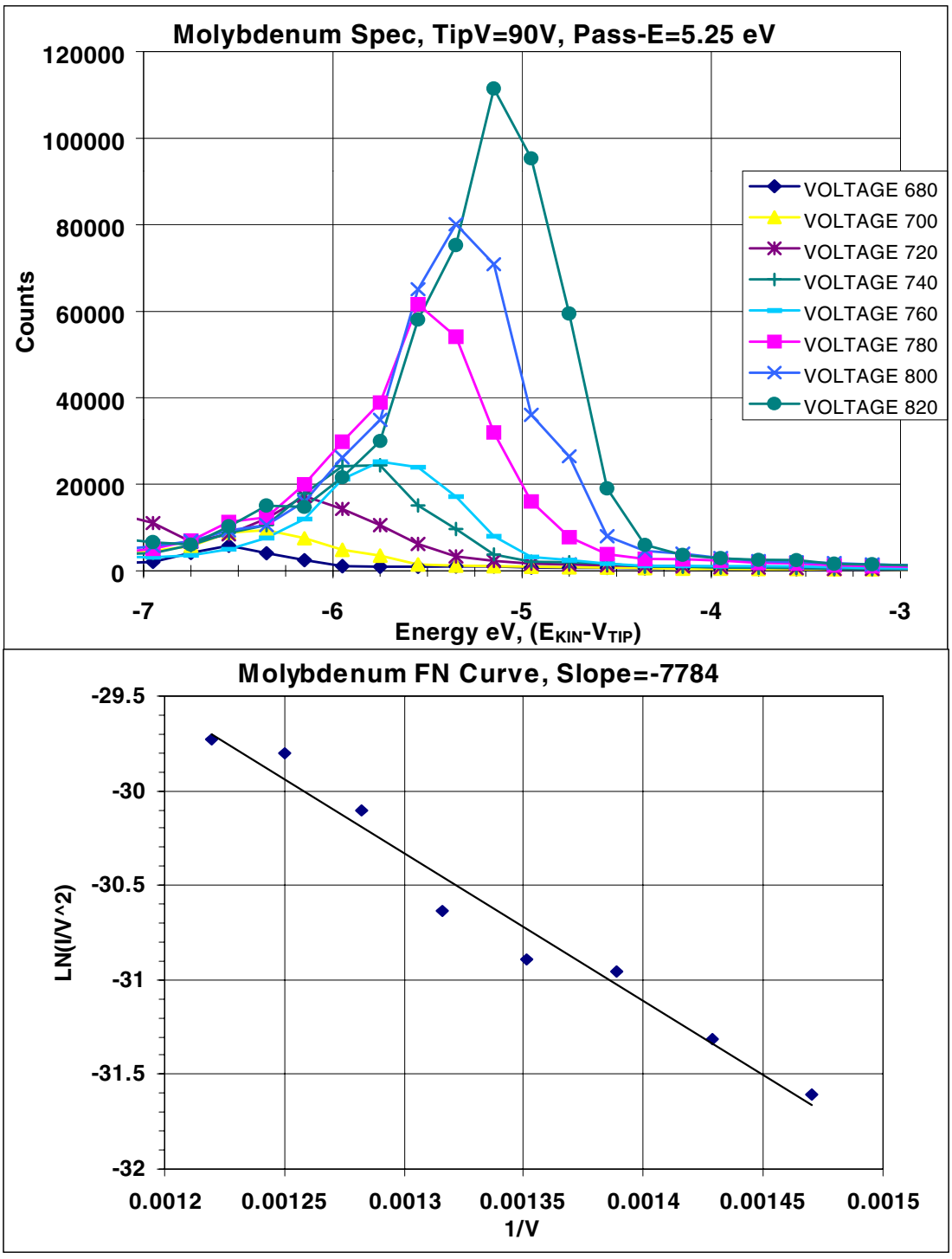

Figure 5.1.A. FEED and Fowler-Nordheim plot of molybdenum tip under high background gas (1×10^{-7} Torr or greater) and first run conditions.

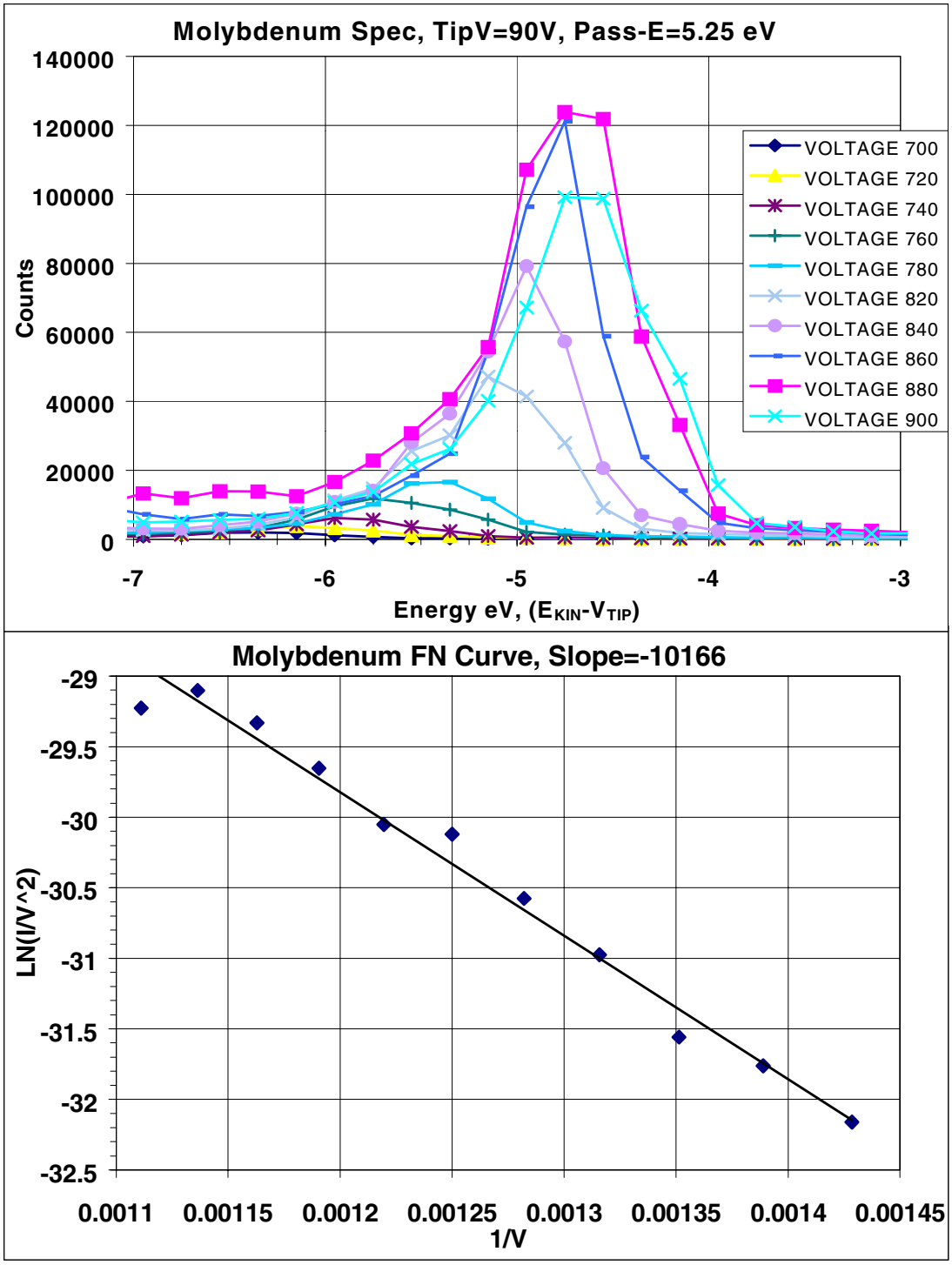

Figure 5.1.B. FEED and Fowler-Nordheim plot of molybdenum tip under high background gas (1×10^{-7} Torr or greater) and after first characterization run.

molybdenum exposed to oxygen while in vacuum with a shift of 1.8 ±0.1 eV [6]. Figure 5.1.B shows the same shifting, but note that the higher anode voltage FEEDs begin to stabilize with the inflection point located around 4.6 eV. Shifting of spectra was seen mostly under the higher pressure (1×10^{-7} Torr) conditions and was minimized but still detectable after several hours of field emission. This demonstrates the field desorption cleaning is an effective method to remove molybdenum oxides under higher emission current densities and a competitive process of formation and desorption of molybdenum oxides exists.

The Fowler-Nordheim I-V curves also demonstrate the process of formation and desorption of molybdenum oxide by showing that the geometric factor ($b \propto$ tip radius) increases by removal of field emission tip material. The shift in Fowler-Nordheim slope from –7784 for the first field emission run to –10166 in the second is attributed to an increase in b because the work function does not increase in the FEED data but decreases.

Figure 5.2.A is a SEM picture of the molybdenum field emission tip used under the higher pressure conditions (1×10^{-7} Torr) which shows sever etching due to field desorption. Original inspection of this tip under an optical microscope showed the tip was relatively sharp comparable to the iridium oxide coated tip presented in figure 5.5.A with a tip diameter of approximately 30 μm. After this tip was removed and inspected, all following tips had SEM pictures taken before and after field emission characterization. Also, a larger ion pump (300 L/s) was attached to the analytical chamber giving a lower standard operating pressure of 1×10^{-9} Torr. Figure 5.2.B is SEM picture of the second

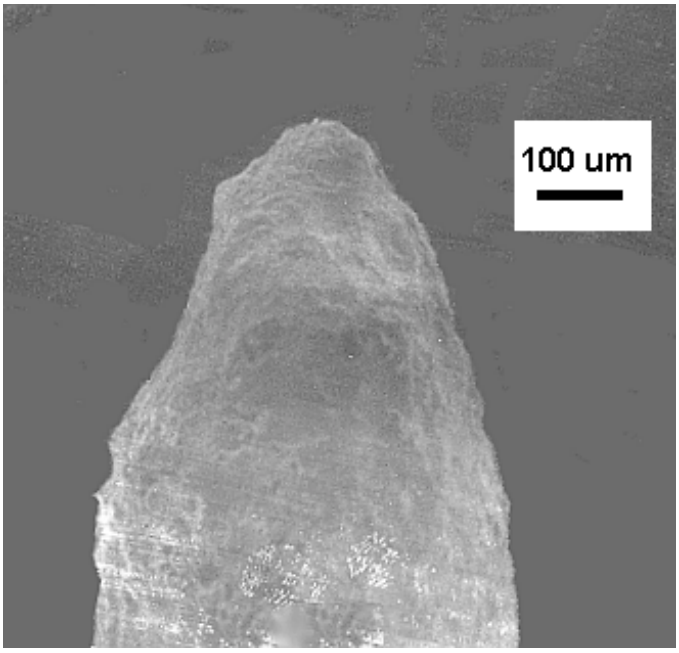

Figure 5.2.A. SEM picture of initial molybdenum tip under high background gas (1×10^{-7} Torr or greater) after field emission characterization experiments.

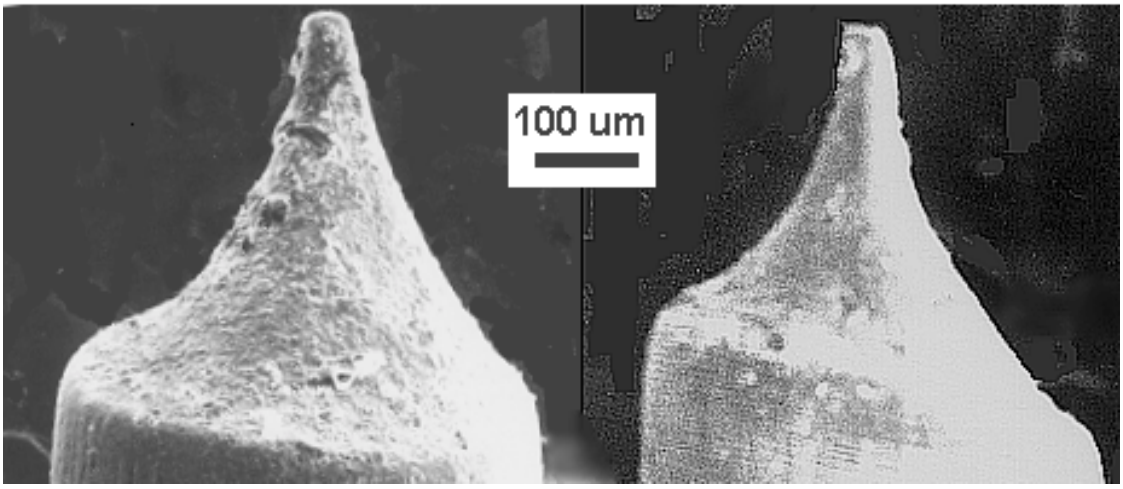

Figure 5.2.B. SEM picture of second molybdenum tip under low background gas (1×10^{-9} Torr) before (left) and after (right) field emission characterization experiments.

pure molybdenum tip characterized under UHV conditions with good stability in tip geometry before (left) and after (right) FEED and Fowler-Nordheim characterization. In general, stability was improved in FEED and Fowler-Nordheim I-V measurements with 1×10^{-9} Torr base pressure.

5.2.2 FEED and Fowler-Nordheim Plots of Molybdenum Tips, 1×10^{-9} Torr Pressure

Figure 5.3.A is the FEED and Fowler-Nordheim plots of the same molybdenum tip characterized previously, but under 1×10^{-9} Torr pressures. After about one hour of emission, stability was achieved and the measurement taken confirming greater stability at lower background pressures. Although this tip had a large diameter of about 100 μm the SEM picture clearly shows a rough surface enhancing the geometric factor in the Fowler-Nordheim slope, with a slope of –9213 and good linearity. The FEED also maintained good stability with no detectable shifting in the distributions under greater anode voltages, higher emission current. Additionally, the emission tip did not show any additional field desorption etching after field emission characterization under UHV.

Figure 5.3.B is the sum of the normalized energy distributions presented in Figure 5.3.A and fitted with Peakfit [7]. To normalize and sum, the largest point in each distribution was set to one and all distributions summed together and plotted as points in the figure. This was fitted with an Exponentially Modified Gaussian (EMG) after background subtraction (plotted by the smooth curve fit). This fit gives an inflection point 4.6 eV below the vacuum level and 95% confidence interval of ± 0.02 eV. For this measurement analyzer energy was 7.35 eV and $\Delta E/E = 0.077$ giving a FWHM resolution

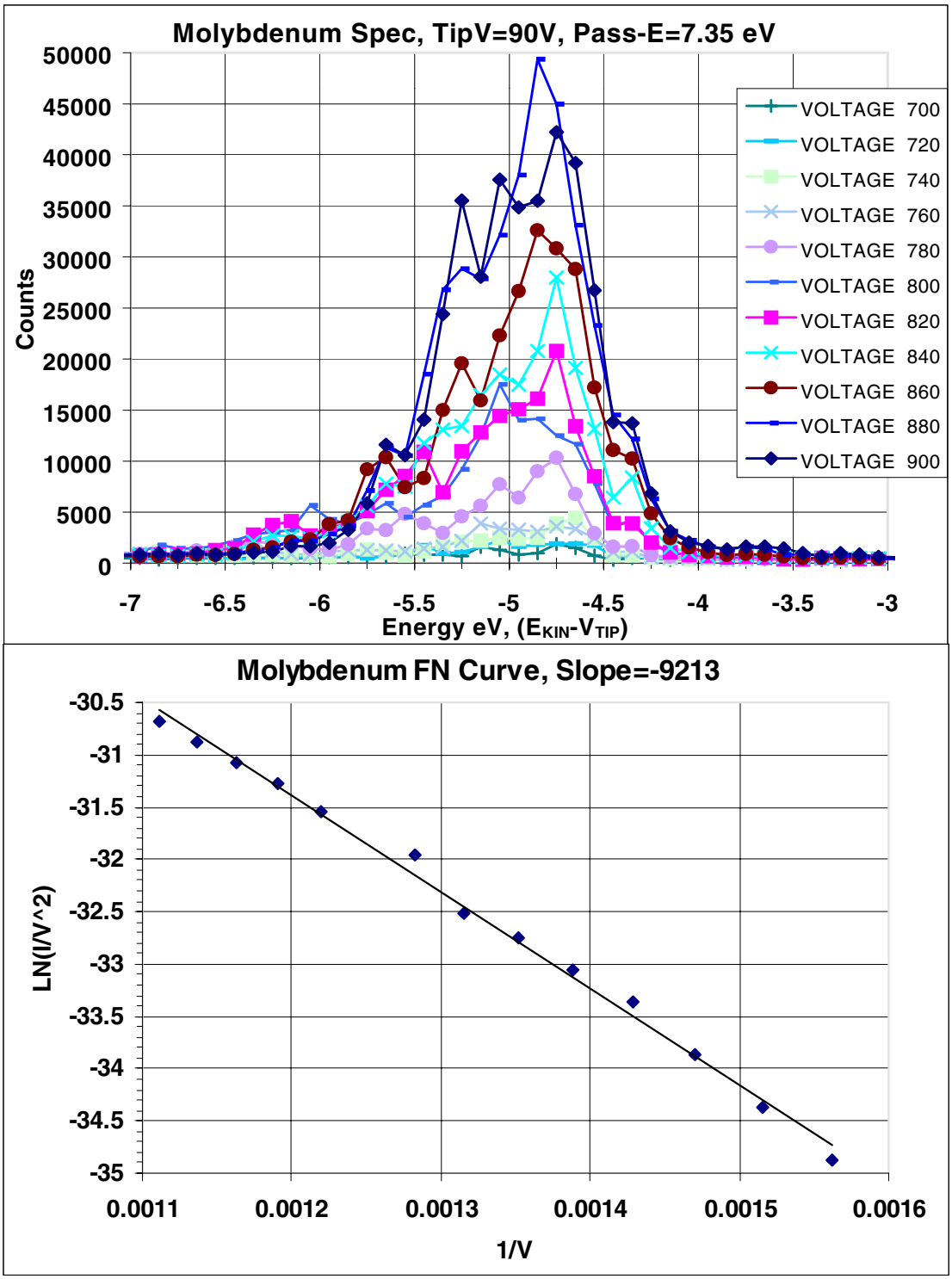

Figure 5.3.A. FEED and simultaneous Fowler-Nordheim plots from a Molybdenum tip under low-pressure (1×10^{-9} Torr) conditions with greater stability.

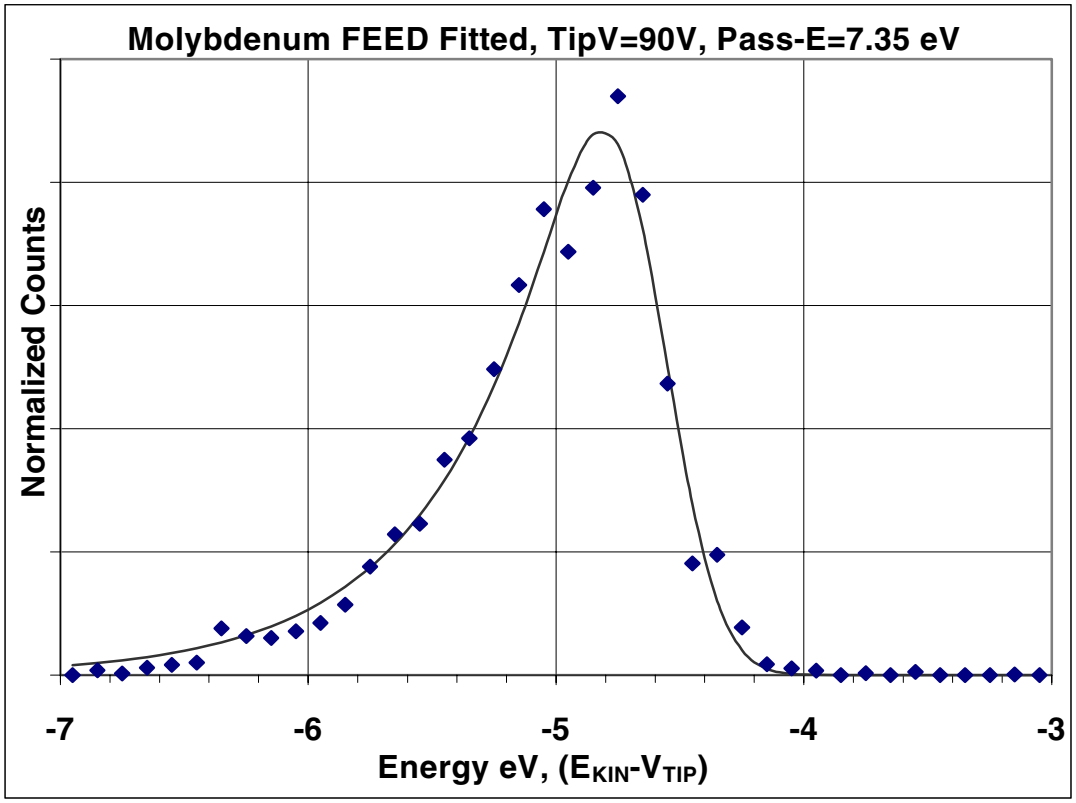

Figure 5.3.B. Fitted FEED of the normalized and summed distributions of Figure 5.3.A giving an inflection point 4.6 eV below vacuum level and a FWHM of 0.75 eV.

of 0.57 eV. Theoretical FEED calculations for a conductor with thermal broadening at 300°K gives a FWHM of approximately 0.2 eV. The combination of these errors agrees roughly with the experimental FWHM of 0.75 eV [2]. The inflection point 4.6 eV below vacuum level agrees with the work function value of polycrystalline molybdenum [3].

Figure 5.4.A is the FEED and Fowler-Nordheim plots of the second molybdenum tip characterized, with SEM pictures in 5.2.B and under 1×10^{-9} Torr pressures. A thermocouple was attached 3-5 mm away from the emission tip to measure temperature changes during the different field conditions used. The temperature fluctuations were too minor to correlate with field emission heating, with an average temperature of 22.5°C and a temperature range of 0.5°C over an emission current of 0 to 10μA. The FEED and Fowler-Nordheim I-V results are more unstable than the previous results because this is the first characterization scan and the close presence of the thermocouple may effect results. Later scans show more stability, however molybdenum oxides were formed on the surface with minimal field desorption. This indicates that pressure is a factor in field desorption, where the gas is ionized and actively sputters the emitter surface [8].

The top plot in Figure 5.4.B is the sum of the normalized energy distributions presented in Figure 5.4.A and fitted with Peakfit in the same manner the first molybdenum tip was analyzed [7]. The lower plot is the normalized energy distribution of the same tip after several hours of field emission with more oxides present. The FEED spectra required more than one EMG after background subtraction to obtain a good fit. The first FEED is fitted with two EMGs with inflection points at 4.6 eV and 5.3 eV

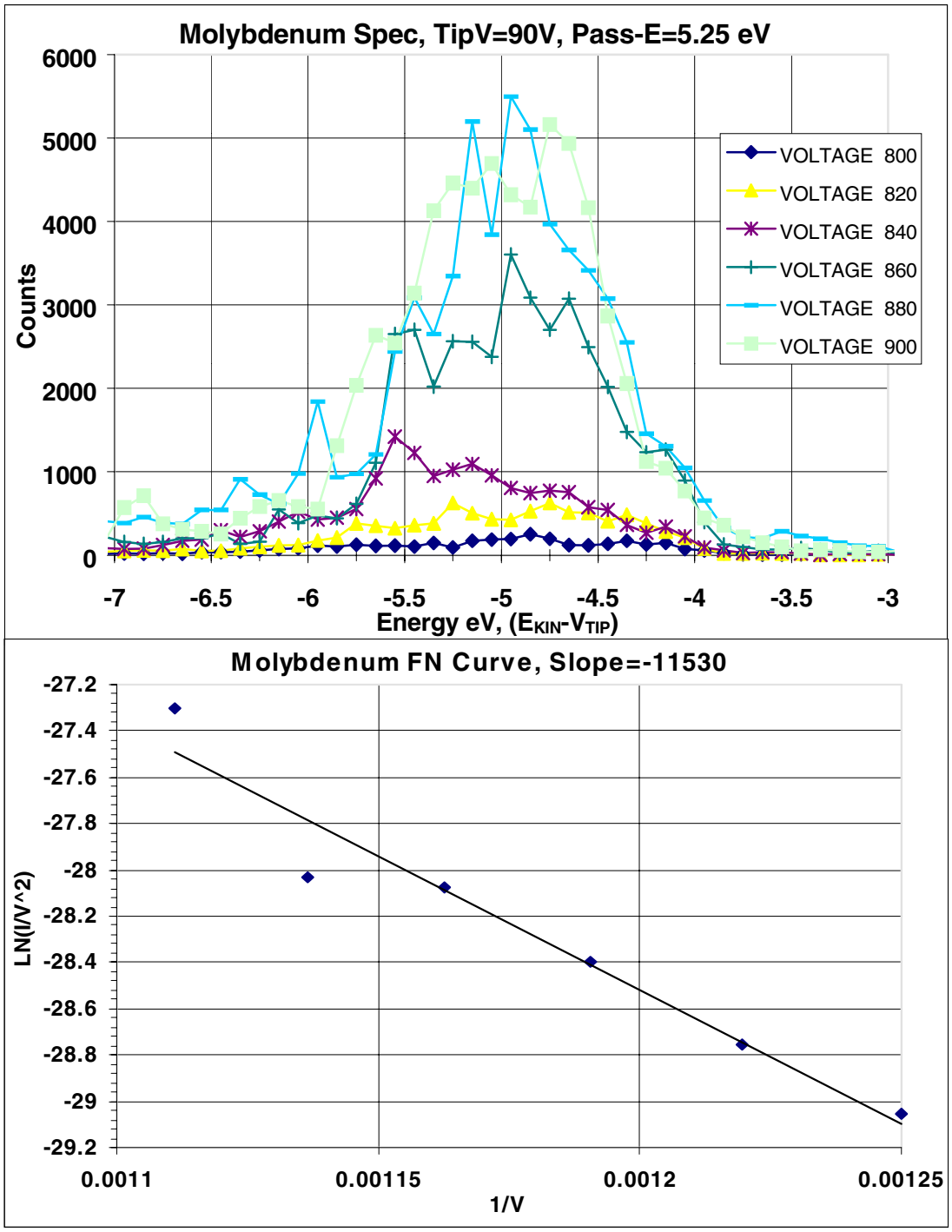

Figure 5.4.A. FEED and simultaneous Fowler-Nordheim of second molybdenum tip under low-pressure (1×10^{-9} Torr) conditions with thermocouple attached.

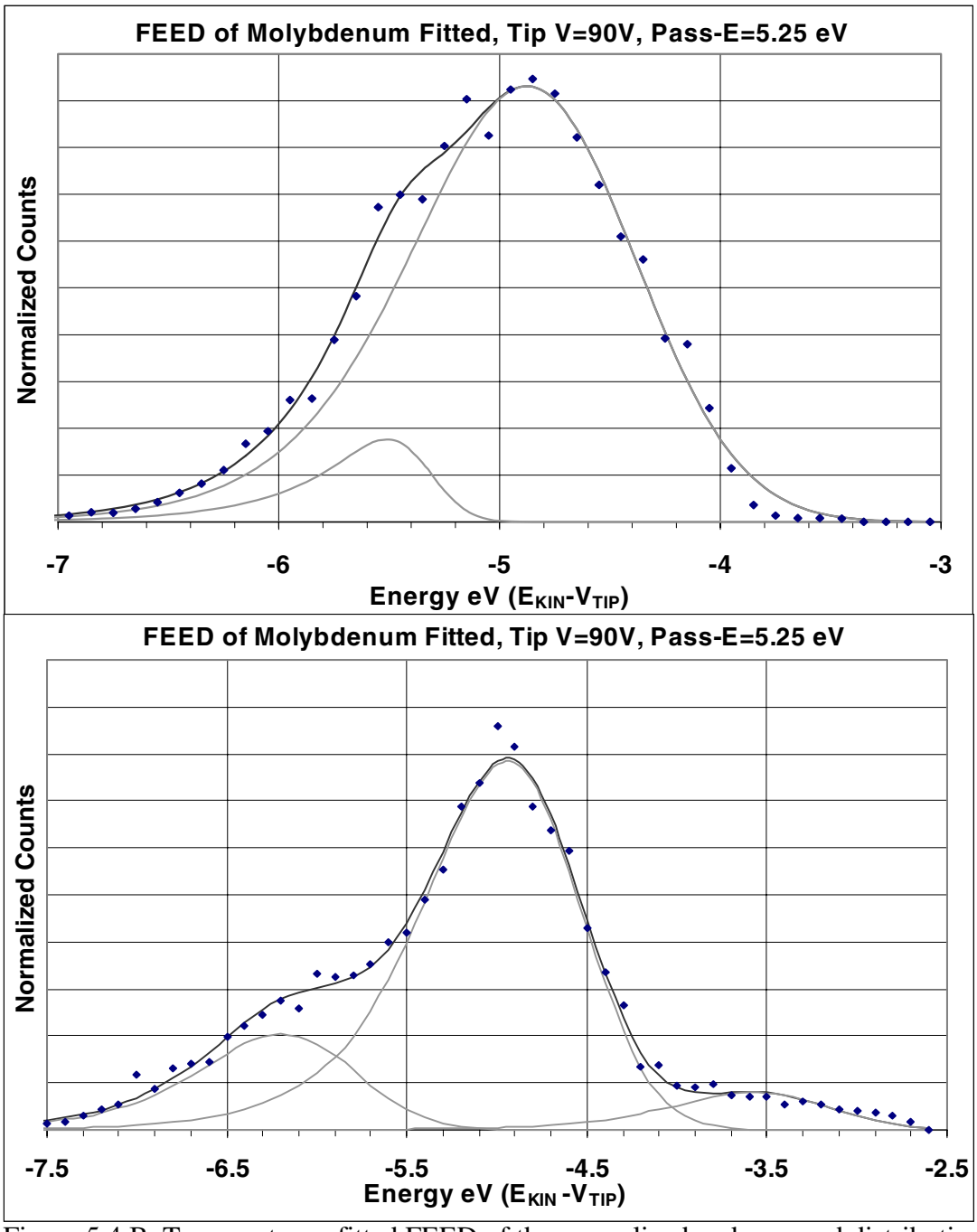

Figure 5.4.B. Top spectrum, fitted FEED of the normalized and summed distributions of Figure 5.4.A giving inflection points 4.6 eV and 5.3 eV below vacuum level. Bottom spectrum, fitted FEED of same tip after hours of field emission giving inflection points 3.3 eV, 4.6 eV, and 5.9 eV below vacuum level.

below the vacuum level, and a 95% confidence interval of ± 0.06 eV in the 4.6 eV peak. The 4.6 eV value agrees with the work function value of molybdenum and the 5.3 eV agrees with surface resonance states also found in the UPS results of chapter 4 and previous FEED and UPS research on molybdenum (100) plane [9,10]. The second FEED is fitted with three EMGs with inflection points at 3.3 eV, 4.7 eV, and 5.9 eV below the vacuum level. The 4.7 eV is from molybdenum, while the 3.3 eV and 5.9 eV values are attributed to MoO_3 and MoO_2 respectively. Research on MoO_3 has shown than under UV radiation or high electric field a defect version of this oxide is created with a beep blue color that possess an energy gap between valence and conduction electrons of 3.2 eV in close agreement with the 3.3 eV distribution [11]. The 5.9 eV result is attributed to the formation of MoO_2 that has a binding energy about 1 eV greater than molybdenum [12].

5.3 Field Emission Characterization of Iridium Oxide Coated Tips and Iridium

The iridium oxide tips were characterized under UHV conditions (1×10^{-9} Torr) and demonstrated improved stability over bare molybdenum tips. The growth of high work function molybdenum oxides (greater than 5 eV) was greatly minimized during field emission and their effect on the FEED spectrum was minor. Additionally, shifting of the FEED from initial to later measurements was minimized to 0.6 eV or less.

Figure 5.5.A is a SEM picture of an iridium oxide coated tip characterized and presented in the following section. On this particular tip, the iridium oxide coating was present at the area of field emission. However, many tips were not coated at the emission tip apex with iridium oxide. Figure 5.5.B is a close up SEM picture of the iridium oxide

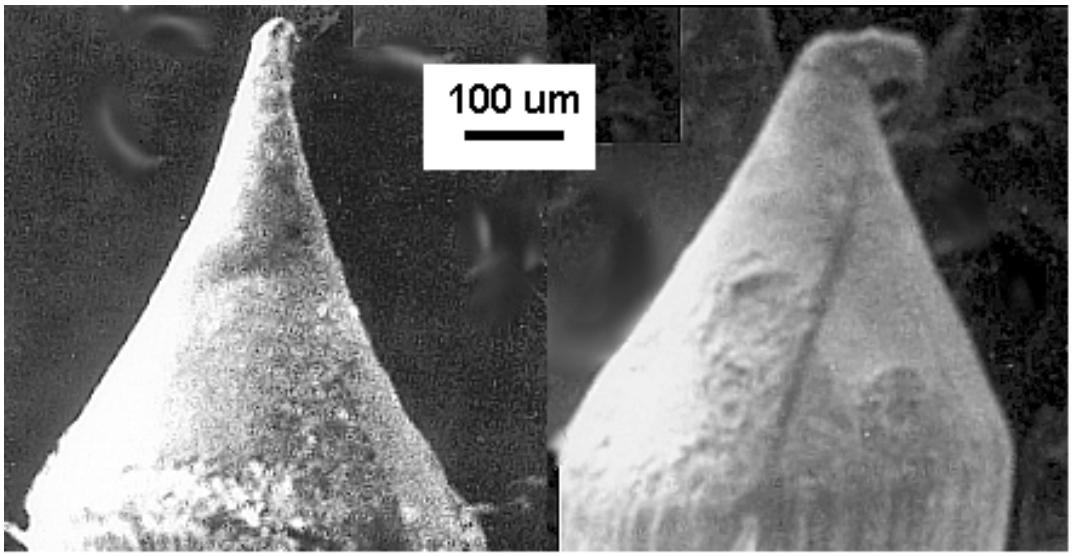

Figure 5.5.A. SEM picture of iridium oxide coated tip before (left) and after (right) field emission characterization experiments. The tip was bent by impacting the anode aperture while positioning, but data presented was taken before the impact.

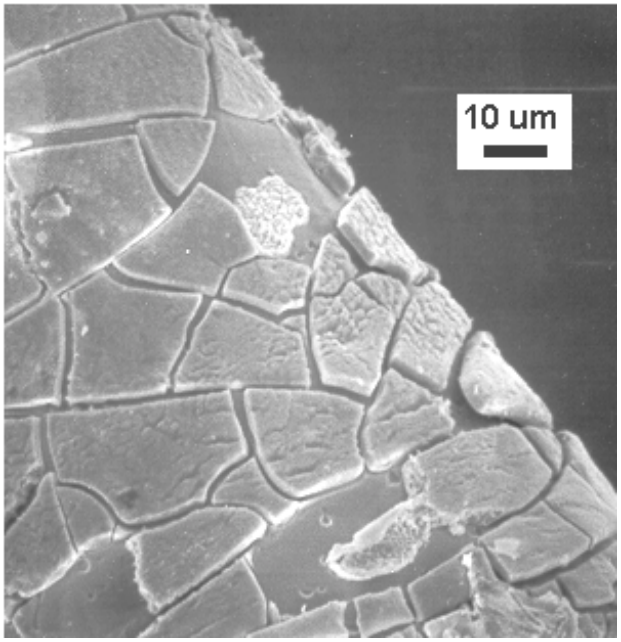

Figure 5.5.B. Close up SEM picture of iridium oxide coated tip away from apex showing cracking and flaking in iridium oxide coat exposing molybdenum and molybdenum oxide beneath.

coating on the side of an emission tip and it is evident that the coating is not conformal but has cracking exposing the molybdenum and molybdenum oxide underneath. This incomplete coverage is confirmed by FEED spectra of tips treated to have iridium oxide coating, which give spectra similar to bare molybdenum tips with distribution components attributed to molybdenum and molybdenum oxides.

Iridium wire was also characterized with FEED to examine the formation of iridium oxide on metallic iridium. The wire was only 0.005 inches in diameter, and a tip was formed by cutting the wire at a diagonal with standard wire cutters. These tips were inspected under an optical microscope and found to have a sharp apex.

5.3.1 FEED and Fowler-Nordheim Plots of Iridium Oxide Coated Tips

Figure 5.6.A is the FEED and Fowler-Nordheim plots of the iridium oxide coated tip shown in Figure 5.5.A under 1×10^{-9} Torr pressures. After stability was achieved, the measurements taken confirm greater stability for the iridium oxide coated tips. FEED spectra maintained very good stability with no shifting in distributions at greater anode voltages and the Fowler-Nordheim I-V slope was linear with a value of -9721. Throughout the experiment, the FEED spectra had no detectable contributions from high work function oxides above 5.1 eV.

Figure 5.6.B is the sum of the normalized energy distributions presented in Figure 5.6.A and fitted with Peakfit in the same manner as the molybdenum tips were fitted [7]. Three EMGs were used with inflection points at 3.2 eV, 4.16 eV, and 4.6 eV below the vacuum level, the 4.16 eV peak has a ± 0.05 eV confidence limit and is rounded to 4.2eV.

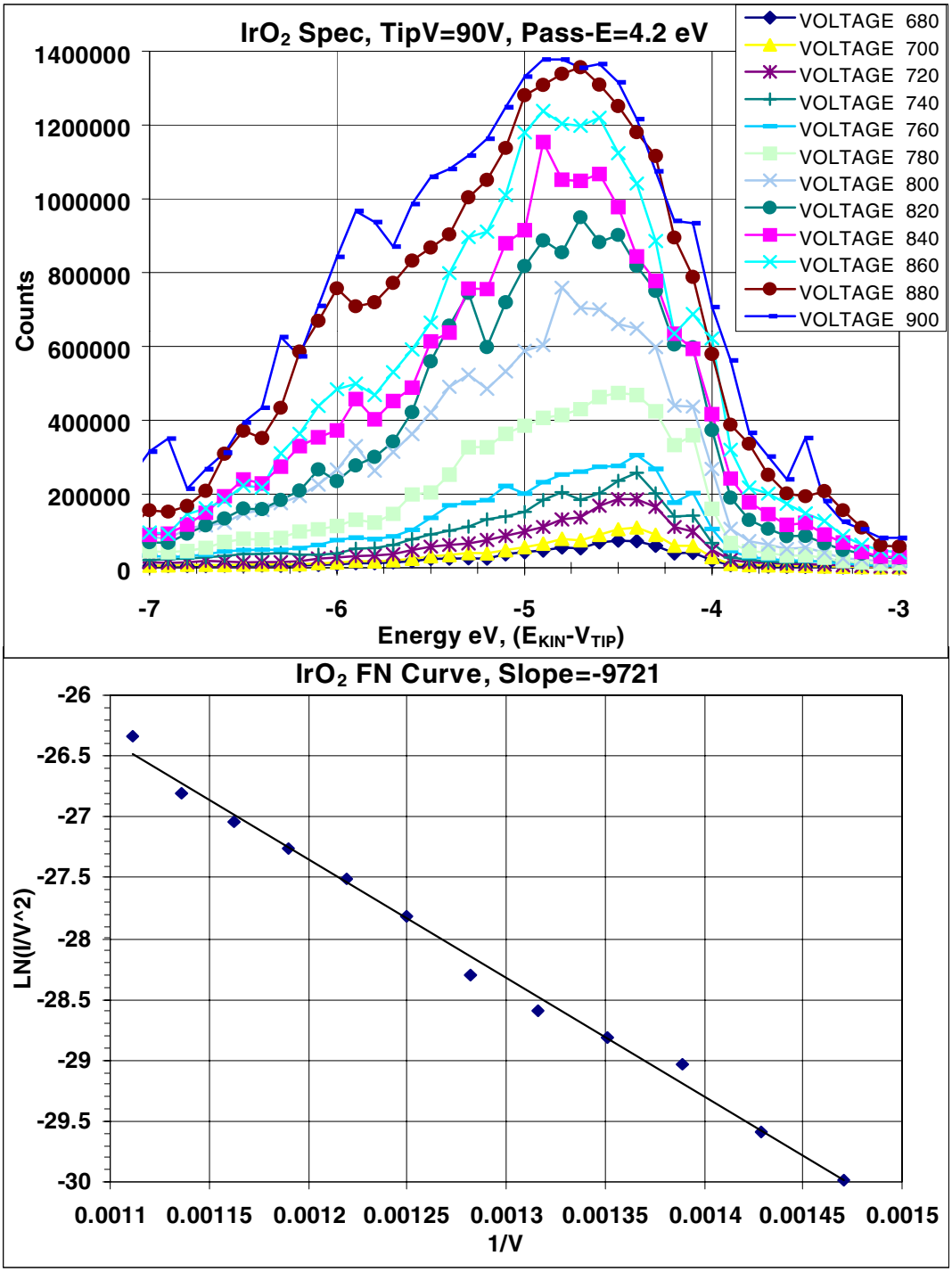

Figure 5.6.A. FEED and simultaneous Fowler-Nordheim plots from an iridium oxide coated tip under low-pressure (1×10^{-9} Torr) with greater stability.

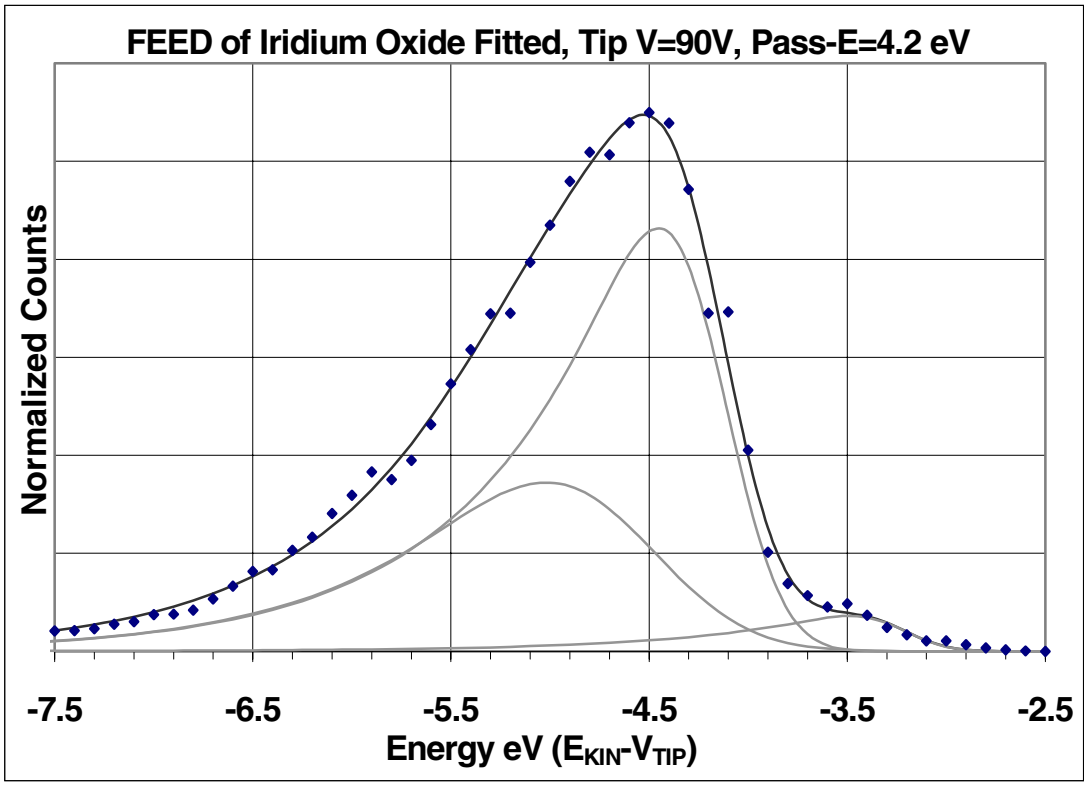

Figure 5.6.B. Fitted FEED of the normalized and summed distributions of Figure 5.6.A giving inflection points 3.2 eV, 4.2 eV, and 4.6 eV below vacuum level.

The largest contribution of 4.2 eV is attributed to iridium oxide (IrO_2) with a 4.2 eV work function determined in the chapter 4 by UPS. The other distributions with 3.2 eV and 4.6eV values are attributed to MoO_3 and metallic Mo respectively as seen on the previous pure molybdenum tips. The presence of field emission from molybdenum and molybdenum oxide substrate concurs with the SEMs showing incomplete coverage.

Figure 5.7.A is the FEED and Fowler-Nordheim plots of the same iridium oxide coated tip characterized above, but before good stability was achieved soon after initial turn on of the field emission tip. During initial turn on the spectra showed greater stability than bare molybdenum as is evident in the minor shifting of the inflection point from approximately 4.1 eV to 4.7 eV as the anode voltage is ramped from 680V to 840V. This shift of approximately 0.6 eV is much less than the 1.8 eV shift found with molybdenum tips at initial turn on and after stabilization. The Fowler-Nordheim I-V slope was stable and linear with a value of -11977. If the work function the emission tip changed from 4.7eV to 4.1 eV this would account for the change in slope from –11977 to –9721 as the tip goes through the stabilization emission. However, not all the emission is from 4.7 eV below the vacuum level in the initial case and 4.1 eV in the final case, so a combination of predominantly work function change and some geometric changes are attributed to the change in Fowler-Nordheim I-V slope.

The top plot in Figure 5.7.B is the sum of the first four normalized energy distributions presented in Figure 5.7.A (680V to 740V on anode) and fitted with Peakfit. The lower plot is the sum all normalized energy distributions presented in Figure 5.7.A.

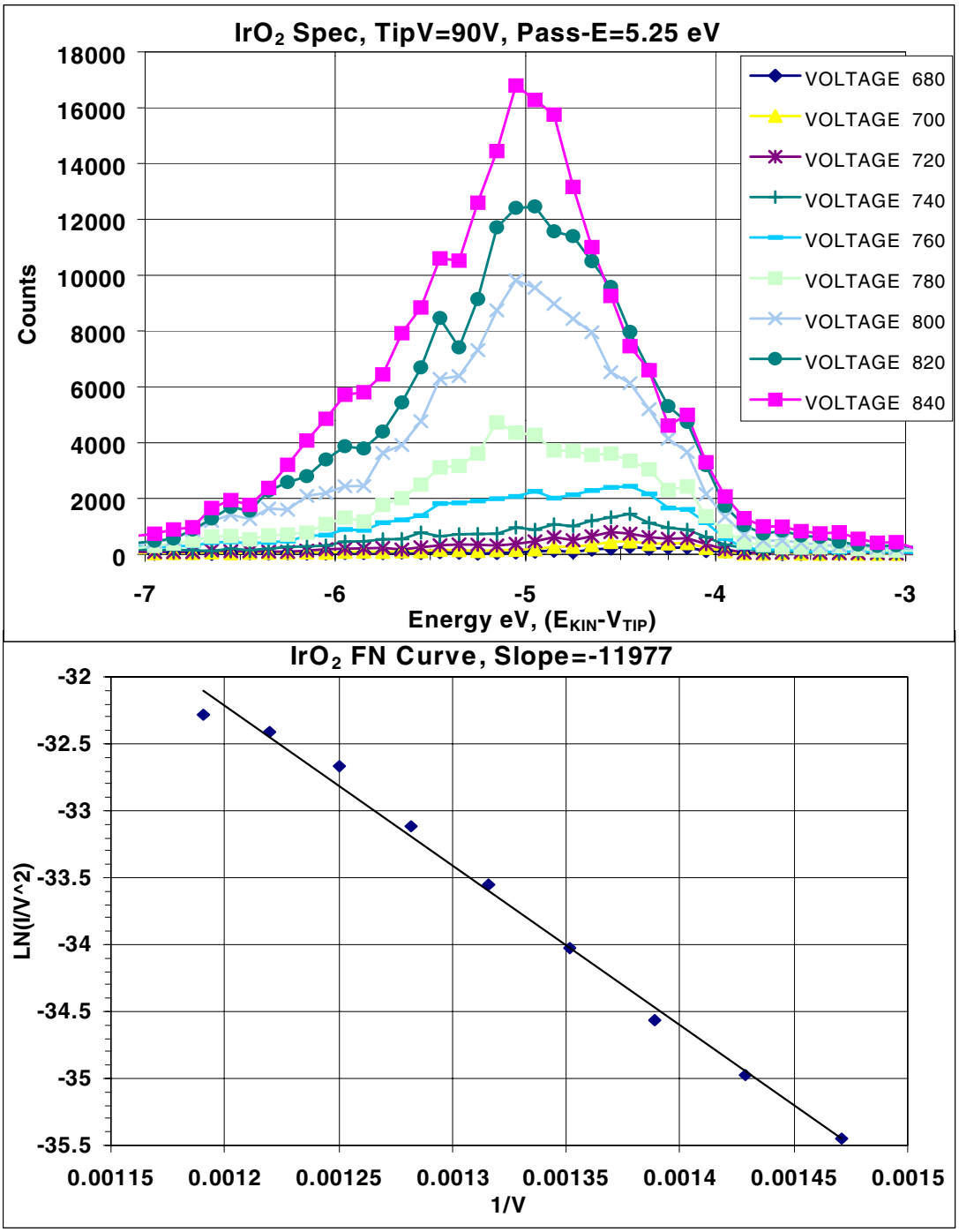

Figure 5.7.A. FEED and simultaneous Fowler-Nordheim plots from an iridium oxide coated tip under low-pressure (1×10^{-9} Torr) conditions soon after initial turn on.

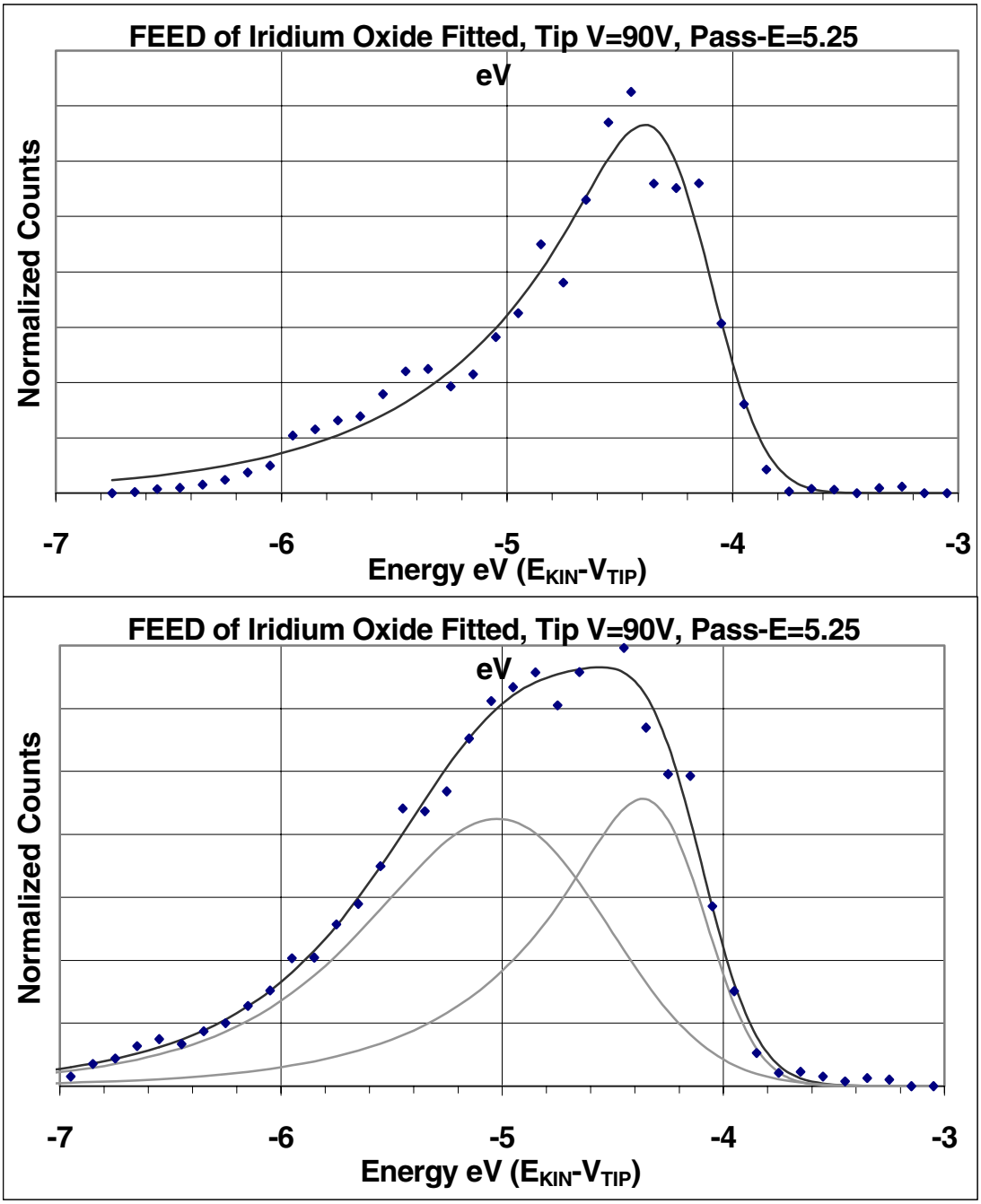

Figure 5.7.B. Top spectrum, fitted FEED of the first four normalized and summed distributions of Figure 5.7.A (680V to 740V on anode) giving an inflection point at 4.1 eV below vacuum level. Bottom spectrum, fitted FEED of all distributions of Figure 5.7.A giving inflection points 4.1 eV and 4.7 eV below vacuum level.

These two plots show the shifting in energy distributions as the anode is ramped up in voltage allowing emission from the partially exposed molybdenum substrate. The top normalized FEED is fitted with one EMG with an inflection point at 4.14 eV and a ± 0.04 eV 95% confidence interval rounded to 4.1 eV below the vacuum level corresponding to emission from iridium oxide. The lower normalized FEED is fitted with two EMGs with inflection points at 4.1 eV and 4.7 eV below vacuum level. These values correspond to IrO_2 and metallic Mo work functions, again demonstrating the poor coverage of IrO_2.

5.3.2 FEED and Fowler-Nordheim Plots of Iridium Wire

Figure 5.8.A is the FEED spectra of a 0.005-inch diameter metallic iridium wire under 1×10^{-9} Torr pressure, top plot is an initial scan and the bottom plot is a subsequent scan. Both spectra show the growth of iridium oxide with field emission energy distributions forming around 4.2 eV and slowly growing in size during field emission compared to the other structures in the distribution that are farther below the vacuum energy level. These structures below 5 eV from the vacuum level correspond to metallic iridium with work function values between 5.0 eV for the (210) iridium metallic plane to 5.76 eV for the (111) plane [13].

The top and bottom plot in Figure 5.8.B is the sum of the normalized energy distributions presented in the top and bottom plot of Figure 5.8.A respectively and fitted with Peakfit. Both FEEDs are fitted with three EMGs to obtain a good fit. The top FEED fit gives inflection points at 4.1 eV, 5.3 eV, and 5.8 eV below vacuum and the bottom plot has infection points at 4.2 eV, 5.4 eV, and 5.9 eV. The values of 4.1 eV and 4.2 eV

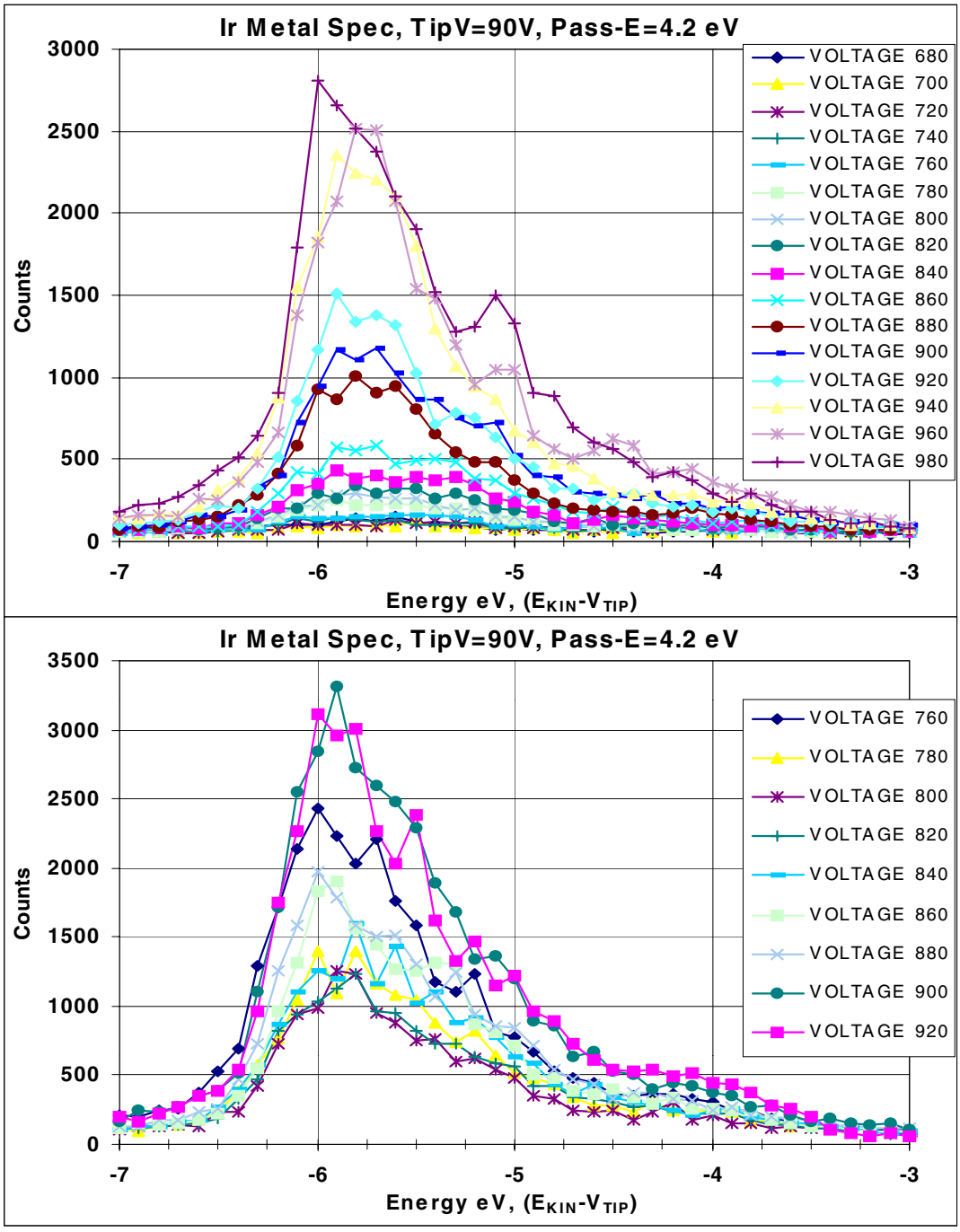

Figure 5.8.A. FEED plots from a metallic iridium tip under low-pressure (1×10^{-9} Torr) conditions soon after initial turn on (top plot) and after hours of emission (bottom plot).

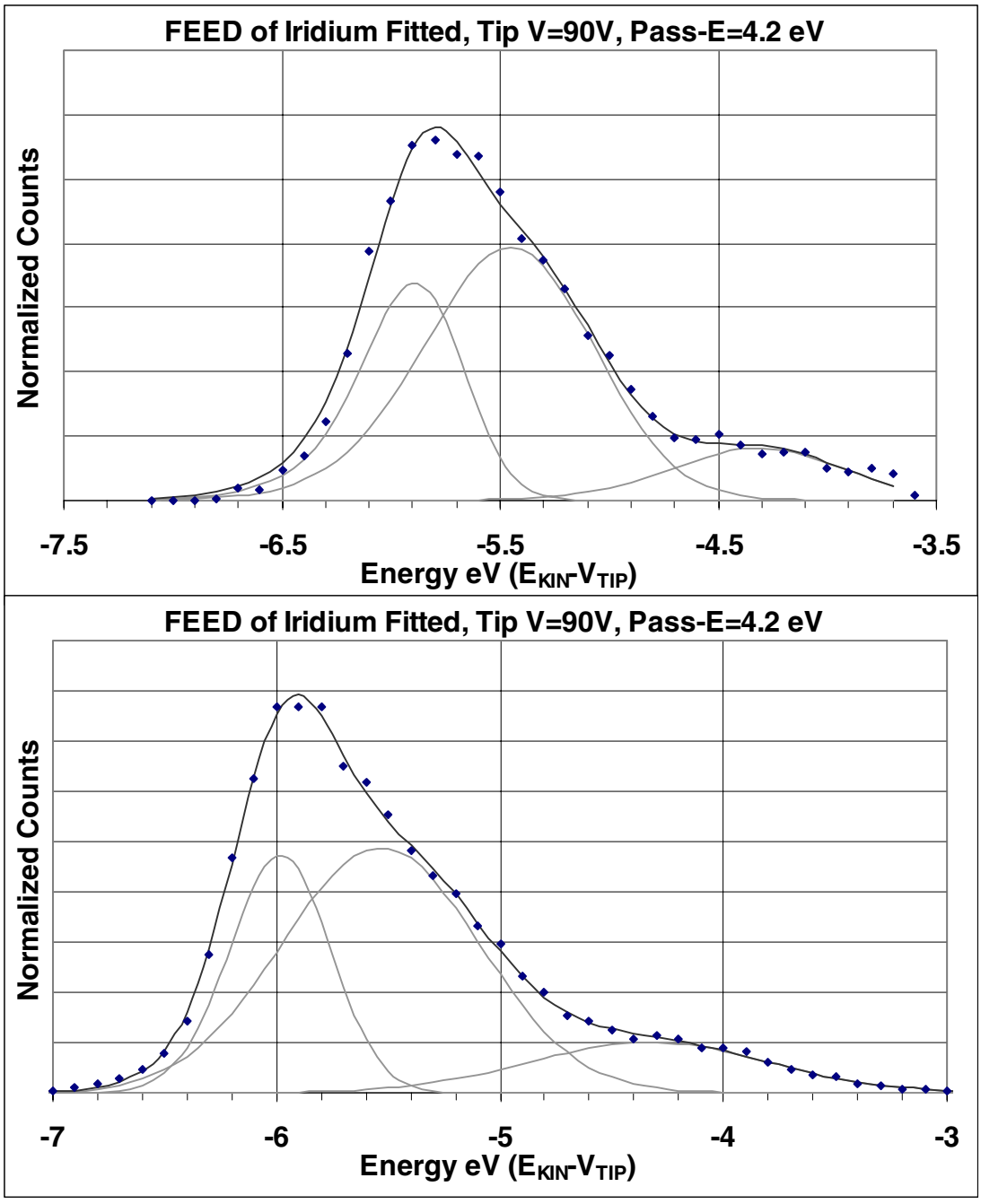

Figure 5.8.B. Fitted FEED of the normalized and summed distributions of Figure 5.8.A, with top and bottom plots correlated respectively. Top spectrum has inflection points at 4.1 eV, 5.3 eV, and 5.8 eV below vacuum level. Bottom spectrum has inflection points at 4.2 eV, 5.4 eV, and 5.9 eV below vacuum level.

agree with the work function value of IrO_2, and the area of this structure increases during field emission from 12% to 14.3% of the total analytical area between the first and later scans. The values of 5.3 eV, 5.4 eV, 5.8 eV, and 5.9 eV agree with metallic iridium work function vales of 5.76 eV for the (111) plane, 5.42 eV for the (110) plane, and 5.27 eV for polycrystalline iridium metal.

5.4 Conclusions

The FEED spectra of molybdenum field emission tips under UHV conditions show a work function measurement of 4.6 eV in agreement with previous research and UPS validating our characterization techniques. Additionally, the FEED shift of 1.8 eV for molybdenum tips exposed to oxygen agrees with previous research.

Fowler-Nordheim I-V plots and SEM pictures confirm field emission desorption and sputtering with dependence on emission current and background chamber pressure.

Iridium oxide coated field emission tips had FEED spectra showing a work function of 4.2 eV in agreement with the UPS data of chapter 4. However, components of molybdenum and molybdenum oxide were present in the FEED data indicating the iridium oxide coating was incomplete. SEM pictures of this coating validated the FEED data showing extensive cracking exposing the molybdenum substrate. Field Emission Energy Distributions of pure iridium wire also demonstrated formation of the low work function IrO_2 in addition to the higher work function components of metallic iridium.

A method to form a conformal coat of IrO_2 over sharp emission tips needs to be developed in order for this process to be effective in enhancing field emission.

References.

1. L.W. Swanson and L.C. Crouser, Phys. Rev. Lett., **19**, 1179 (1967).
2. R.D. Young and C.E. Kuyatt, Rev. Sci. Instrum., **39**, 1477 (1968).
3. D.E. Eastman, Phys. Rev., **B2**, 1 (1970).
4. E.W. Mueller and T.T. Tsong, *Field Ion Microscopy, Principles and Applications*, Elsevier, New York, NY, (1969).
5. S.V. Krishnaswamy and S.B. McLane, Surf. Sci., **70**, 265 (1978).
6. J. Müller, Surf. Sci., **69**, 708 (1977).
7. Peakfit, Jandel Scientific, San Rafeal, CA.
8. R. Gomer, *Field Emission and Field Ionization*, Harvard Univ. Press, Cambridge MA, 56 and 176-177 (1961).
9. R.C. Cinti, E. Al Khoury, and B.K. Chakraverty, Phys. Rev., **B14**, 3296 (1976).
10. Shang-Lin Weng, Phys. Rev. Lett., **38**, 434 (1977).
11. J. Wayne Rabalais and Richard J. Colton, Chemical Phys. Lett., **29**, 131 (1974).
12. F. Werfel and E. Minni, Solid State Phys., **16**, 6091 (1983).
13. CRC Handbook of Chemistry and Physics, 77th ed., 12-122 (1997).

CHAPTER 6

SUMMARY AND CONCLUSIONS

The process of field emission with particular emphasis on work function measurements was examined by simultaneous FEEDs and Fowler-Nordheim I-V plots. These measurements were correlated with UPS work function measurements. Molybdenum and iridium oxide (IrO_2) were characterized and found to have a work function of 4.6 eV and 4.2 eV using both techniques.

The custom built analytic chamber used in the field emission analysis demonstrated the ability to independently determine the value and changes in work function (Φ) and emitter geometry (b) during the dynamic process of field emission. This characterization was accomplished through simultaneous measurement of the Field Emission Energy Distribution and Fowler-Nordheim I-V plots. Where work function is independently determined by the first method, and this value used with the latter method, which is dependent on geometry and work function, to independently evaluate tip geometry.

Iridium Oxide coating was found to enhance the stability of molybdenum emission tips with a relatively low work function of 4.2 eV and inhibited the formation of high work function (more than 5.1 eV) molybdenum oxides. However, the method of pulse laser deposition of iridium and annealing in oxygen to form iridium oxide on molybdenum emitters left rather severe cracking in the protective oxide coating exposing the molybdenum substrate. A more effective process of coating iridium oxide in a conformal manner needs to be address before this technique can be reliably utilized to enhance and stabilize emission of field emitters in less than ultra high vacuum conditions.

BIBLIOGRAPHY

Berge, S., P.O. Gartland, and B.J. Slagsvold, Surf. Sci., **43**, 275 (1974).

Berglund, C.N., and W.E. Spiecer, Phys. Rev., **A136**, 1030 (1964).

Berglund, C. N., and W.E. Spicer, Phys. Rev., **A136**, 1044 (1964).

Block, J.H., *Chemistry and Physics of Solid Surfaces*, CRC Press, Boca Raton FL, ch3., (1977).

Blouin, M., and D. Guay, J. Electrochem. Soc., **144**, 573 (1997).

Brodie, I., and P.R. Schwoebel, Proc. IEEE, **82**, 1006 (1994).

Chalamala, B., J. Bernhard, D. Golden, B. Gnade, E. Sosa, S. Aggarwal, Appl. Phys. Lett., **74**, 1394 (1999).

Chalamala, B.R., R.M. Wallace, and B.E. Gnade, J. Vac. Sci. Technol., **B16**, 2859 (1998).

Cinti, R.C., E. Al Khoury, and B.K. Chakraverty, Phys. Rev, **B14**, 3296 (1976).

Cordfunke, E.H.P., and G. Meyer, Recueil, **81**, 495 (1962).

CRC Handbook of Chemistry and Physics, 77th ed., (1997).

Dahl, D.A., and J.E. Delmore, SIMION Version 4.0 EGG-CS-7233 Rev. 2, Idaho National Engineering Laboratory (1988).

Dautremont-Smith, W. C., Displays, **3**, 67, (1982).

Dyke, W.P., and W.W. Dolan, Adv. Electronics and Electron Phys., **8**, 90 (1956).

Eastman, D.E., Phys. Rev, **B2**, 1 (1970).

Einstein, A., Annalen der Physik, **17**, 132 (1905).

El Khakani, M.A., M. Chaker, and E. Get, Appl. Phys. Lett., **69**, 2027 (1996).

Excel 97, Microsoft Corporation 1983-1997.

Feuerbacher, B., B. Fitton, and R. F. Willis, *Photoemission and the Electron Properties of Surfaces*, John Wiley, New York, 28 (1978).

Fowler, R.H., Phys. Rev., **33**, 45 (1931).

Fowler, R.H., and L. Nordheim, Proc. Roy. Soc. London, **A119**, 683 (1928).

Gadzuk, J.W., Surface Sci., **15**, 466 (1969).

Gomer, R., *Field Emission and Field Ionization*, Harvard Univ. Press, Cambridge MA, 6-33, 56,and 176-177 (1961).

Gray, H.F., Infor. Displ., **3**, 9 (1993).

Hewlett-Packard Co., HP VEE Ver. 3.12 (1995).

Holloway, P.H., J. Sebastian, T. Trottier, H. Swart, and R.O. Peterson, Solid State Tech., **38**, 47 (1995).

Huang, K., *Statistical Mechanics*, John Wiley & Sons, New York NY, 224 (1963).

Itoh, S., T. Niyamam, and M. Yokoyama, J. Vac. Sci. Tech., **B11**, 647 (1993).

Itoh, S., T. Watanabe, K. Ohtsu, M. Taniguchi, S. Uzawa, and N. Nishimura, J. Vac. Sci. Tech., **B13**, 487 (1995).

Jackson, J.D., *Classical Electrodynamics*, John Wiley & Sons, New York, 75-78 (1962).

Jost, K., J. Phys., **E12**, 1006 (1979).

Kane, E.O., Phys. Rev., **127**, 131 (1962).

Kim, K.S., W.E. Baitinger, J.W. Amy, and N. Winograd, J. of Electron Spectroscopy and Related Phenomena, **5**, 351 (1974).

Kreider, K., Sensors and Actuators, **B5**, 165 (1991).

Krishnaswamy, S.V., and S.B. McLane, Surf. Sci., **70**, 265 (1978).

Kuyatt, C.E., and J.A. Simpson, Rev. Sci. Instrum., **38**, 1 (1967).

Madhukar, S., S. Aggarwal, A.M. Dhote, R. Krishnan, D. Keeble and E. Poindexter, J. Appl. Phys., **81**, 3543, (1997).

Miller, S.C., and H.R. Good, Phys. Rev., **91**, 174 (1953).

Millikan, R.A., and C.F. Frying, Phys. Rev., **27**, 51 (1926).

Modinos, A., *Field, Thermionic, and Secondary Electron Emission Spectroscopy*, Plenum Press, New York, 1-18 (1984).

Mueller, E.W., and T.T. Tsong, *Field Ion Microscopy, Principles and Applications*, Elsevier, New York, NY, (1969).

Müller, J., Surf. Sci., **69**, 708 (1077).

Nakamura, T., Y. Nakao, A. Kamisawa, and H. Takasu, Appl. Phys. Lett., **65**, 1522 (1994).

Norman, J. H., H. G. Staley, and W. E. Bell, J. Chem. Phys., **42**, 1123 (1965).

Peakfit, Jandel Scientific, San Rafeal, CA.

Peakfit, SPSS, Inc., 444 North Michigan Avenue, Chicago, IL 60611.

Peuckert, M., Surface Sci., **144**, 451 (1984).

Rabalais, J.W., and Richard J. Colton, Chemical Phys. Lett., **29**, 131 (1974).

Rogers, D.B., R.D. Shannon, A.W. Sleight, and J.L. Gilson, Inorganic Chem., **8**, 841, (1969).

Ryden, W.D., A.W. Lawson, and C.C. Sartain, Phys. Rev, **B1**, 1494 (1970).

Schaich, W.L., and N.W. Ashcroft, Phys. Rev., **B3**, 2452 (1971).

Schottky, W., Z. Phys., **14**, 63 (1923).

Schreiner, W., *XRD Pattern Processing for the PC*, Materials Data, Inc., Livermore CA.

Schwoebel, P.R., and I. Bordie, J. Vac. Sci. Technol., **B13**, 1391 (1995).

Smentkowski, V. S., and J. T. Yates, J. Vac. Sci. Technol, **A12,** 219 (1994).

Smith, N. V., Phys. Rev., **B3**, 1762 (1971).

Sommerfeld, A., Z. Phys., **47**, 1 (1928).

Spicer, W.E., Phys. Rev., **112**, 114 (1958).

Spindt, C.A., J. Appl. Phys., **39**, 3504 (1968).

Spindt, C.A., United States Patent: 4926056 (1990).

Spindt, C.A., and I. Brodie, Adv. Electron. Electron Phys., **83**, 1 (1992).

Swanson, L.W., and L.C. Crouser, Phys. Rev. Lett., **19**, 1179 (1967).

Utsumi, T., J. Soc. Infor. Displ., **1/3**, 313, (1993).

Wagner, C.D., W.M. Riggs, L.E. Davis, J.F. Moulder, and G.E. Muilenberg, *Handbook of X-ray Photoelectron Spectroscopy*, Perkin-Elmer Corp., Eden Prairie MN, 188 (1979).

Weng, Shang-Lin, Phys. Rev. Lett., **38**, 434 (1977).

Werfel, F., and E. Minni, Solid State Phys., **16**, 6091 (1983).

Wood, R.W., Phys. Rev., **5**, 1 (1897).

Young, R.D., Phys. Rev., **113**, 110 (1958).

Young, R.D., and C.E. Kuyatt, Rev. Sci. Inst., **39**, 1477 (1968).

Young, R.D., and E.W. Müller, Phys. Rev., **113**, 115 (1958).